TRANSFORMER MODELLING FOR TRANSIENT STUDIES

by

WASHINGTON L. A. NEVES

B. Eng., Universidade Federal da Paraíba, 1979
M.Sc., Universidade Federal da Paraíba, 1982

A DISSERTATION SUBMITTED IN PARTIAL FULFILLMENT OF
THE REQUIREMENTS FOR THE DEGREE OF
DOCTOR OF PHILOSOPHY

IN

THE FACULTY OF GRADUATE STUDIES
DEPARTMENT OF ELECTRICAL ENGINEERING

We accept this thesis as conforming
to the required standard

THE UNIVERSITY OF BRITISH COLUMBIA
November 1994

In presenting this thesis in partial fulfilment of the requirements for an advanced degree at the University of British Columbia, I agree that the Library shall make it freely available for reference and study. I further agree that permission for extensive copying of this thesis for scholarly purposes may be granted by the head of my department or by his or her representatives. It is understood that copying or publication of this thesis for financial gain shall not be allowed without my written permission.

(Signature)

Department of Electrical Engineering

The University of British Columbia
Vancouver, Canada

Date December 23, 1994

DE-6 (2/88)

Abstract

Transformer modelling is a concern for the utility industry. The object of this work is to develop and investigate dynamic core models suitable for transient studies. A major advantage of the core models developed here is that they use readily available transformer test data as supplied by the manufacturer.

For ferroresonance and inrush current studies, core saturation needs to be represented reasonably well. A direct approach to producing nonlinear peak flux-current and voltage-current characteristic of the iron core, taking iron losses into account, is presented. The algorithm is simple in concept, easy to implement, and may be useful for electromagnetic transient programs. A crude estimation of the transformer open circuit capacitance is also made from rated frequency data. It is useful for situations in which the transformer exciting current experiences strong capacitive effects.

An iterative algorithm for more correctly representing the flux-linkage curve of a delta-connected transformer, suitable for situations in which the tests are performed with a closed delta, is developed. It uses positive sequence excitation test data as input and takes into consideration the removal of triplen harmonics from the line current.

An approach to model frequency-dependent effects in the transformer core from transformer no-load loss data, is presented. Hysteresis and eddy current effects in the core are treated simultaneously. The flux-current trajectories are generated by circuit models with no need to pre-define them.

Simulations using the developed models are compared to laboratory measurement of inrush current and to a ferroresonance field test.

Table of Contents

List of Tables

List of Figures

Acknowledgement

I would like to express my gratitude to those who helped me to complete this research work. Special thanks are due to my supervisor, Dr. Hermann Dommel for his encouragement, patience, guidance and for arranging much-needed financial support.

I wish to thank Dr. José Martí for discussions and invaluable suggestions. I am grateful to Dr. A. E. Araújo, Dr. S. Carneiro and Dr. A. Soudack for suggestions on the reseach work and on the presentation on the results in this thesis.

I am grateful to Dr. W. Dunford and Dr. M. Wvong for their help at the early stage of this work. Thanks are due to Mr. A. Otter for providing financial help from TRIUMF (Tri-University Meson Facility)-Vancouver, B.C., and for discussions and providing test material.

Thanks are due to The Canadian Electrical Association (CEA) and Powertech Labs Inc., for financial assistance during part of this work and for providing transformer data from Project 267-D-766. The support of Mr. J. Drakos, Mr. M. B. Hughes and Mr. K. Takahashi, is gratefully acknowledged. I am grateful to Dr. Wilsun Xu for invaluable discussions, and for help on Chapter 6.

The financial assistance from Universidade Federal da Paraíba (UFPB)-Campina Grande-Brazil, where I received the support of the Department of Electrical Engineering, and from Conselho Nacional de Pesquisa (CNPq-Brazil), are gratefully acknowledged.

I am deeply grateful to my wife Catarina and my daughter Deborah for all their love, patience and help. During this time, my wife brought light through our new born Eduardo, looked after the family, and kept encouraging me.

Finally, to Kadi Purru, Cláudia Lisbôa, Cláudia Oliveira, Jane Armstrong and their families, the Soudack's and those friends who cared, my warmest thanks.

to:

Elisa Silva

and,

to the Memory of

Edison Guimarães - "Padin"

His early blindness by the sight did not prevent him from being a tireless learner of electricity and music.

Chapter 1

Introduction

1.1 Transformer Modelling

The simulation of electromagnetic transients in power systems is essential for insulation coordination studies and for the adequate design of equipment and its protection. To carry out these studies on digital computers, mathematical models are needed for the various components, whether with lumped or distributed parameters. To attempt to model each component in its entirety and then to determine its interaction with the rest of the system would be extremely difficult due to the system complexities. Models with some simplifications, which are still accurate enough for practical purposes, are therefore usually used.

The problem of accurately predicting the transient electrical interaction of power system components has faced the electric power engineer for almost a century. There is a large amount of research work in this area. The transformer is one of the most important components in power systems, and because of this, it has been given special attention [1].

Despite the large number of papers published in the area, transformer modelling still presents substantial difficulties today. Transformer inductances are nonlinear and frequency-dependent. The distributed capacitances between turns, between winding segments and between winding and ground produce resonances that may affect terminal and internal voltages [2]. The core modelling may play a very important role for ferroresonance and inrush current studies in transformers [3].

1.2 Thesis Outline

When power system transients are to be computed, general purpose programs such as the EMTP (Electromagnetic Transients Program) are often used [4]. Our goal is to advance the modelling of transformers in connection with these programs, focussing on saturation, eddy currents and hysteresis effects in the iron core. The developed models are intended to be applicable for situations such as ferroresonance and inrush currents in transformers. The models are discussed as follows:

- A brief literature review of transformer models is presented in Chapter 2.
- Saturation in the core is represented by nonlinear functions obtained from the transformer test data. The model development, measurements and simulations are discussed in Chapter 3.
- An algorithm to produce saturation curves of delta connected transformers, from positive sequence open circuit tests, is developed in Chapter 4.
- Frequency-dependent core models are presented in Chapter 5.
- In Chapter 6, distribution transformer models are obtained from 60 Hz parameters. The difficulties in obtaining the transformer parameters are outlined. Comparisons between simulations and a field test are carried out.

- The main conclusions of this thesis work are summarized in Chapter 7.

1.3 Thesis Contributions

The author believes the following to be original contributions from this research work:

a) A direct method to more accurately compute saturation curves from transformer standard test data (Chapter 3).

b) An algorithm to compute saturation curves of three-phase delta-connected transformers in which the delta connection could not be opened for tests (Chapter 4).

c) Development of frequency-dependent core models in which eddy current and hysteresis are treated simultaneously. For these models it is not necessary to pre-define the trajectories of the dynamic hysteresis loops (Chapter 5).

d) Guidelines to model distribution transformers from rated parameters (Chapter 6).

The following publications report part of the research work developed in this thesis:

1) W. L. A. Neves and H. W. Dommel, *On Modelling Iron Core Nonlinearities*, IEEE Transactions on Power Systems, Vol. 8, No. 2, May 1993, pp.417-425.

2) W. L. A. Neves, H. W. Dommel, *Saturation Curves of Delta-Connected Transformers From Measurements,* to appear in IEEE Transactions on Power Delivery. Paper 94 SM 459-8 PWRD presented at IEEE PES Summer Meeting, July 24-28, 1994, San Francisco, CA.

3) W. L. A. Neves, H. W. Dommel and Wilsun Xu, *Practical Distribution Transformer Models for Harmonic Studies*, to appear in IEEE Transactions on Power Delivery. Paper 94 SM 406-9 PWRD presented at IEEE PES Summer Meeting, July 24-28, 1994, San Francisco, CA.

Chapter 2

Literature Review And Case Studies

2.1 Introduction

A brief review of various transformer representations for digital simulation of transients in power systems, and a discussion of eddy current and hysteresis loss in magnetic cores are presented next. It is shown that an exact model which reproduces the frequency-dependent core losses, even at low frequencies, is very difficult to achieve. Sensitivity analysis for ferroresonance and transformer inrush current case studies are carried out. In these studies, the transformer core is represented by a nonlinear inductance in parallel with a constant resistance. It is shown that the system is more sensitive to variations in the core inductance. The system is not sensitive to small variations in the shunt resistance. However, typical transformer data show that no-load losses at rated frequency increase quickly as the transformer is driven into saturation. This may be significant for ferroresonance studies.

2.2 EMTP Basic Models

Guidelines to model transformers with the EMTP are presented in references [4,5]. These models are based on circuit theory. The linear behaviour of transformers can be

represented by branch resistance and inductance matrices [R] and [L] (here the exciting current must not be ignored since its absence produces infinite elements in the inductance matrix), or by a matrix [R] and an inverse inductance matrix $[L]^{-1}$. These matrices are obtained from positive and zero sequence short circuit impedances and from open circuit impedances. Saturation effects can be simulated by appending nonlinear inductance branches. In [4], it is suggested that these nonlinear branches should be placed across that branch in the equivalent circuit where the integrated voltage is equal to the iron core flux. Although this point depends on the transformer design and, in general, is not accessible in the model, it can be approximated fairly accurately by using the branch of the winding closest to the core (usually the lower voltage winding). Saturation curves of transformers are often supplied as *rms* values of voltages and currents($V_{rms}=f(I_{rms})$). A technique for converting this curve to a peak flux versus peak current characteristic($\lambda=f(i)$) is supplied by the auxiliary program CONVERT[4]. This algorithm does not take eddy currents and hysteresis losses into account, i. e., when computing saturation curves it is assumed that the excitation branch consists only of a nonlinear inductance. The next two chapters present improvements on the computation of saturation curves by including the effect of transformer no-load losses.

In the EMTP, nonlinear elements are either represented as piecewise linear or as nonlinear with the compensation method [6]. When the compensation method is used, nonlinear elements are simulated as current injections, which are superimposed on the linear network solution without the nonlinear elements. As an example, consider a case where the network contains only one nonlinear resistance between nodes **k** and **m** (Figure 2.1). The network solution is found by the compensation theorem according to the following steps:

- remove the nonlinear branch between nodes **k** and **m** and calculate the open circuit voltage v_{km_0};
- build the instantaneous Thèvenin equivalent circuit between nodes **k** and **m** (to find the Thèvenin resistance, a current of **1 A** must be injected from node **k**, and drawn out from node **m**);
- solve the two following equations simultaneously:

$$v_{km} = v_{km0} - R(t) \cdot i_{km} \tag{2.1}$$

$$v_{km} = f(i_{km}). \tag{2.2}$$

Equation (2.2) represents the nonlinear resistance characteristic. Figure 2.2 shows the simultaneous solution of the two equations above (intersection between the two curves). For nonlinear inductances, the nonlinear characteristic is usually known in the form :

$$\lambda = f(i). \tag{2.3}$$

The EMTP uses the trapezoidal rule of integration and converts the flux $\lambda(t)$ into a linear function of (t) and the network solution is found in a similar way as for a nonlinear resistance.

The saturation characteristics of modern transformers are often represented as piecewise linear inductances of two slopes (Figure 2.3). Such piecewise linear inductances can be simulated with two linear inductances L_1 and L_2 in parallel (Figure 2.4). The switch is closed whenever $|\lambda| \geq \lambda_{SATURATION}$, and is opened again as soon as $|\lambda| \leq \lambda_{SATURATION}$.

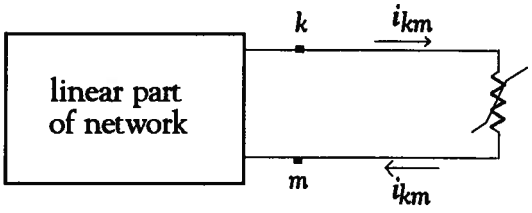

Figure 2.1: Nonlinear element connected to linear network.

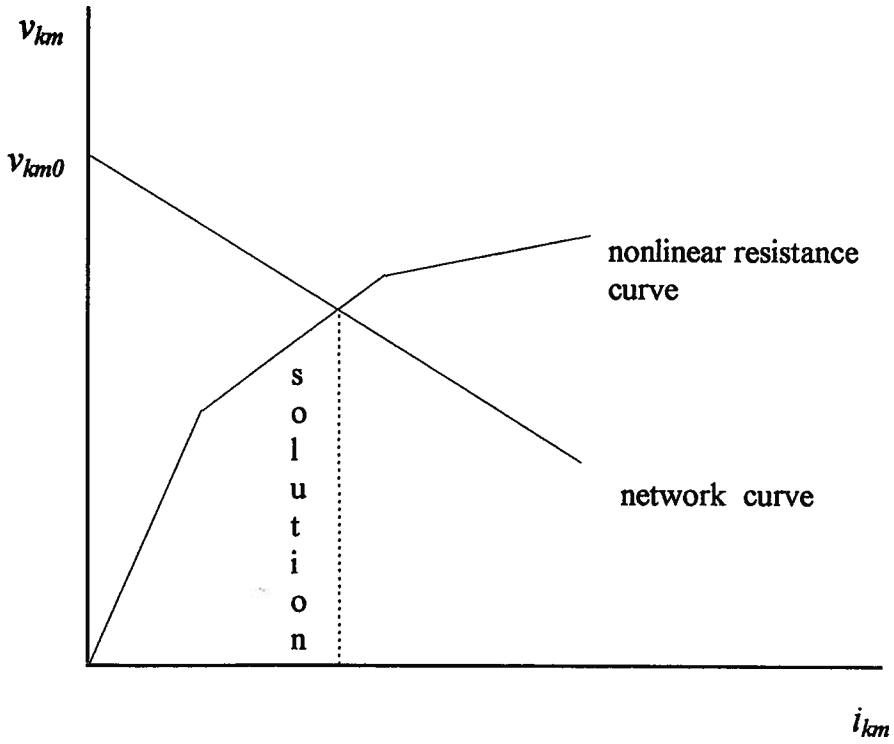

Figure 2.2: Simultaneous solution of two equations.

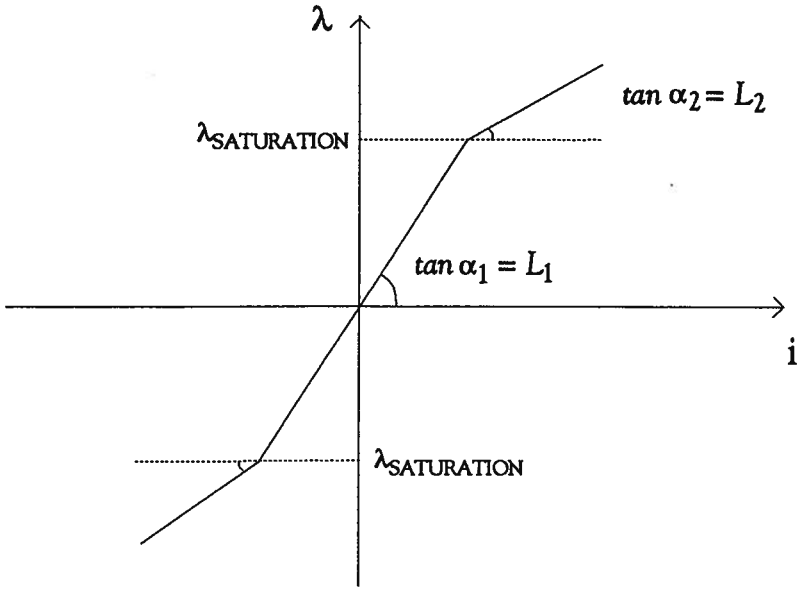

Figure 2.3 : Piecewise linear inductance with two slopes.

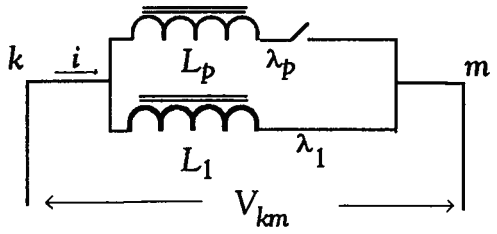

Figure 2.4 : "Switched inductance" implementation of two slope piecewise linea inductance.

Magnetic hysteresis effects have been incorporated in the BPA (Bonneville Power Administration) version of the EMTP [7]. This model uses pre-defined trajectories in the $\lambda - i$ plane to decide in which direction the curve will move if the flux either increases or decreases. Eddy current effects in the core are represented as fixed resistances. Mork and Rao [8] used this model to simulate ferroresonance and compared their results to laboratory measurements. There was a large discrepancy between measured and simulated curves. A single-valued flux-current characteristics predicted voltage and current waveforms in closer agreement to the tests. In Chapter 3, it is shown that a nonlinear resistance may be necessary to represent eddy current effects in transformers.

2.3 Other Models

Dick and Watson [9] described a method of saturating large power transformers and plotting instantaneous magnetization curves. The authors used a detailed equivalent circuit transformer model based on the principle of duality between magnetic and electric circuits which takes the yoke saturation into account. Hysteresis loops are modeled using pre-defined trajectories constructed from a hyperbolic equation.

Germay et al.[10] studied ferroresonance effects in power systems. They represented magnetic hysteresis by Preisach's theory [11,12]. This theory assumes that the ferromagnetic material is made up of elementary domains and that the magnetization characteristic of each domain is a rectangular loop characterized by the constants **a** and **b** (Figure 2.5), and by the displacement field H_m representing the action of neighboring domains. It also assumes that a distribution function, related to the probability of finding a loop with given (a,b) is unique. The distribution function can be computed numerically by manipulation of the saturation loop and magnetization curve [11]. This theory has gained large acceptance. Its basic ideas

and evolution are presented by Mayergoys [12]. Recently, a hysteresis model based on this theory was developed for the EMTP [13].

Santesmases et al.[14] represent transformer cores by a simple equivalent circuit consisting of a nonlinear inductance in parallel with a nonlinear resistance. The nonlinear elements are obtained from functions derived from the hysteresis dynamic loops. This is essentially the same model as proposed by Chua and Stromsmoe [15]. The resistance in the model accounts for the energy loss due to the loops, which means that the hysteresis and eddy current losses are assumed to have the same frequency dependence. A family of dynamic hysteresis loops is needed to construct the nonlinear functions.

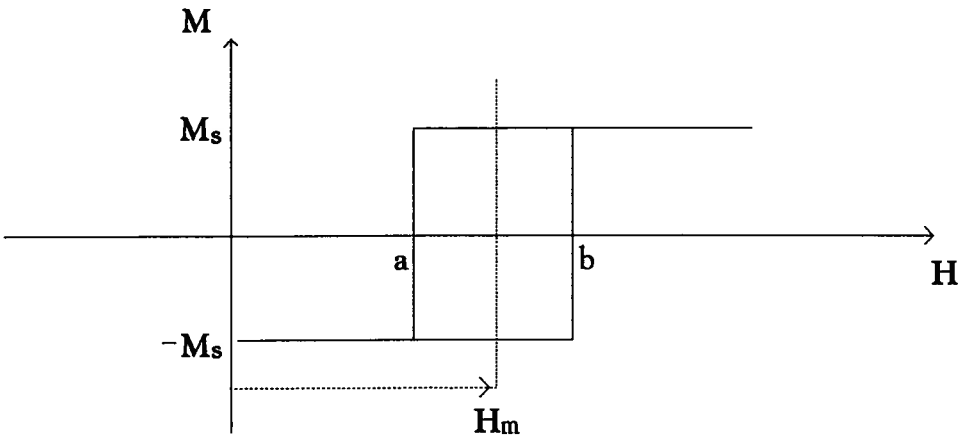

Figure 2.5 : Elementary domain hysteresis loop

A recent attempt to build a general transformer model for transient studies was sponsored by the EMTP Development Coordination Group (DCG) [16]. The principle of duality was used to model the magnetic flux paths in the air and in the iron parts. Frequency-dependent effects in the core were included by solving Maxwell's equations (in the

frequency domain) within laminations, ignoring nonlinear effects[1]. As a result, a frequency-dependent equivalent impedance $Z_{eq}(\omega)$ was found. $Z_{eq}(\omega)$ was matched by a ladder network and connected in parallel with the iron core nonlinear inductance L_l as shown in Figure 2.6.

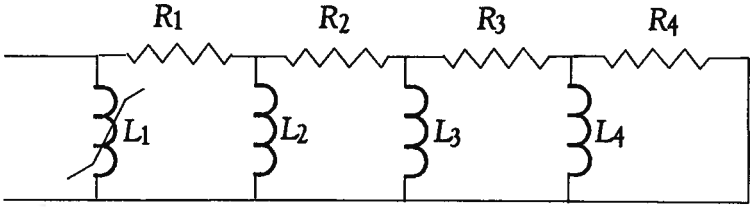

Figure 2.6 : Ladder network for eddy current representation.

The ladder network reproduces the theoretical transformer frequency response with an error less than 5% for frequencies below 200kHz. This model was applied in a situation where a circuit breaker, on the low voltage side of the transformer, attempts to clear a fault nearby [17]. The transient recovery voltage (TRV) is computed using both a frequency-dependent model for the core and the conventional model (constant resistance in parallel with the magnetizing inductance). The conventional model produced a more damped TRV.[2] It is difficult to know which model is correct since the authors did not show comparisons to field measurements.

The idea of modelling power transformer eddy current effects by means of Maxwell's equations, has also been used in references [18,19,20]. In the next section, some difficulties

[1] The ferromagnetic material was assumed to have constant permeability μ and constant resistivity σ.

[2] In reference[17] it is also shown that the conventional model is accurate enough (numerical error less than 5%) for frequencies up to 3 kHz.

concerning classical eddy current and hysteresis representations of ferromagnetic materials will be discussed.

2.4 Iron Losses

Transformer cores are usually made of iron alloys. Core materials can be divided into three major classes: non-oriented steel (hot rolled)[3], grain oriented steel (cold rolled)[4] and metallic glasses (amorphous material)[5].

Most distribution and power transformer cores in service today are of grain oriented silicon steel laminations. However, given the very low losses of amorphous alloys, the trend may change in the near future. Today, thousands of distribution transformers and a few power transformers made of metallic glasses are in service in the U.S.A., Japan and Canada [22].

In the presence of a time-varying magnetic field, induced voltages, eddy currents and hysteresis take place in the core material. Classical electromagnetic theory assumes a uniform distribution of eddy currents when slowly time-varying magnetic fields are applied to iron cores (Figure 2.7a). The first theoretical studies of eddy currents in iron sheets were done by Oliver Heaviside followed by J. J. Thomson [24]. The iron was assumed to be a homogeneous medium characterized by two constants: permeability μ and conductivity σ.

---

[3] Non-oriented grades of electrical sheets are designed to have the same magnetic properties in the rolling direction as they have perpendicular to that direction. They were largely used in the past for power and distribution transformer cores.

[4] Cold rolled materials were introduced to the market in 1934 by N. P. Goss [21]. Their permeabilities are much bigger in the direction of rolling than perpendicular to that direction. Core laminations are usually cut so that the magnetic flux is along the rolling direction for the greatest part of its path through the core. These materials have lower losses when compared to non-oriented steels.

[5] Fe-Si-B alloys were introduced to the transformer market in the U.S.A. in 1976 [22]. These alloys present higher resistivity, when compared to grain oriented steels, and very low losses.

The electromagnetic theory (Maxwell's equations) was applied to show how the magnetic flux density B would diffuse from one part of the material to the other according to the equation

$$\nabla^2 B = \mu\sigma\frac{\partial B}{\partial t}. \tag{2.4}$$

The equation above oversimplifies a much more complicated phenomenon.[6] Core losses, computed by this approach, are always underestimated when compared to measured values. A detailed review of eddy current and hysteresis loss in magnetic cores is presented in [25]. Weiss, Barkhausen, Bitter, Landau and Liftshitz made significant contributions towards the understanding of eddy current effects in ferromagnetic materials. In 1907, the French physicist Pierre Weiss provided the first insight into understanding the behavior of magnetic materials. He introduced the concept of magnetic domains. In 1919 Barkhausen had shown that the magnetization could change in a very discontinuous way (Barkhausen effect). 1n 1931, Francis Bitter, working at the Westinghouse Research Laboratories proved the existence of domains by making them visible. His technique consists of polishing the surface of the magnetic material and spreading a colloidal suspension of magnetic powder over the surface. The powder will be deposited in regions of higher gradient fields (domain boundaries) and the domains are then visible through a microscope[21]. In 1935, Landau and Lifshitz introduced the ideas that magnetization could change by a movement of the boundary between domains, and that domains magnetized in the direction of the applied field would expand at the expense of domains magnetized against the applied field. Today, it is

[6] When Maxwell died in 1879, he left his theory in the form of twenty equations in twenty variables. Shortly after his death, the reduction of his equations to the four vectorial equations known today was done independently by Oliver Heaviside and Heinrich Hertz [23]. At that time, very little was known about ferromagnetism. Eddy currents in ferromagnetic materials were assumed to behave the same way as in non-magnetic conductors.

generally accepted that the eddy current loss is due to the micro eddy currents produced at the moving domain boundaries. Therefore, eddy currents will be concentrated around the moving domain walls, as shown in Figure 2.7b. The bigger the domain the larger the eddy currents produced around its boundaries. Eddy current distribution may not be uniform even for very slowly time-varying magnetic fields.

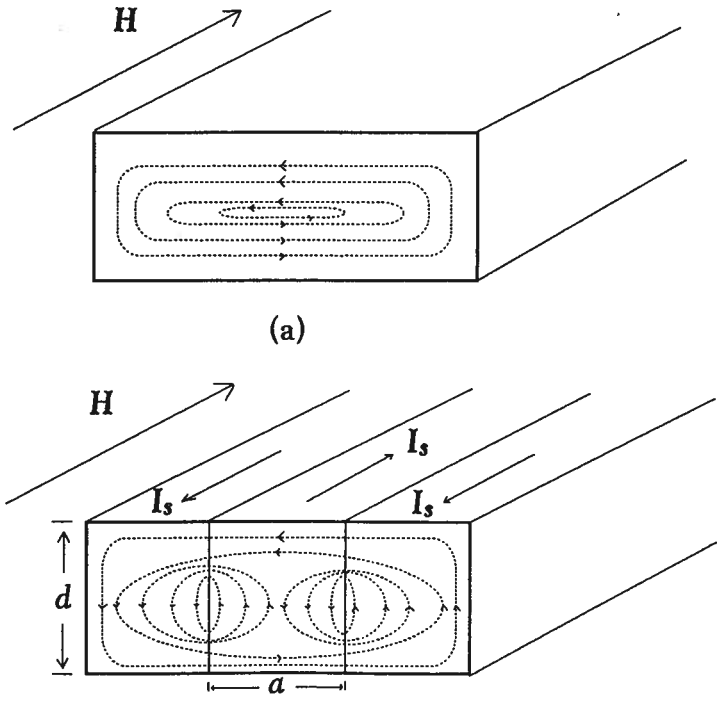

Figure 2.7 : Eddy current distribution in a ferromagnetic sheet of thickness d:
(a) Classical representation;
(b) Sheet subdivided into 180^0 domain of width a.

It is very complicated to properly use Maxwell's equations within iron core laminations to account for eddy currents. For a precise calculation, the effect of domain wall motion should somehow be included in the field equations [26, 27, 28].

The loss in a ferromagnetic sheet at a frequency f, consists of hysteresis and eddy currents. The total loss is always greater than would be expected from the sum of static hysteresis loss and eddy current loss, calculated using classical theory [29,30]. The excess loss, arising from the non-uniform distribution of eddy currents, is known as anomalous loss.[7] Since, in practice, only the total loss w can be measured, assumptions must be made based on the most probable physical behavior of the material if hysteresis and eddy current loss are to be separated. The total loss per kilogram, per volume of magnetic material, in an iron sample can be written as a combination of three loss components:

$$w = w_h + w_e + w_a \,, \tag{2.5}$$

where w_h , w_e and w_a are hysteresis, eddy current and anomalous loss, respectively, in W/kg. It is well known that the total loss w is frequency-dependent. Hysteresis loss is attributed to domain wall movements back and forth across crystal grain boundaries, non magnetic inclusions and imperfections [21]. It is common to assume that w_h is independent of the speed in which the domain wall moves. So, the hysteresis loss per magnetic volume at a given frequency f is related to the enclosed area of the DC hysteresis loop (Figure 2.8) according to the equation:

$$w_h = f \oint H dB. \tag{2.6}$$

---

[7] Electrical Engineering textbooks, usually address the magnetic domain theory to explain the properties of magnetic materials, but seldom relate the domain wall movements to eddy currents. Anomalous losses were known even before the domain theory was completed. In 1927, it was already known that there is a strong correlation between grain size and eddy current losses [31].

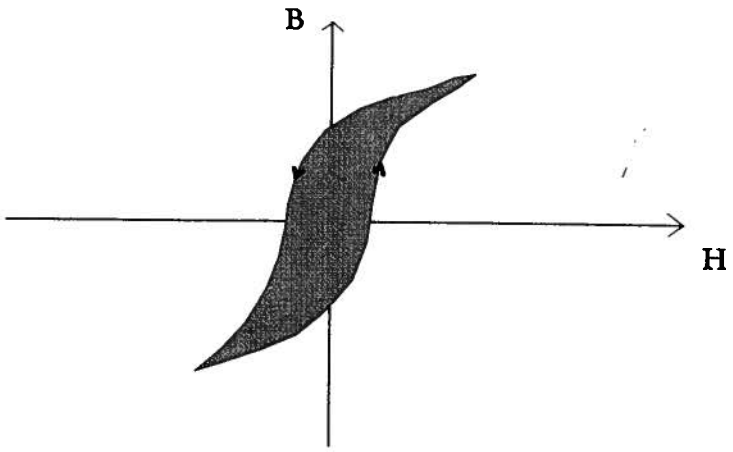

Figure 2.8: Hysteresis loops. In the B - H plane, the trajectory of a signal of frequency f, will encircle the hatched area (DC hysteresis loss) f times per second.

Any increase in loss per cycle above the DC hysteresis loss has been attributed to eddy current effects [22]. Steinmetz [28] proposed the following equation for calculation of the hysteresis loss:

$$w_h = k_h \cdot B_m^x \cdot f, \tag{2.7}$$

where

k_h is the hysteresis coefficient and depends on the core material;

B_m is the maximum flux density in Teslas; and

x is the Steinmetz coefficient (ranging from 1.5 to 2.2 depending on the core material).

The principal means of controlling the core loss is to use thin laminations. For a lamination in which its thickness t_d is much smaller than its width, the classical eddy current loss is given by [22]:

$$w_e = (\pi \cdot t_d \cdot B_m \cdot f)^2 / (6\rho), \tag{2.8}$$

where ρ is the resistivity of the material, and t_d is the lamination thickness. Inserting equations (2.7) and (2.8) into (2.5) and dividing by f, the total loss per cycle is given by:

$$\frac{w}{f}=k_h \cdot B_m^x+(\pi \cdot t_d \cdot B_m)^2 \cdot f/(6\rho)+w_a/f$$

A typical curve of power loss per cycle as a function of frequency, for a constant flux amplitude, is shown in Figure 2.9. The anomalous loss can be very high (usually greater than the classical eddy loss for commercial steel at power frequency [26]).

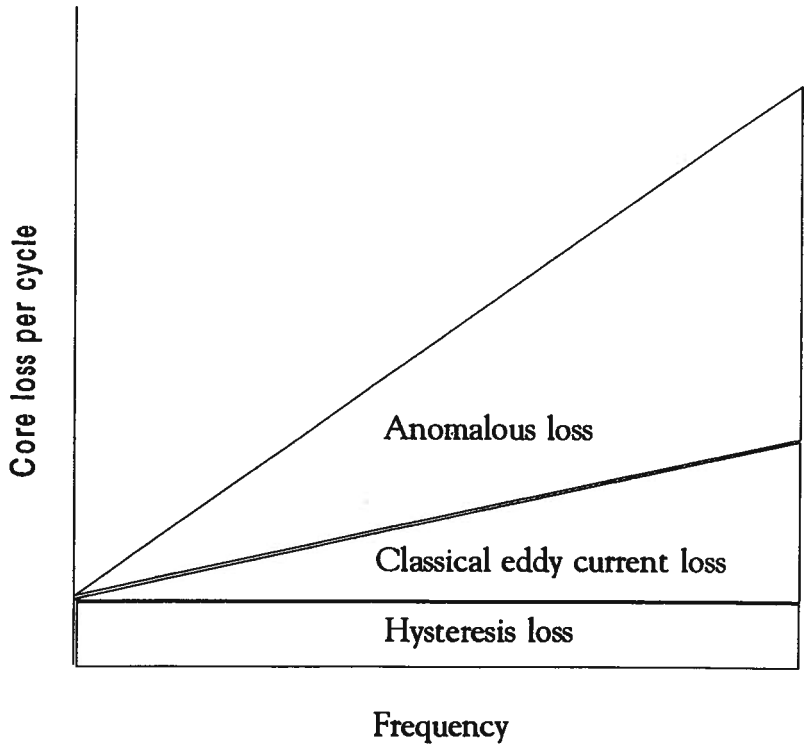

Figure 2.9: Typical steel laminations power-loss curve.

2.4.1 Laboratory Measurements

As part of this thesis project, some measurements were performed for grain oriented steel laminations to gain some insight into how eddy currents and hysteresis loss behave as the frequency changes. The steel samples were assembled in a standard Epstein frame [33]. The amplitude B_m of the sinusoidal flux density $B=B_m \sin \omega t$ was kept constant during each set of measurements.

Figure 2.10 illustrates the circuit used to measure the total AC core loss for a frequency range from a few hertz up to 80 Hz. V(t) is a frequency variable sinusoidal voltage source connected to a power amplifier. A waveform analyzer was used to measure the voltages at points A and B with respect to ground. The current sample waveform was taken from a 0.1Ω resistance R connected in series with the Epstein frame primary winding. Current and voltage waveforms (512 points) were obtained and the losses were computed using a built-in routine. The total loss per cycle, as a function of frequency for B_m=1.0T, is shown in Figure 2.11. The laminations were 0.3mm thick, with $\rho = 4.5 \times 10^{-7} \Omega \cdot m$. The solid line, through the measured points, is a second order polynomial approximation. This curve is extended downwards to f=0. At f=0, it is assumed that the loss per cycle is the DC hysteresis loss. The classical eddy curent loss is computed using (2.8) and added to the hysteresis loss. The losses per cycle calculated by the classical approach are lower than the measured ones. The hysteresis loss per cycle at 60 Hz accounts for about half of the total loss. Reference [32] quotes measurements in grain oriented steel laminations in which the anomalous loss could be close to an order of magnitude higher than the classical eddy current losses for frequencies up to 1 kHz. Herzer and Hilzinger [34] show examples of amorphous alloys with large anomalous loss (nealy 40% of total loss) at frequencies of 100 kHz.

It is complicated to predict losses in iron cores accurately. A better understanding of loss mechanism in ferromagnetic materials is providing researchers with the tools to reduce them. Theoretically, the classical methods would be applied properly if the laminations were made of a fine domain structure. Researchers are struggling to reduce the total loss and increase permeability of ferromagnetic steels. Very high permeability low loss steel sheets are on the market today. Nevertheless, although total losses are low, anomalous loss is still high when compared to the classical eddy current loss [22].

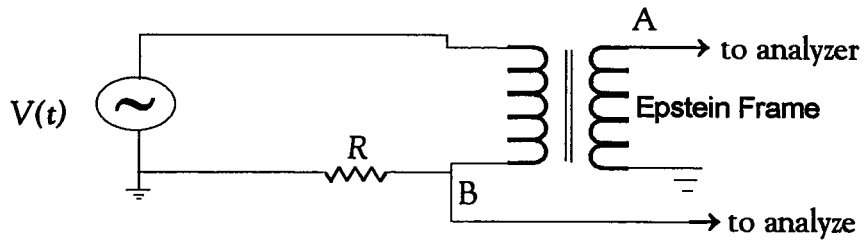

Figure 2.10 : AC core loss measurements.

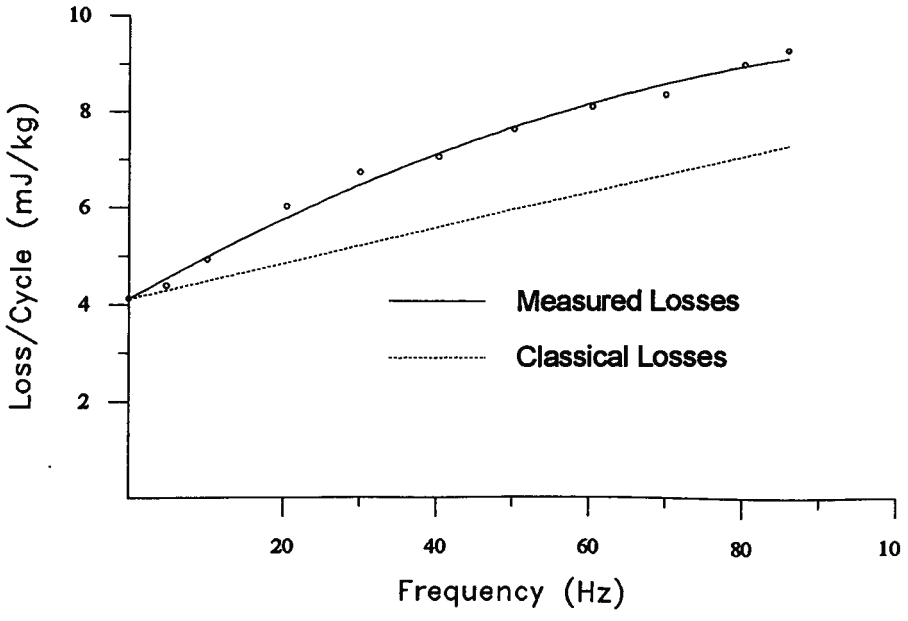

Figure 2.11: Power-loss curve for commercial Grain oriented steel lamination.

2.4.2 Building Factor

There is also a further complication that transformer core loss per kilogram is always greater than the nominal loss of the steel as measured in standard testers. The ratio between the transformer per unit loss and the nominal or standard unit loss is called the "building factor" of the core. Building factors usually range from 1.1 to 2.0 [35]. The extra loss is due to phenomena such as:

- Non-uniform flux distribution due to difference in path lengths among magnetic circuits;
- Distortion of flux waveform due to magnetic saturation;
- Flux directed out of the rolling direction;
- Transverse flux between layers due to joints.

The flux distribution in transformer laminations is not uniform even at low frequencies [36,37,38]. For a sinusoidal applied flux, the flux in each lamination is not sinusoidal, although the flux components add up to produce the sinusoidal total flux.

Advances in computer software have been used to improve the design of electrical machinery [39]. There are several commercial programs available today [40]. They are essentially useful for situations in which qualitative results are important (for instance, in designing transformer lap joints, it is important to find the geometry of the joints that leads to minimum losses). The accuracy of the present methods needs verification against experiments [35].

2.5 Transformer Core Representation During Transients

The major nonlinear effects in transformers are saturation, eddy currents and hysteresis. Saturation is the predominant effect [41]. In the following sections, ferroresonance and inrush current simulations will be addressed. The transformer excitation branch is represented by a crude model (constant resistance in parallel with a nonlinear inductance). Sensitivity studies are carried out to analyze how the system responds to changes in the core model parameters.

2.5.1 Ferroresonance Case Study

Consider the BPA (Bonneville Power Administration) 1100kV test system [42]. It comprises a generating station, a transformer bank (autotransformers) and a short three-phase transmission line. Field tests were carried out. Ferroresonance occurred in phase A when this phase was switched off on the low voltage side of the transformer (Figure 2.12). Phase C was not yet connected to the transformer at that time. One can study this case, replacing the dotted part of the network by its Thèvenin equivalent circuit, which consists of a voltage source behind a capacitance (crude representation of the capacitive coupling to phase A of the line). Figure 2.13 is the equivalent circuit of the system referred to the high voltage side. The nonlinear inductance characteristic shown in Figure 2.14 (three straight line segments) was obtained from the V_{rms}-I_{rms} curve supplied by the transformer manufacturer, using the method of [4]. Unfortunately, the transformer no-load data were produced by exciting voltages that did not go beyond 1.1 p.u., and data at higher saturation levels would be needed for this case. Autotransformers have typical air core inductances (the core is completely saturated and it behaves like air) of 3 to 4 times the short circuit inductance [4]. A straight line segment, with a slope of 4 times the short circuit inductance was connnected to the last segment of Figure 2.14, to represent the air core inductance. The

Microtran® program[43] was run twice for different values of core resistance ($R=R_C$ and $R=0.8R_C$, where $R_C=4.2M\Omega$ is the resistance at the rated voltage). A time step of $\Delta t=100\mu s$ was used in each case. Both simulations, of the terminal voltage at phase A, are shown in Figure 2.15. The two curves are almost identical.

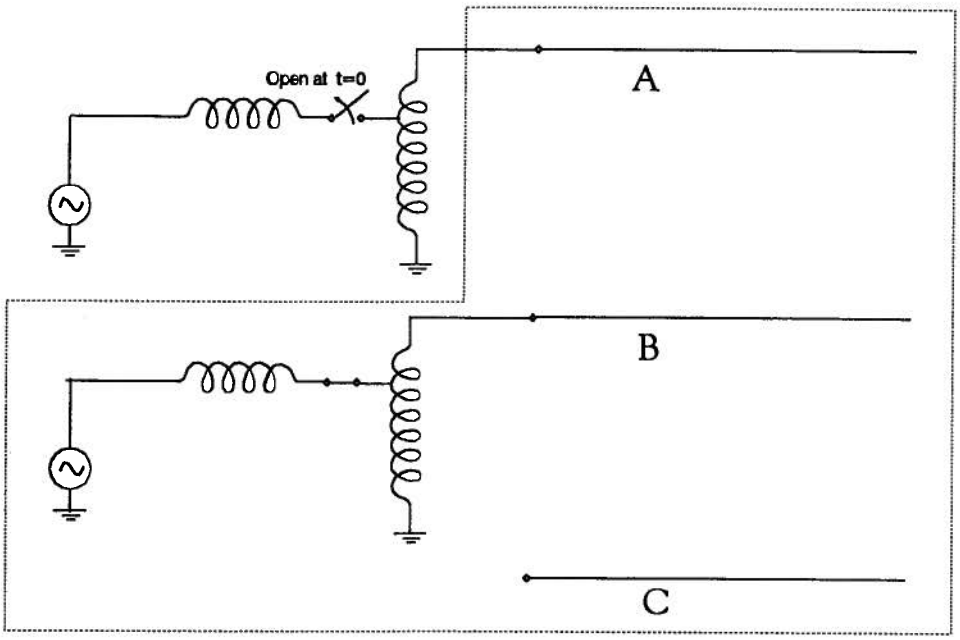

Figure 2.12: Ferroresonance in a 1100kV test system.

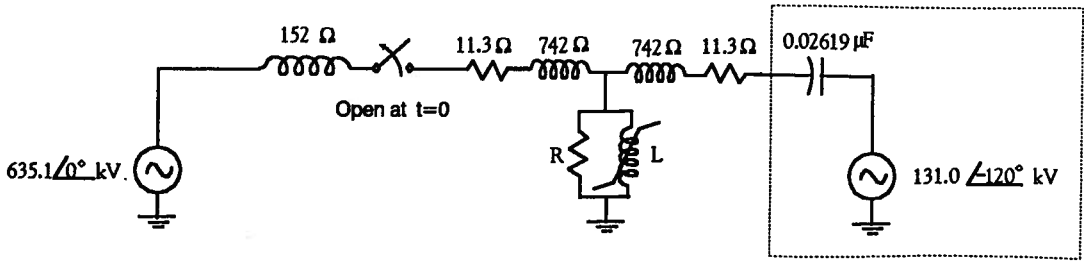

Figure 2.13 : Thèvenin equivalent circuit.

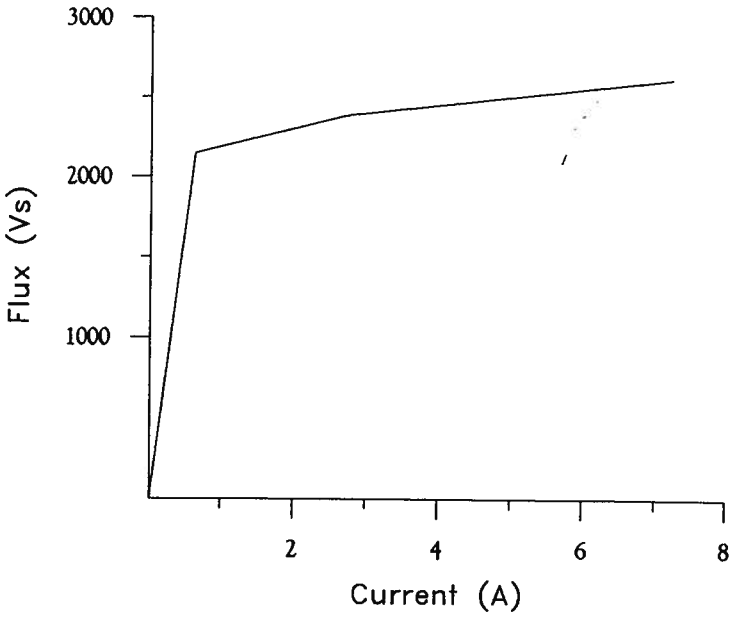

Figure 2.14 : Nonlinear inductance characteristic referred to the 1100 kV side.

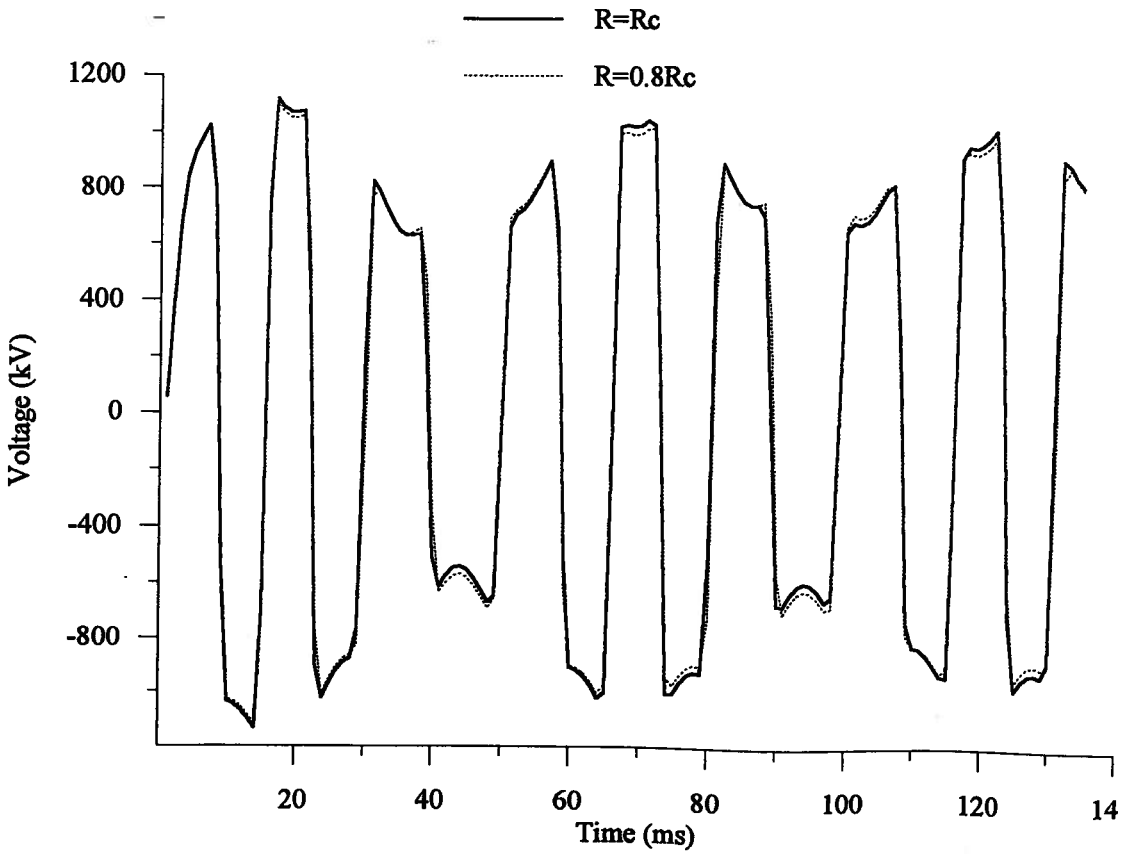

Figure 2.15: Voltage at phase A (sensitivity study for changes in core resistance).

The Microtran program was run again, now with the slope of the air core inductance made 20% smaller. The results are shown in Figure 2.16, where the solid curve is the same curve of Figure 2.15 for $R=R_C$. It is seen that the simulated system is more sensitive to variations in the nonlinear inductance than to core losses.

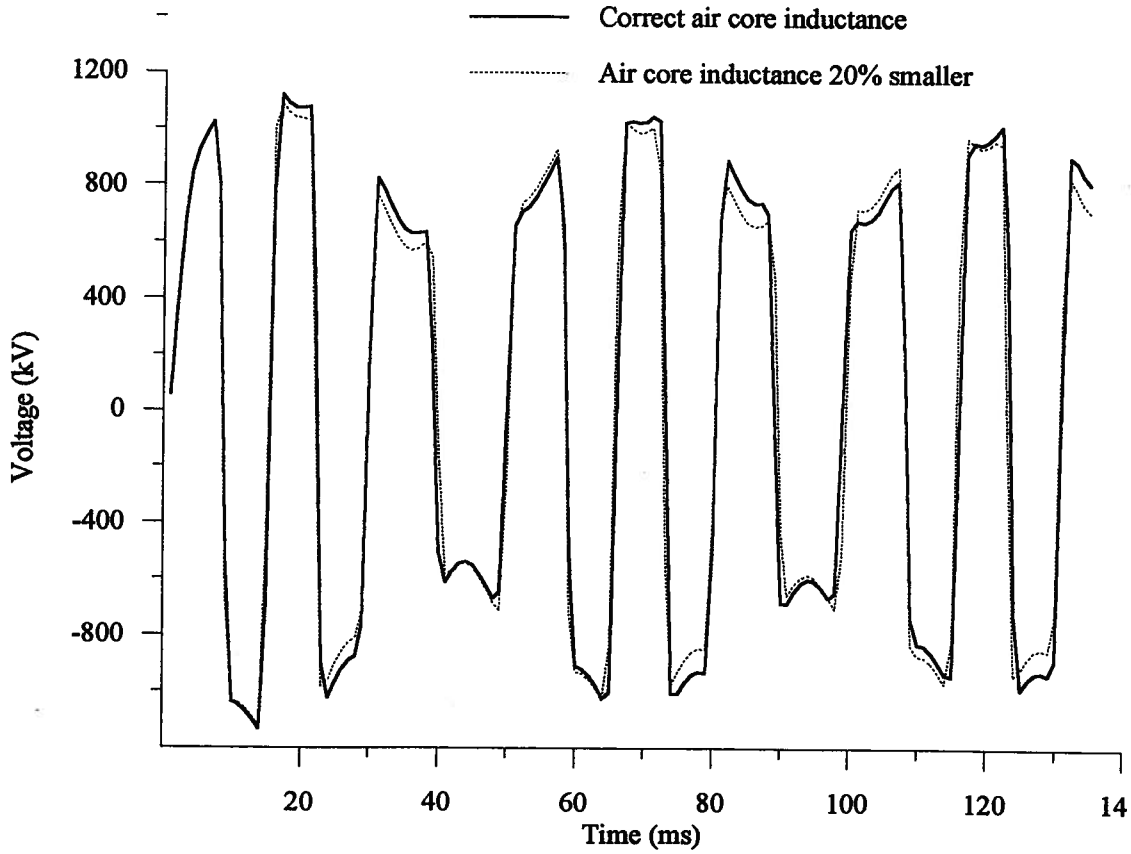

Figure 2.16: Voltage at phase A (sensitivity study due to variations in the air core inductance).

2.5.2 Inrush Current Case Study

Now consider the analysis of inrush current simulations in a single phase transformer (same transformer data of the previous section). The aim here is to see how sensitive the current waveforms are to changes in the core resistance and nonlinear inductance (Figure

2.17). The plot of the inrush current for three values of core resistance ($R=R_C$, $R=0.5R_C$ and $R=\infty$) and the nonlinear inductance of the previous example, is shown in Figure 2.18. The solid curve represents in fact any of the simulations. It was assumed that no transformer residual flux existed prior to energization at t=0. In these simulations, inrush currents are not sensitive to variations of the core resistance. However, if the slopes of the flux-current characteristic above the rated flux were changed by 10% (dashed curve), a noticeable difference between the current waveforms would be seen. In these simulations, inrush currents are shown to be very sensitive to variations of the nonlinear inductance.

2.6 Summary

This chapter summarized the difficulties in modelling transformer cores. Their exact representation during transients is complex since the magnetic properties of the cores are not yet fully understood. Another major problem is the availability of data. All that is usually available from transformer manufacturers are data obtained from tests performed at rated frequency [46,47,48]. The information available from open circuit tests are *rms* voltages as a function of *rms* currents, and no-load losses for a few input voltage levels.

In the simulation examples of Section 2.4, a constant resistance was used to reproduce the transformer core loss. It was shown that the system is not sensitive to small variations in the resistance. In practice, however, this resistance is not linear. Typical distribution transformer correction factors are shown in Table 2.1 [44]. They should be applied to no-load losses, at rated voltage, to give the correct losses when the transformer is driven into saturation. The equivalent resistance, which reproduces the open-circuit losses, decreases as the voltage level increases beyond the rated voltage (losses increase at faster rate than the square of the voltage). For 225 kVA and above (three-phase transformers), the open circuit equivalent resistance is equal to approximately half of the resistance at rated

voltage. This may make a difference during ferroresonance studies. Another complication is that the core loss is frequency-dependent [29,38,49].

Table 2.1 - Typical distribution transformer data.

Operating Voltage (%)	Correction Factors	
105	1.15	For 167 kVA and below, 1 phase
110	1.30	For 150 kVA and below, 3 phase
105	1.5	For 225 kVA and above, 1 phase
110	2.4	For 225 kVA and above, 3 phase

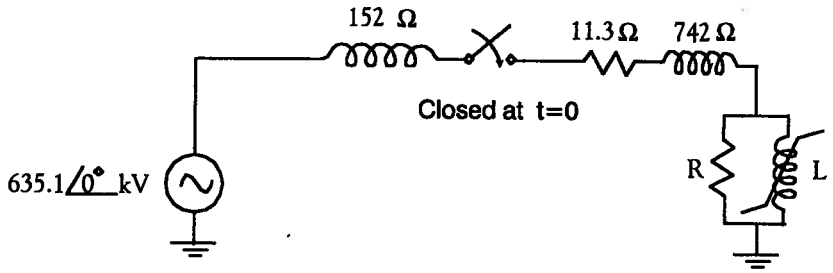

Figure 2.17: Energization of a transformer.

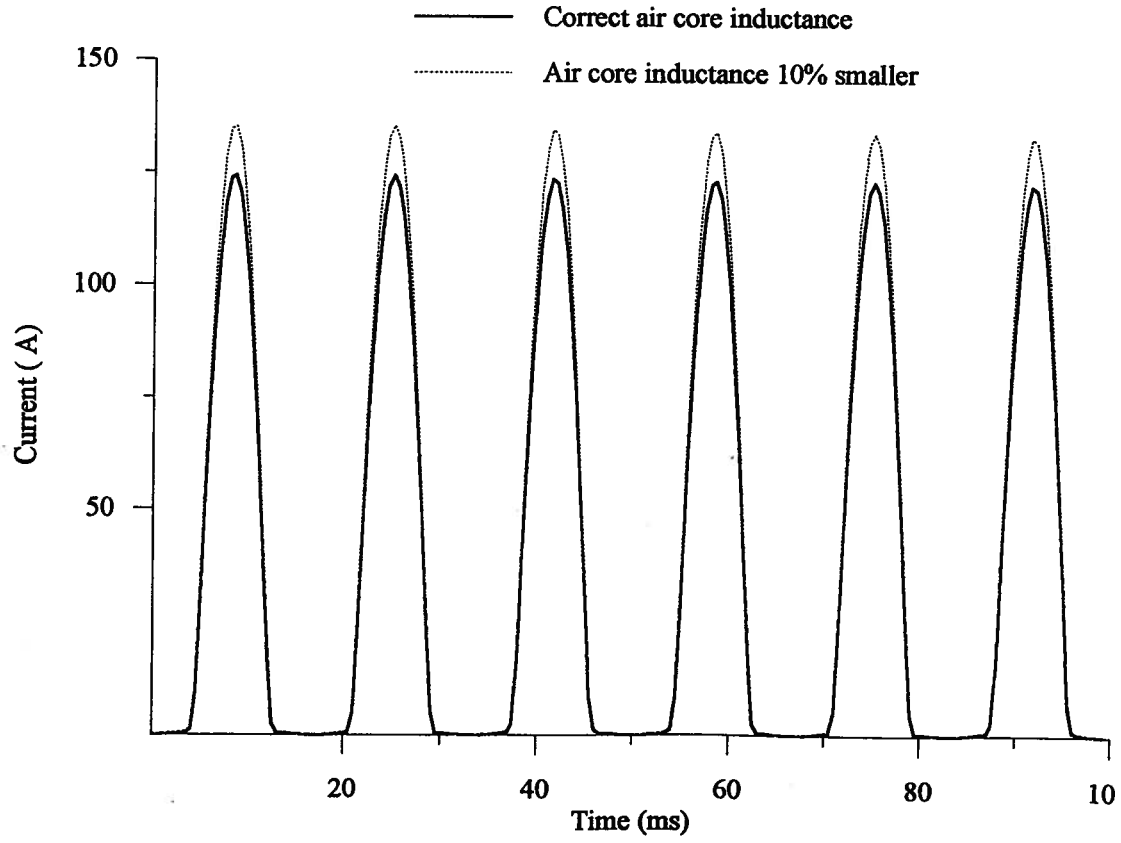

Figure 2.18: Inrush current (sensitivity study).

Chapter 3

On Modelling Iron Core Nonlinearities

3.1 Introduction

Transformer manufacturers usually supply saturation curves in the form of *rms* voltages as a function of *rms* currents. Some methods have been used to convert these $_{rms}-I_{rms}$ curves into peak flux - peak current curves (nonlinear inductances) [4, 45, 51]. As shown later, these methods can be modified to take iron core losses into account, thereby producing a nonlinear inductance as well as a parallel nonlinear resistance.

In addition, laboratory experiments were performed with a silicon iron steel core assembled in an Epstein frame. Average power and *rms* current at 60 Hz were measured at different voltage input levels. For comparison purposes, the initial magnetization curve for the core material was measured as well.

Simulations of ferroresonance in a power system are carried out to examine the effect of the transformer nonlinearities on its terminal voltage waveform. These simulations are compared to a field test.

The algorithm is applied to distribution transformers to get their open circuit nonlinear parameters. Measurements have shown that there are newly manufactured transformers in which their excitation currents at rated voltage are smaller than their excitation currents at lower voltages. For these transformers, improvement on the computed saturation curves would be accomplished by modifying the algorithm to include the effect of stray capacitances.

3.2 Saturation Curves

The cores of transformers and reactors are sometimes represented as an equivalent circuit consisting of a nonlinear inductance ($\lambda - i_l$ curve) in parallel with a nonlinear resistance ($v - i_r$ curve) [14, 15]. The characteristics of these elements are obtained from the dynamic hysteresis loops. The resistance in this model accounts for the energy losses due to the loops. Chua and Stromsmoe [15] did make comparisons between simulations and laboratory tests for a small audio transformer, and for a supermalloy core inductor as well. A family of peak flux - peak current loops for 60, 120 and 180 Hz sinusoidal (voltages and current) excitations of various amplitudes were obtained. The agreement between simulations and measurements of the loops was very good. This indicates that, for the frequencies under consideration, a nonlinear resistance would represent hysteresis and eddy current effects reasonably well.

The same equivalent circuit is used here. However, the nonlinear characteristics are calculated in a simpler way directly from the transformer test data. The nonlinear resistance (piecewise linear $v - i_r$ curve) is found from the no-load (excitation) losses. This information is then used to compute the current through the nonlinear inductance and to construct the piecewise linear $\lambda - i_l$ curve.

Figure 3.1(a) shows a voltage source connected to a single-phase transformer whose excitation branch is represented by a nonlinear inductance in parallel with a nonlinear resistance. Their nonlinear characteristics are computed according to the following assumptions:

- the $v-i_r$ and $\lambda-i_l$ curves (Figures 3.1(b) and 3.1(c)) are symmetric with respect to the origin (R_k and L_k are the slopes of segment k of the $v-i_r$ and $\lambda-i_l$ curves, respectively);

- the no-load test is performed with a sinusoidal voltage source; the winding resistances and leakage inductances are ignored.

The conversion algorithm works as follows:

For the construction of the $v-i_r$ curve (Section 3.2.1):

- compute the peak values of the current $i_r(t)$ point by point from the no-load losses, and subsequently compute their *rms* values I_{r-rms}.

For the construction of the $\lambda-i_l$ (Section 3.2.2):

- obtain the *rms* values I_{l-rms} of the current $i_l(t)$ through the nonlinear inductance from I_{r-rms}, the total *rms* I_{t-rms} current and the applied voltage $v(t)$;

- compute the peak values of the inductive current $i_l(t)$ point by point from their *rms* values and *rms* voltages.

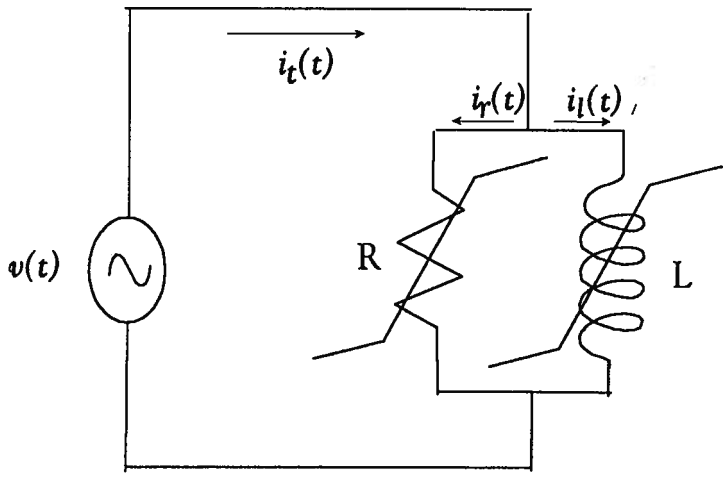

(a)

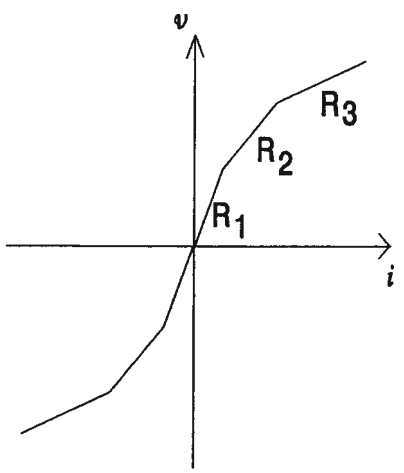

(b)

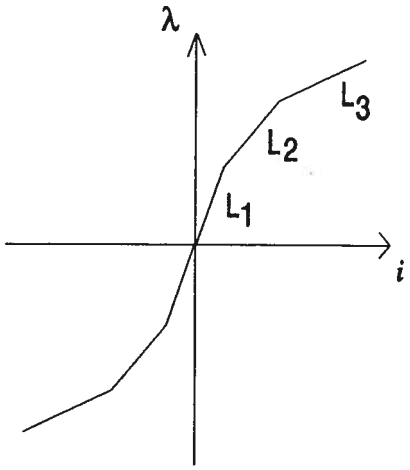

(c)

Figure 3.1: Excitation test:
(a) core representation;
(b) $v-i_r$ characteristic;
(c) $\lambda-i_l$ characteristic.

3.2.1 Computation of the v - i_r Curve

Let us assume that the no-load losses P_1, P_2,..., P_m are available as a function of the applied voltage $_{rms_1}$, V_{rms_2}, ..., V_{rms_m} as shown in Figure 3.2.

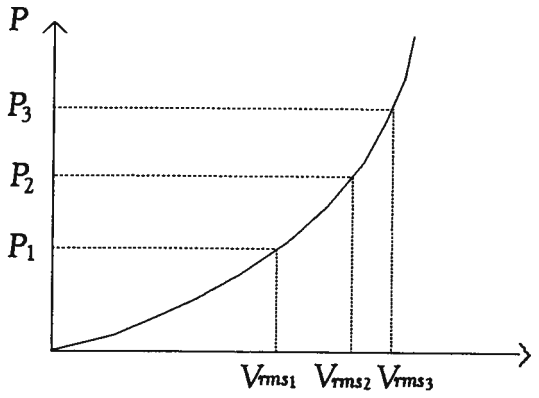

Figure 3.2 : V*rms* - Average Power curve

From these data points we want to construct a piecewise linear resistance curve, as shown in Figure 3.3(b), which would produce these voltage dependent no-load losses. Let us first explain how the no-load losses can be obtained from a given $v-i_r$ curve, before describing the reverse problem of constructing the $v-i_r$ curve from the given no-load losses at rated frequency. For instance, assume that the applied voltage is $_{rms_2}$ and varies sinusoidally as a function of time, as shown in Figure 3.3(a), with

$$v_2(\theta) = V_2 \sin\theta \tag{3.1}$$

where $_2 = V_{rms_2}\sqrt{2}$. Because of the symmetry of the $v-i_r$ curve with respect to the origin, it is sufficient to observe 1/4 of a cycle, to $\theta = \pi/2$. From Figure 3.3, it can be seen that :

$$i_{r_2}(\theta)=\begin{cases} (V_2 \sin\theta)/R_1 & \text{if } \theta<\theta_1 , \\ I_{r_1}+(V_2 \sin\theta - V_1)/R_2 & \text{if } \theta_1 \le \theta \le \frac{\pi}{2}. \end{cases}$$

In general, $i_r(\theta)$ can be found for each $v(\theta)$ through the nonlinear $v-i_r$ characteristic, either graphically (as indicated by the dotted lines in Figure 3.3), or with equations. This will give us the curve $i_r(\theta)$ over 1/4 of a cycle, from which the no-load losses are found as

$$P=\frac{2}{\pi}\int_0^{\frac{\pi}{2}} v(\theta) i_r(\theta)\, d\theta \tag{3.2}$$

Let us now address the reverse problem, i.e., constructing the $v-i_r$ curve from the given no-load losses. Obtaining the points $_1, V_2, \ldots, V_m$ on the vertical axis of Figure 3.3(a) is simply a re-scaling procedure from *rms* peak values,

$$_k = V_{rms_k}\sqrt{2}, \tag{3.3}$$

for k = 1,2,3, ..., m. For the first linear segment in the $v-i_r$ curve, the calculation of the peak current I_{r_1}, on the horizontal axis is straightforward. Since $P_1 = V_{rms_1} I_{rms_1}$, in the linear case,

$$I_{r_1}=\frac{2P_1}{V_1}.$$

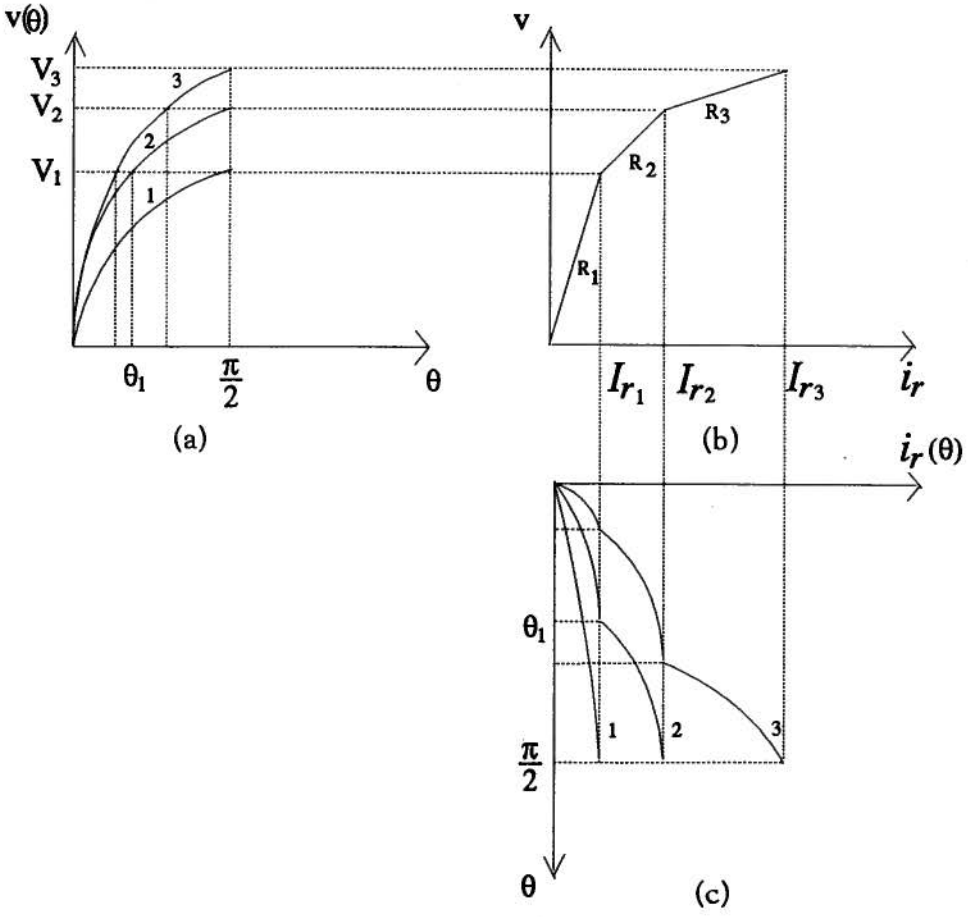

Figure 3.3: Computation of the nonlinear resistance:
(a) sinusoidal voltage input signal;
(b) $v - i_r$ curve to be computed;
(c) output current.

For the following segments ($k>2$), we must use the power definition of equation (3.2), with the applied voltage $v(\theta)=V_k \sin\theta$ (Figure 3.3a). Then

$$P_k=\frac{2}{\pi}\left[\int_0^{\theta_1}(V_k\sin\theta)\left(\frac{V_k\sin\theta}{R_1}\right)d\theta+\right.$$
$$\int_{\theta_1}^{\theta_2}(V_k\sin\theta)\left(I_{r_1}+\frac{V_k\sin\theta-V_1}{R_2}\right)d\theta+\cdots+ \tag{3.5}$$
$$\left.\int_{\theta_{k-1}}^{\frac{\pi}{2}}(V_k\sin\theta)\left(I_{r_{k-1}}+\frac{V_k\sin\theta-V_1}{R_k}\right)d\theta\right].$$

The "break points" θ_1, θ_2, ..., θ_{k-1} in equation (3.5) are known from

$$\theta_j=\arcsin(V_j/V_k), \tag{3.6}$$

for $j=1, 2, \ldots, k-$. The only unknown in equation (3.5) is the slope R_k in the last segment. The average power can therefore be rewritten in the form

$$P_k=a_{r_k}+\frac{b_{r_k}}{R_k}, \tag{3.7}$$

with a_{r_k}, b_{r_k} and P_k known values. R_k is then easily computed and I_{r_k} is calculated from

$$I_{r_k}=I_{r_{k-1}}+\frac{V_k-V_{k-1}}{R_k}. \tag{3.8}$$

This computation is done segment by segment, starting with I_{r_2} and ending with the last point I_{r_m}. Whenever a point I_{r_k} has been found for the horizontal axis in Figure 3.3b, its *rms* value is calculated as well, because it is needed later for the construction of the $\lambda-i_l$ curve. I_{r-rms} is found from the definition of the *rms* value,

$$I_{rms}^2 = \frac{2}{\pi}\int_0^{\frac{\pi}{2}} i^2(\theta)\,d\theta \tag{3.9}$$

i.e.,

$$I_{r-rms_k}^2 = \frac{2}{\pi}\left[\int_0^{\theta_1}\left(\frac{V_k \sin\theta}{R_1}\right)^2 d\theta + \int_{\theta_1}^{\theta_2}\left(I_{r_1} + \frac{V_k \sin\theta - V_1}{R_2}\right)^2 d\theta + \cdots + \int_{\theta_{k-1}}^{\frac{\pi}{2}}\left(I_{r_{k-1}} + \frac{V_k \sin\theta - V_1}{R_k}\right)^2 d\theta\right]. \tag{3.10}$$

3.2.2 Computation of the λ - i_l curve

The $\lambda - i_l$ curve is computed using the *rms* current information from the $v - i_r$ curve. Peak voltages are converted to peak fluxes and the *rms* values of the current through the nonlinear inductance are converted to peak values.

The conversion of peak voltages V_k to peak fluxes λ_k is a re-scaling procedure. Hence, for each linear segment in the $\lambda - i_l$ curve,

$$\lambda_k = \frac{V_k}{\omega}, \tag{3.11}$$

where ω is the angular frequency.

Let us now compute the peak values of the inductive current. At first, their *rms* values are evaluated. It can be shown that for sinusoidal input voltages, the harmonic components of the resistive current are orthogonal to their respective harmonic components of the inductive current (see Appendix A). Then,

$$I_{l-rms}=\sqrt{I_{t-rms}^2-I_{r-rms}^2}\ , \tag{3.12}$$

with the resistive current I_{r-rms} already computed from equation (3.10) and the total current I_{t-rms} known from the transformer test data. For the first linear segment in the $\lambda-i_l$ curve,

$$I_{l_1}=I_{l-rms_1}\sqrt{2}. \tag{3.13}$$

For the following segments $k\geq 0$, the peak currents are obtained by evaluating I_{l-rms} for each segment k, using equation (3.9). Thus, assuming $\lambda_k(\theta)=\lambda_k\sin\theta$, we have[1]

$$\begin{aligned} I_{l-rms_k}^2=\frac{2}{\pi}\Bigg[&\int_0^{\theta_1}\left(\frac{\lambda_k\sin\theta}{L_1}\right)^2 d\theta+\\ &\int_{\theta_1}^{\theta_2}\left(I_{l_1}+\frac{\lambda_k\sin\theta-\lambda_1}{L_2}\right)^2 d\theta+\cdots+\\ &\int_{\theta_{k-1}}^{\frac{\pi}{2}}\left(I_{l_{k-1}}+\frac{\lambda_k\sin\theta-\lambda_{k-1}}{L_k}\right)^2 d\theta\Bigg] \end{aligned} \tag{3.14}$$

Here, similarly to the case of the $\nu-i_r$ curve computation, only the last segment L_k of equation (3.14) is unknown. Equation (3.14) can be rewritten in the form

$$a_{l_k}\Gamma_k^2+b_{l_k}\Gamma_k+c_{l_k}=0 \tag{3.15}$$

---

[1] For computation of the *rms* value of the inductive current, it does not matter what the flux phase is, owing to the fact that the voltage (or flux) is assumed to be sinusoidal and the $\lambda-i_l$ curve symmetric with respect to the origin. Here, for computing purposes only, it is assumed $\lambda_k(\theta)=\lambda_k\sin\theta$. This has the advantage that the limits of integration in equation (3.14) are the same as those in equation (3.5). The same procedure applied in Figure 3.3 for the computation of the $\nu-i_r$ curve can then be used for the $\lambda-i_l$ curve computation.

with constants a_{l_k}, b_{l_k} and c_{l_k} known, and $\Gamma_k = 1/L_k$ to be computed. It can be shown that $a_{l_k} > 0$, $b_{l_k} > 0$ and $c_{l_k} < 0$. Since Γ_k must be positive, then

$$\Gamma_k = \frac{-b_{l_k} + \sqrt{b_{l_k}^2 - 4a_{l_k}c_{l_k}}}{2a_{l_k}} . \tag{3.16}$$

The peak current I_{l_k} is computed from

$$i_{l_k} = i_{l_{k-1}} + \Gamma_k(\lambda_k - \lambda_{k-1}) .$$

In this fashion, the peak values of the inductive current are computed directly for every segment in the $\lambda - i_l$ curve.

3.3 Comparisons Between Experiments and Simulations

Laboratory experiments were performed with a silicon iron steel core assembled in an Epstein frame [33]. No-load losses and *rms* current at 60 Hz, were measured for different voltage levels (Table 3.1). For comparison purposes, the initial magnetization curve [50] for the core material, was measured as well (Appendix B). The computed $v - i_r$ and $\lambda - i_l$ points (including core losses) are shown in Table 3.2. The measured and the calculated points (connected by straight line segments), with and without including the core losses, are shown in Figure 3.4.[2] The computed $v - i_r$ points connected by straight line segments (the first two columns of Table 3.2) is shown in Figure 3.5.

It can be seen that the computed $\lambda - i_l$ curve is closer to the measured one if we consider the core losses. The $v - i_r$ curve (Figure 3.5) is nonlinear and this may be important when modelling transformers and reactors for transients or harmonic studies.

---

[2] Sometimes, due to measurement errors, V_{rms} - I_{rms} and no-load loss curves may be crooked and need to be smoothed. The developed algorithm checks the presence of "noise" and, if it exists, a low pass Fourier filter is used to remove the "noise" from the input data.

Table 3.1: Laboratory measurements

$_{rms}(V)$	$I_{rms}(A)$	Losses(W)
0.0000	0.0000	0.0000
3.2040	0.0468	0.0727
6.7090	0.0656	0.2628
8.8880	0.0797	0.4223
11.8680	0.0953	0.6909
14.4960	0.1141	0.9723
16.2550	0.1281	1.1850
18.6160	0.1531	1.5090
20.9280	0.1875	1.8830
23.7840	0.2641	2.4620
25.2110	0.3265	2.8370
28.1780	0.5406	4.0100

Table 3.2: Computed $v-i_r$ and $\lambda-i_l$ curves

$v(V)$	$i_r(A)$	$\lambda(V.s)$	$i_l(A)$
0.0000	0.0000	0.0000	0.0000
4.5311	0.0321	0.0120	0.0579
9.4880	0.0524	0.0252	0.0599
12.5695	0.0630	0.0333	0.0858
16.7839	0.0776	0.0445	0.0950
20.5004	0.0894	0.0544	0.1313
22.9880	0.0974	0.0610	0.1514
26.3270	0.1098	0.0698	0.1997
29.5967	0.1240	0.0785	0.2674
33.6357	0.1484	0.0892	0.4349
35.6537	0.1684	0.0946	0.5819
39.8497	0.2371	0.1057	1.0251

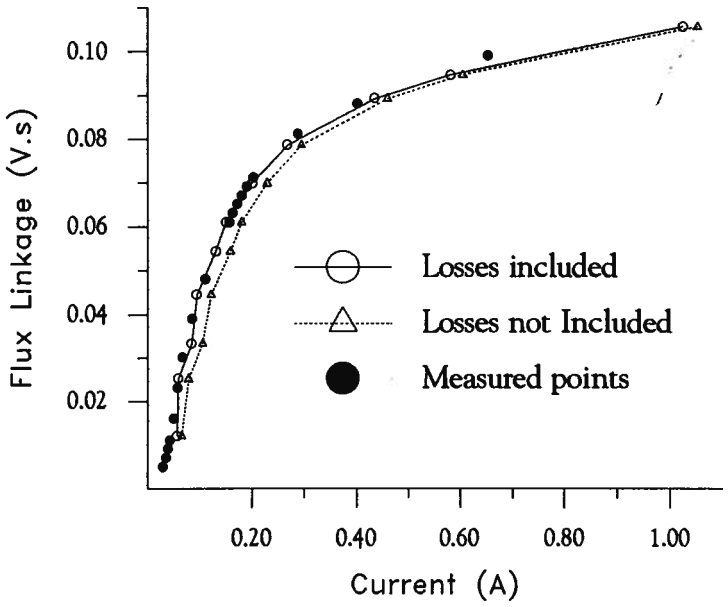

Figure 3.4: $\lambda - i_l$ curve.

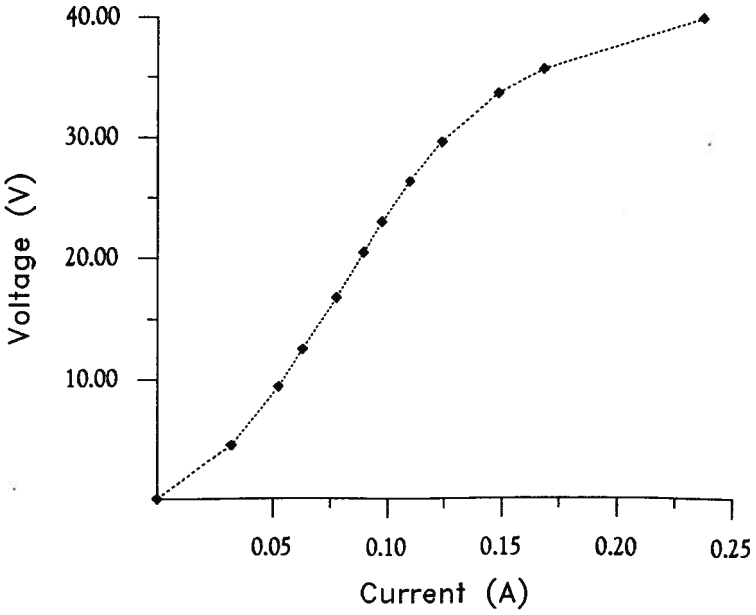

Figure 3.5: Computed $v - i_r$ curve.

3.4 Ferroresonance Simulations and Field Test

The BPA System of Section 2.4.1 is simulated again, Now, the transformer excitation branch is represented by a nonlinear resistance (curve represented by three piecewise-linear segments in Figure 3.6) in parallel with a nonlinear inductance (Figure 3.7) produced by the described algorithm, from the transformer manufacturer data. A straight line segment, with a slope of 4 times the short circuit inductance was connnected to the last segment of Figure 3.7 to represent the air core inductance. The voltage waveforms at the transformer terminal at phase A line side, are shown in Figure 3.8. The simulations were made assuming the excitation resistance to be constant (R_C=4.2MΩ - see dotted curve) and assuming a nonlinear resistance represented by Figure 3.6 obtained from the algorithm developed in this chapter (thin solid line). Simulations come closer to the field test (thicker solid line) if the nonlinear losses are taken into account. [3]

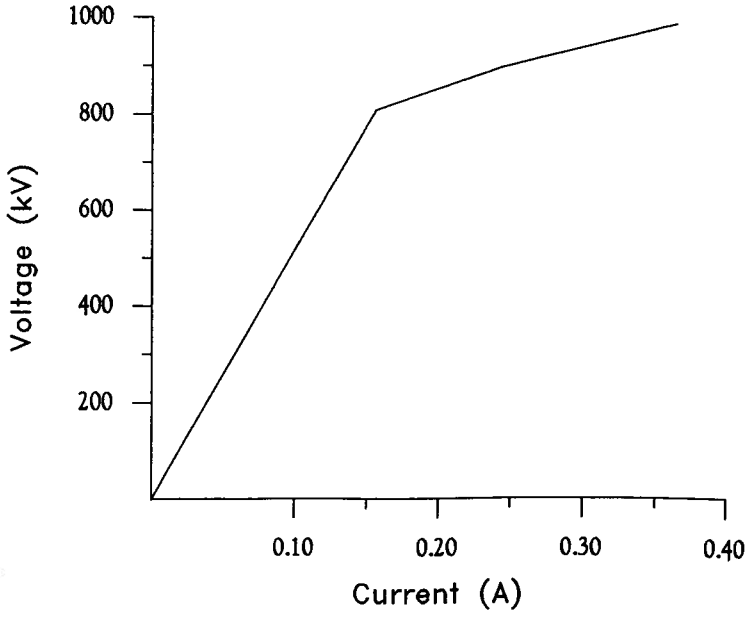

Figure 3.6: Nonlinear resistance.

[3] The field test curve was obtained using a digitizer to copy the data points from an oscilograph plot. Simulations were also made using a transformer air core inductance of 3 times the short circuit inductance, but the agreement with the field test was not so good.

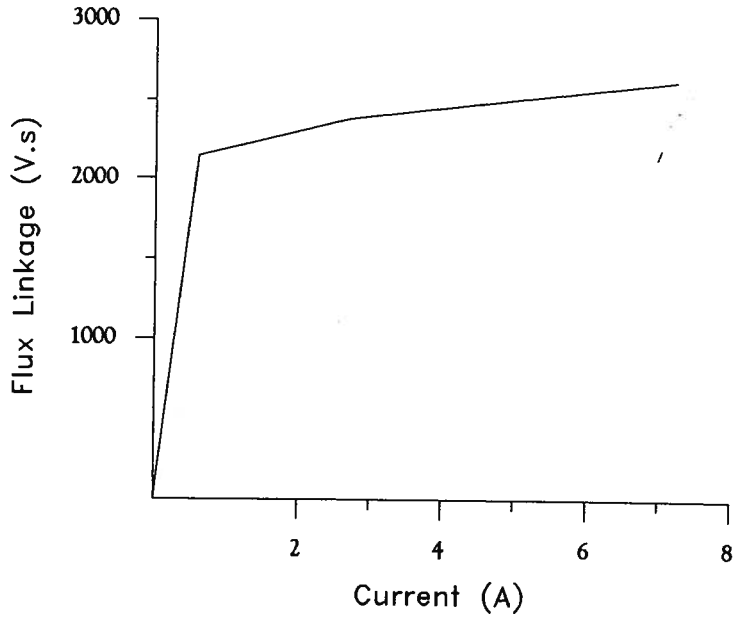

Figure 3.7 : Nonlinear inductance

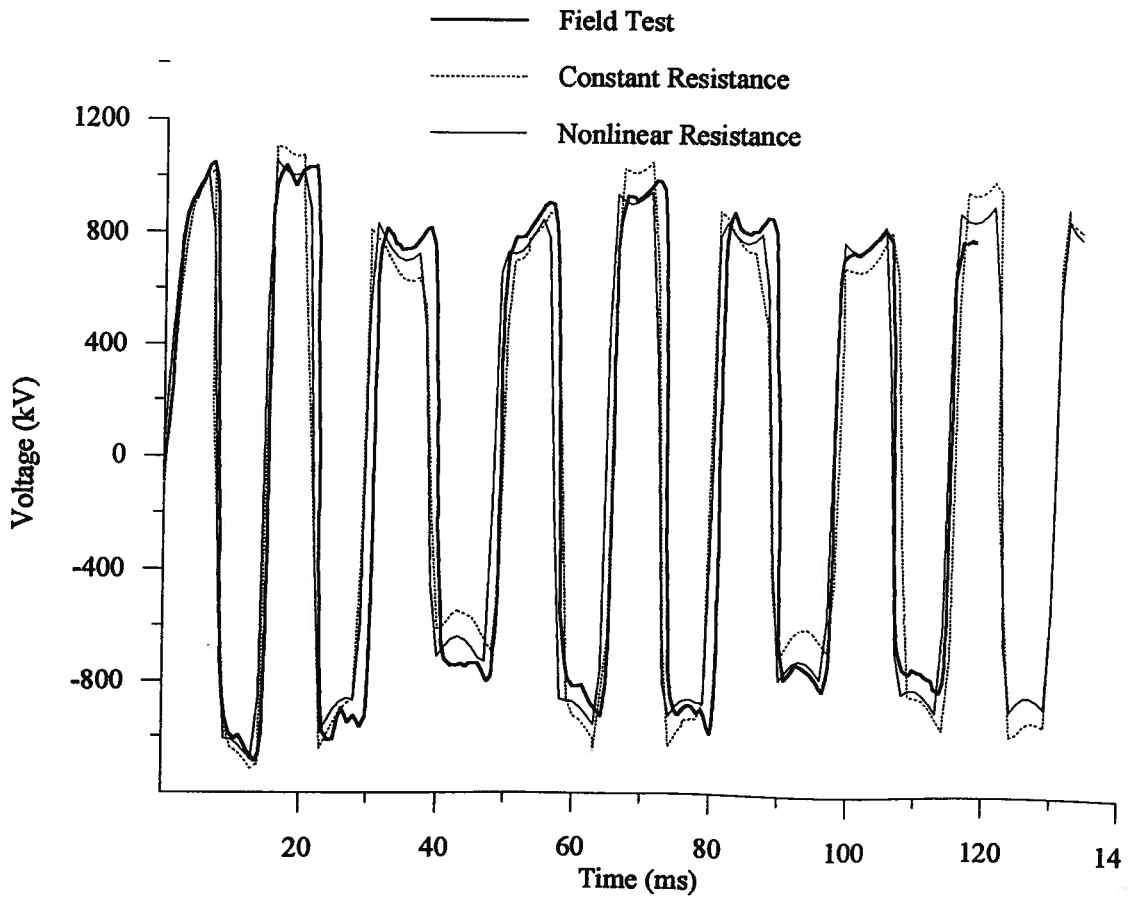

Figure 3.8 : Ferroresonance in a power system.

3.5 Distribution Transformer Saturation Curves

In Figure 3.9, one can see the nonlinear inductances curves ($\lambda - i_l$ curves) for 3 distribution transformers (50 kVA each), from different manufacturers, computed with the developed algorithm from tests performed at the low voltage terminals (120 V). The no-load losses were measured as well. The nonlinear resistance curves are shown in Figure 3.10. Transformer A has higher inductance in the unsaturated region and saturates at higher flux level, also it has the lowest no-load losses.

The $_{rms} - I_{rms}$ curve for a brand new distribution transformer is shown in Figure 3.11. The excitation *rms* current is not monotonic and drops as the voltage increases up to the vicinity of the rated voltage. In the unsaturated region, the transformer core has such a high permeability that current through stray capacitances tend to cancel out the magnetizing current.

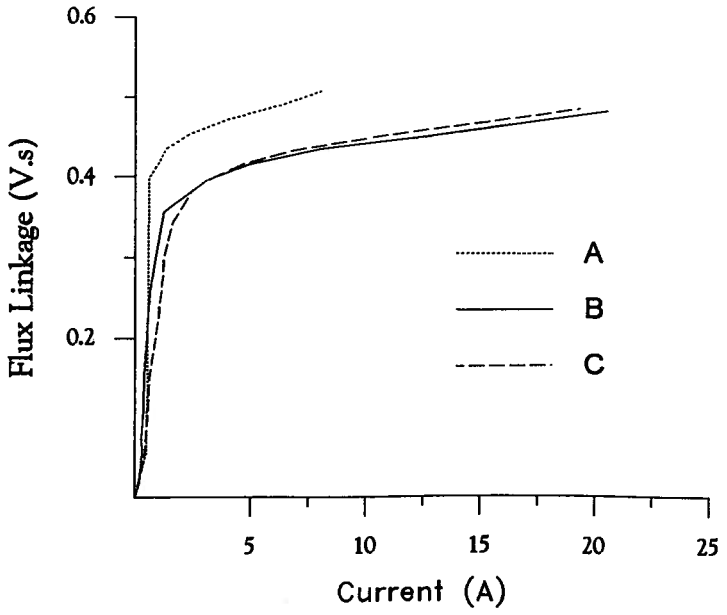

Figure 3.9: Nonlinear core inductances.

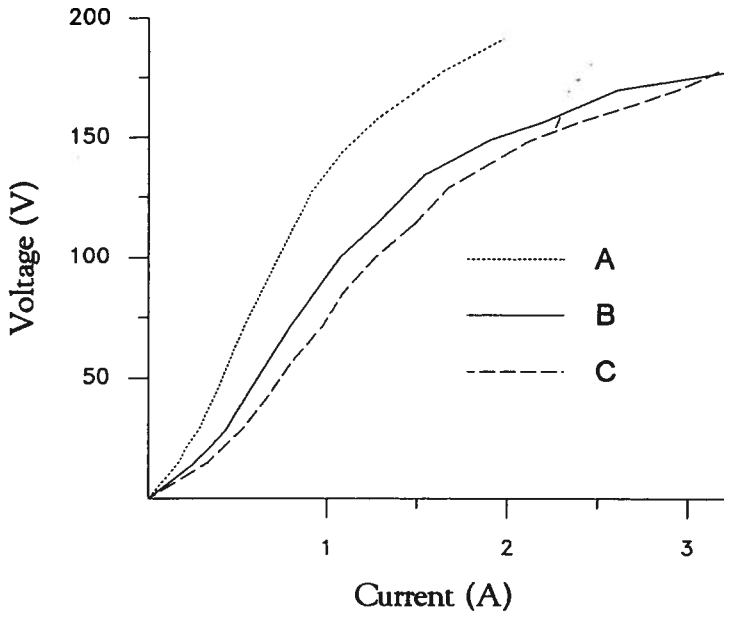

Figure 3.10: Nonlinear resistances.

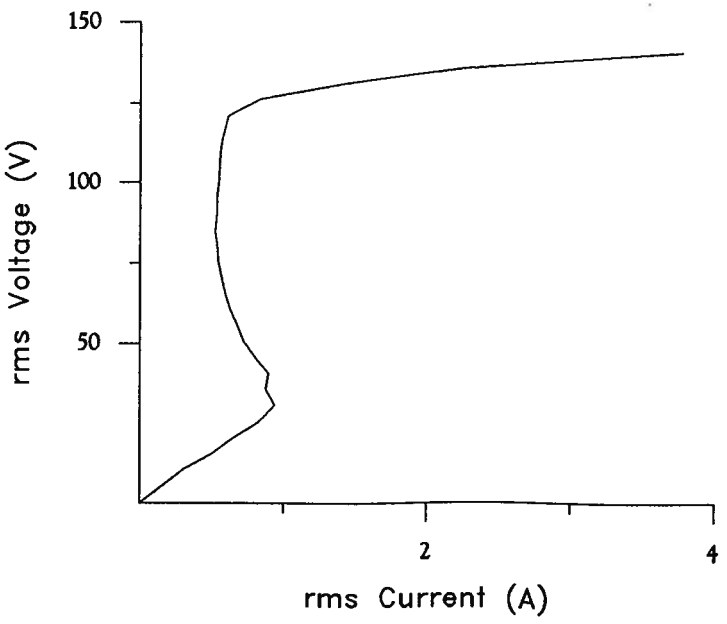

Figure 3.11: Newly manufactured transformer $_{rms} - I_{rms}$ curve.

The developed algorithm will not work for this case, unless stray capacitances are known. The algorithm is modified by inserting $-\omega C V_k \sin\theta$, where C is the open circuit capacitance, in between each parenthesis of equation (3.14). Then,

$$I^2_{l-rms_k} = \frac{2}{\pi}\left[\int_0^{\theta_1}\left(\frac{\lambda_k \sin\theta}{L_1} - \omega\, CV_k \sin\theta\right)^2 d\theta + \int_{\theta_1}^{\theta_2}\left(I_{l_1} + \frac{\lambda_k \sin\theta - \lambda_1}{L_2} - \omega\, CV_k \sin\theta\right)^2 d\theta + \ldots + \int_{\theta_{k-1}}^{\frac{\pi}{2}}\left(I_{l_{k-1}} + \frac{\lambda_k \sin\theta - \lambda_{k-1}}{L_k} - \omega\, CV_k \sin\theta\right)^2 d\theta\right]. \quad (3.17)$$

Equation 3.17 is rewritten in the form of 3.15, and the inductance L_k computed for each segment k. In Chapter 6, a crude method of estimating the capacitance C is briefly described.

3.6 Summary

A direct method for the computation of iron core saturation curve $(\lambda - i_l)$ has been presented. It is based on the transformer test data. It is a modification of previous methods, with core losses taken into account. Besides the $\lambda - i_l$ curve, it produces a nonlinear $v - i_r$ curve as well. Comparisons between laboratory measurements and simulations were made. It was shown that more accurate $\lambda - i_l$ curves can be obtained if losses are included.

Ferroresonance simulations were carried out. Simulations come closer to field tests if the nonlinear $v - i_r$ curve is taken into account.

The $\lambda - i_l$ and $v - i_r$ curves can be used for modelling transformers and iron core reactors in electromagnetic transients and harmonic loadflow programs.

Chapter 4

Saturation Curves of Delta-Connected Transformers from Measurements

4.1 Introduction

In the algorithm presented in last chapter (Section 3.2), we assumed all odd harmonic current components to be present in the measured values. For three-phase transformers, the standard excitation test data available are the positive sequence *Vrms* - *Irms* curves, and no-load losses. In Figure 4.1, we show a symmetrical three-phase voltage source supplying a no-load delta-connected transformer. The delta branches consist of nonlinear elements. In general, excitation tests are carried out with a closed delta [52]. In that case, ammeters, placed in series with the line, will not "detect" the triplen harmonic currents, because these circulate in the delta connection. In the next sections, we develop a method for generating the piecewise linear saturation curves (nonlinear resistance and nonlinear inductance), which accounts for the fact that triplen harmonics circulate in the closed delta, but do not appear in the measured line currents.

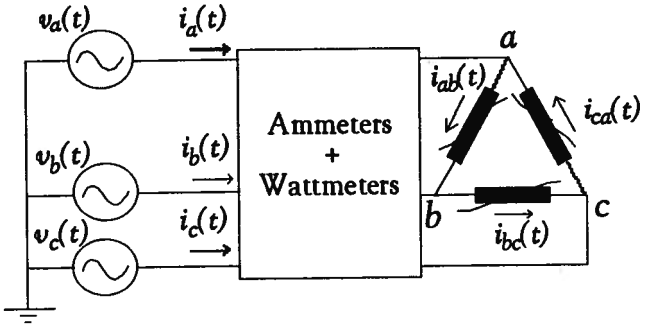

Figure 4.1: Delta-connected transformer
positive sequence excitation test.

4.2 Basic Considerations

In the circuit of Figure 4.1, the three branch elements of the delta connection are assumed to be nonlinear and identical. The branch currents can be written as a Fourier time series containing odd harmonic components only. Then:

$$\begin{aligned} i_{ab}(t) &= I_1 \sin(\omega t) + I_3 \sin(3\omega t) + \cdots + I_p \sin(p\omega t) + \cdots \\ i_{bc}(t) &= I_1 \sin(\omega t - 120^0) + I_3 \sin(3(\omega t - 120^0)) + \cdots + I_p \sin(p(\omega t - 120^0)) + \cdots \\ i_{ca}(t) &= I_1 \sin(\omega t + 120^0) + I_3 \sin(3(\omega t + 120^0)) + \cdots + I_p \sin(p(\omega t + 120^0)) + \cdots, \end{aligned} \tag{4.1}$$

where p is odd.

The triplen harmonic currents ($I_3, I_9, \ldots$) are in phase (zero sequence harmonics). The *rms* current in each branch is

$$I_{\Delta-rms} = \sqrt{\frac{I_1^2 + I_3^2 + \cdots + I_p^2 + \cdots}{2}}. \tag{4.2}$$

The line currents are:

$$\begin{aligned} i_a(t) &= i_{ab}(t) - i_{ca}(t) \\ i_b(t) &= i_{bc}(t) - i_{ab}(t) \\ i_c(t) &= i_{ca}(t) - i_{bc}(t) \,. \end{aligned} \tag{4.3}$$

Substituting (4.1) into (4.3) gives:

$$\begin{aligned} i_a(t) &= \sqrt{3}I_1 \sin(\omega t - 30^0) + \sqrt{3}I_5 \sin(5\omega t + 30^0) + \cdots \\ i_b(t) &= \sqrt{3}I_1 \sin(\omega t - 150^0) + \sqrt{3}I_5 \sin(5\omega t + 150^0) + \cdots \\ i_c(t) &= \sqrt{3}I_1 \sin(\omega t + 90^0) + \sqrt{3}I_5 \sin(5\omega t - 90^0) + \cdots \end{aligned} \tag{4.4}$$

Ammeters, placed into the supply line (outside the delta) read the *rms* current,

$$I_{rms} = \sqrt{3}\sqrt{\frac{I_1^2 + I_5^2 + \cdots + I_p^2 + \cdots}{2}} \,. \tag{4.5}$$

From equations (4.1) to (4.5) one can make the following observations:

- triplen harmonic currents, although present in each branch, are not present in the line currents.
- if triplen harmonic currents in each delta branch are removed from the *rms* value (equation (4.2)) and scaled by $\sqrt{3}$, the *rms* line currents (equation (4.5)) are obtained. This is the basis of the algorithm developed next.

4.3 Saturation Curves

Each delta branch in Figure 4.1 is represented by a nonlinear inductance in parallel with a nonlinear resistance (Figure 4.2). Their nonlinear characteristics are computed with the same assumptions made in the previous chapter.[1]

[1] Branch currents in the delta will have a "Δ" subscript and line currents will have no subscript added. For example, $i_{r\Delta}$ and i_r are the resistive components of the current in the delta branch and in the line, respectively.

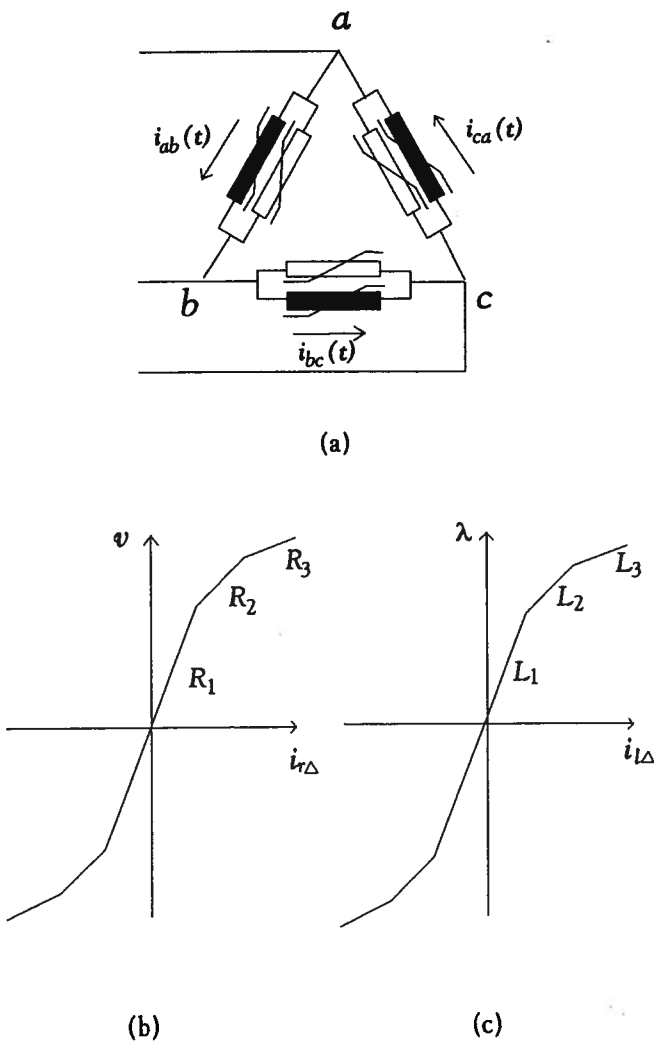

Figure 4.2: Core representation:
a) Nonlinear elements;
b) $v-i_{r\Delta}$ curve;
c) $\lambda-i_{l\Delta}$ curve.

The algorithm works as follows:

1. For the construction of the $v-i_{r\Delta}$ curve (Section 4.3.1):
   - compute the peak values of the branch current $i_{r\Delta_1}$, $i_{r\Delta_2}$,... point by point from the no-load losses.
2. For the construction of the $\lambda-i_l$ curve (Section 4.3.2):
   - from the $v-i_{r\Delta}$ curve, compute the *rms* values $I_{r\Delta-rms}$, remove the triplen harmonic currents and obtain the resistive line current I_{r-rms};
   - obtain the *rms* values I_{l-rms} of the line current due to the nonlinear inductance from I_{r-rms}, the total line current I_{t-rms}, and the applied voltage v;
   - compute the peak values of the inductive current $i_{r\Delta_1}$, $i_{r\Delta_2}$, ... point by point iteratively.

4.3.1 Computation of the v - ir_Δ curve

Similarly to the previous chapter, let us assume that the three-phase no-load losses P_1, P_2, ..., P_m are available as a function of the branch voltages $_{rms_1}$, V_{rms_2}, ..., V_{rms_m} (Figure 4.3).

If we assume that the applied voltage is sinusoidal, the conversion of *rms* voltages to peak values (vertical axis of Figure 4.2b) is simply

$$_k = V_{rms_k}\sqrt{2} \tag{4.6}$$

for $k = 1, 2, \ldots, m$.

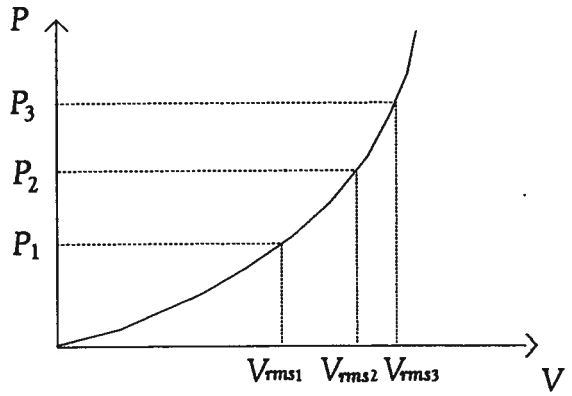

Figure 4.3: $_{rms}$- power loss curve.

Due to symmetry reasons, voltage and current waveforms need only be evaluated over 1/4 of a cycle. For a sinusoidal voltage $v(\theta)=V_k \sin\theta$, the three-phase active power P_k can be written in the form[2] :

$$P_k=3\left(\frac{2}{\pi}\int_0^{\frac{\pi}{2}} v(\theta)i_{r\Delta}(\theta)d\theta\right). \tag{4.7}$$

For the first linear segment in the $v-i_{r\Delta}$ curve, the current is sinusoidal. The computation of the first peak current $i_{r\Delta 1}$ is therefore straightforward. Since $P_1=3V_{rms_1}I_{rms_1}$ in the linear case,

$$i_{r\Delta 1}=\frac{2P_1}{3V_1}. \tag{4.8}$$

From the second segment onwards ($k\geq 2$), equation (4.7) is evaluated at each segment k, with only $i_{r\Delta_k}$ being unknown, as explained in more detail in Section 3.2.1 of the previous chapter. The computation of the peak current $i_{r\Delta_k}$ is done segment by segment,

[2] If the voltages have no harmonics, the active power P_k is produced only by the fundamental component of the current. This component is present in each branch as well as in each line. So, it does not matter if the wattmeters are connected in series with the line or with each delta branch. The three-phase power readings would be the same in both cases.

starting with $i_{r\Delta_2}$ and ending with the last point $i_{r\Delta_m}$. Whenever a point $i_{r\Delta_k}$ is found, its *rms* value is calculated as well. A Fourier program (see Appendix C for the algorithm) is used to compute the triplen harmonics (I_3, I_9, ...). They are then removed from $I_{r\Delta-rms}$ to obtain I_{r-rms}, which is needed later for the construction of the $\lambda - i_{l\Delta}$ curve.

4.3.2 Computation of the λ - $i_{l\Delta}$ curve

The conversion of the peak branch voltages $_k$ to flux λ_k, is again a re-scaling procedure. Hence, for each linear segment in the $\lambda - i_{l\Delta}$ curve,

$$\lambda_k = \frac{V_k}{\omega} \quad . \tag{4.9}$$

Let us now compute the peak values of the currents $i_{l\Delta_k}$ through the nonlinear inductance. First, the *rms* values of the line currents i_{l-rms} are evaluated with

$$I_{l-rms} = \sqrt{(I_{t-rms})^2 - (I_{r-rms})^2}, \tag{4.10}$$

where the line current I_{t-rms} is available from the measurements, and where I_{r-rms} has already been computed from the previous section.

For the first linear segment, the computation of $i_{l\Delta_1}$ is straightforward since there are no harmonics yet. Therefore,

$$i_{l\Delta_1} = \frac{\sqrt{2} I_{l-rms_1}}{\sqrt{3}}.$$

From the second segment onwards ($k \geq 2$), the algorithm works iteratively as follows (see $\lambda - i_{l\Delta}$ curve in Figure 4.4):

1. guess i_g;
2. with $\lambda(\theta) = \lambda_k \sin\theta$, find 1/4 of a cycle of the distorted current analytically;

3. compute the *rms* inductive branch current whose peak is i_g ;

4. use a Fourier program to find the triplen harmonic inductive currents in the delta branch (Appendix C);

5. remove the triplen harmonics from the estimated *rms* branch current. Scale the estimated result I_{lest} by $\sqrt{3}$ and compare it to $I_{l\text{-}rms}$ in equation (4.10);

6. if the absolute value of the difference $i_d = I_{l\text{-}rms} - I_{lest}$ is less than the specified tolerance, convergence is achieved. Otherwise, the residue i_d is added to i_g and the iterative process is repeated from step 2 onwards.

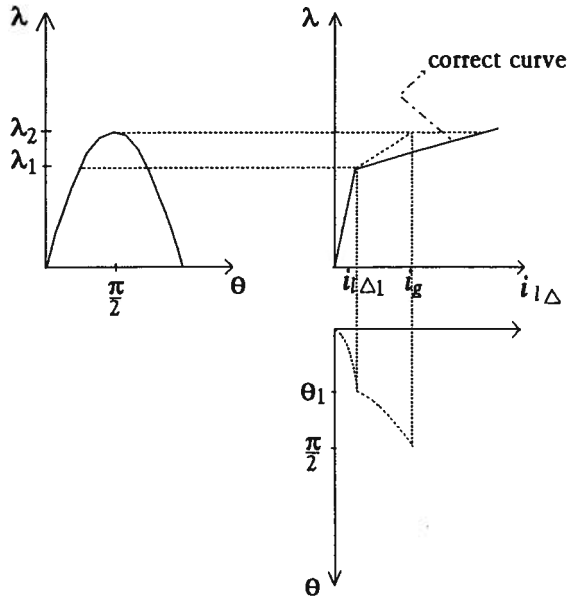

Figure 4.4: Generating current wavefor from sinusoidal flux.

In general, convergence is achieved in less than 20 iteration steps with a tolerance of $10^{-5}\, i_{l\Delta_1}$ and initial guess

$$i_g = i_{l\Delta_{k-1}} + \frac{\sqrt{2}(I_{l-rms_k} - I_{l-rms_{k-1}})}{\sqrt{3}},$$

for every $k \geq 2$. In some cases more than 20 iteration steps may be necessary.

4.4 Case Study

Consider a 50 Hz three-phase five-legged core type transformer. The following information is known [53]:

1. rated power - 750 MVA (three-phase);

2. rated voltages - 420 kV/ 27 kV (line to line values);

3. wye connection on 420 kV side, delta connection on 27 kV side.

The positive sequence excitation test data, from the closed delta 27 kV side, are shown in Table 4.1.

V_{rms} is the *rms* line to line excitation voltage, $I_{t\text{-}rms}$ is the *rms* excitation current (three-phase average) and P are the no-load losses (three-phase values).

Table 4.1: Three-phase transformer test data

V_{rms} (kV)	I_{t-rms} (A)	P (kW)
22.76	8.20	206.21
24.29	11.35	240.26
25.64	15.50	270.13
27.00	21.16	311.00
27.50	24.68	323.03
28.47	31.63	355.48
29.10	38.30	385.41
32.50	80.97	560.00

The two computed λ - $i_{l\Delta}$ curves (points connected by straight line segments) are shown in Figure 4.5. One of them assumes that all odd harmonic components of the current are present in the measured values, and is therefore incorrect. The other curve is the correct one; it has been produced with the algorithm of Section 4.3.2.

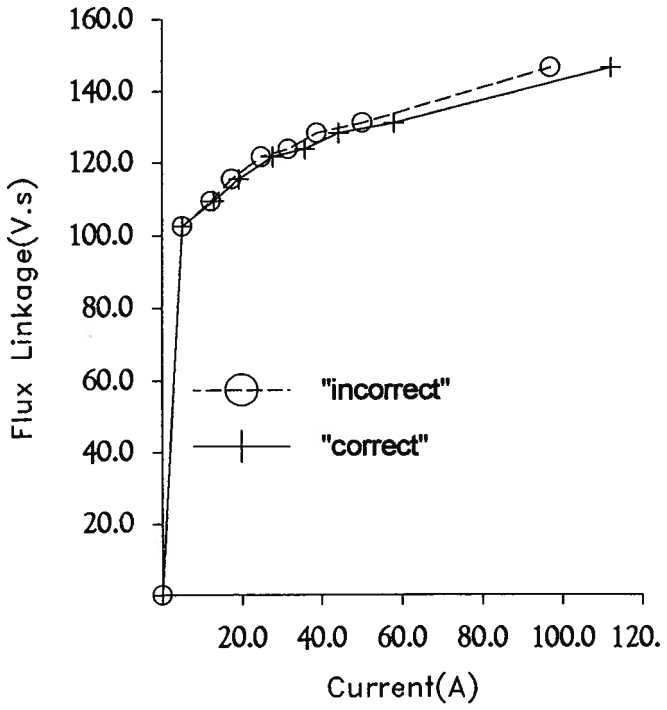

Figure 4.5: $\lambda - i_{l\Delta}$ curve.

It can be seen that the correct curve goes deeper into saturation. For the highest flux value, there is a difference of approximately 14% between the peak currents of the incorrect curve and the correct one. The piecewise linear ν - $i_{r\Delta}$ curve is shown in Figure 4.6.

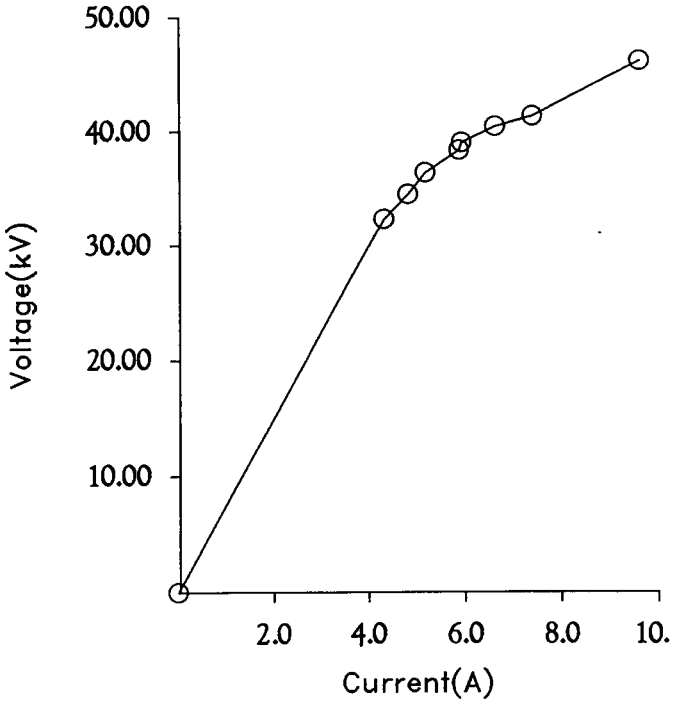

Figure 4.6: $v - i_{r\Delta}$ curve.

In the iteration scheme of Section 4.3.2, harmonics up to the 99th order were included, which is more than needed in practice. An average of 23.86 iteration steps was necessary (the maximum number of iterations was 34). In order to check the numerical accuracy of the method, the *rms* line currents were recomputed back from v - $i_{r\Delta}$ and λ - $i_{l\Delta}$ curves. Numerical errors were found to be very small (less than 0.001%).

4.5 Summary

An approach to the computation of instantaneous saturation curves of delta-connected transformers has been presented. It uses positive sequence excitation test data as input, and is suitable for situations in which the tests are performed with a closed delta.

For the case study presented in Section 4.4, it was shown that a difference of approximately 14% between the peak currents of the incorrect curve and the correct one occurred. The last flux linkage point is around 1.2 p.u. In fact, for transient studies, it is

often necessary to know peak flux-peak current curves beyond that point. The usual way is to extend the curve up to a value necessary for the study (this extension is sometimes done with a straight line passing through the previous to the last and the last point in the peak flux-peak current curve). This may lead to larger errors for the peak values of the current. The curves diverge as the flux goes up towards deep saturation. The transformer magnetizing current would always be underestimated if triplen harmonics inside the delta windings were not taken into account. Errors can also affect the air core reactance value. A parametric study was done considering typical air core reactances from 0.2 p.u. to 0.5 p.u., connected to the last point of the correct curve of Figure 4.5. Errors on the slope of the saturation characteristics, for this case, are between 18% and 25%, when the magnetizing curve reaches the transformer rated current. These differences may be important in ferroresonance or inrush current studies

For the development of the algorithm in this chapter, it was assumed that each phase behaves independently. This is valid when the transformer is saturated only. The current in the saturated phase is much larger than the current in the remaining phases. The saturated phase can be considered "decoupled" from the other phases.

Chapter 5

Hysteresis and Eddy Current Losses in Iron Core

5.1 Introduction

In this chapter, a general discussion of hysteresis and eddy losses in iron core is presented. RL networks, in which the inductances are nonlinear and the resistances are linear, are developed to model the nonlinear and frequency-dependent effects of the transformer core (saturation, eddy currents and hysteresis). It is assumed that the core loss is known as a function of frequency. Simulations are compared to laboratory measurement of inrush current and to a ferroresonance field test.

5.2 Frequency-Dependent Core Models

Rosales and Alvarado[18] represented eddy current effects in the core by solving Maxwell's equations within the laminations assuming that the permeability and conductivity of the material were constant. They derived expressions for the lamination impedance $Z_l(j\omega)$ and admittance $Y_l(j\omega)$ in the forms:

$$Z_l(j\omega) = R_l \xi \tanh(\xi), \tag{5.1}$$

and

$$Y_l(j\omega) = (1 / R_l\xi)\coth(\xi) \tag{5.2}$$

where

$$R_l = \frac{2w}{\sigma l d} \qquad \xi = d\sqrt{j\omega\mu\sigma}$$

and

l = lamination length;

w = lamination width;

$2d$ = lamination thickness;

μ = magnetic permeability of the material;

σ = electric conductivity of the material.

From the expansion of the hyperbolic tangent in (5.1) into partial fractions

$$\tanh\xi = 2\xi\sum_{k=1}^{\infty}\frac{1}{\xi^2 + [\pi(2k-1)/2]^2}, \tag{5.3}$$

they realized a series Foster-like linear circuit and from the expansion of the hyperbolic cotangent, they realized the parallel Foster-like circuit of Figure 5.1. The accuracy of the representation depends on the number of terms retained in the partial fraction expansion.

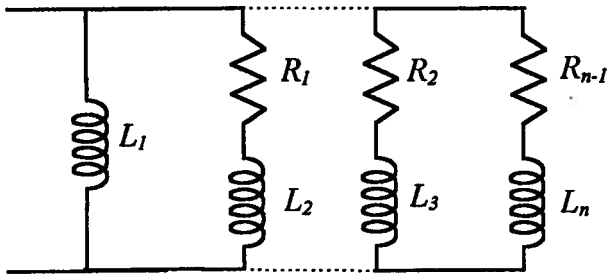

Figure 5.1: Eddy Current representation of the core after [18]

Tarasiewicz et al.[17] used (5.1) and expanded the hyperbolic tangent in continued fraction form,

$$\tanh \xi = \cfrac{\xi}{1+\cfrac{\xi^2}{3+\cfrac{\xi^2}{5+\cfrac{\xi^2}{7+\cfrac{\xi^2}{9+\cdots}}}}}, \tag{5.4}$$

and realized the ladder network of Figure 5.2, known as the standard Cauer circuit.

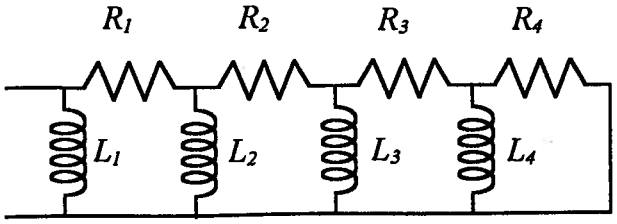

Figure 5.2: Eddy Current representation of the core after [17]

They observed that the number of terms to be retained in the continued fraction of (5.4) is smaller than the number of terms to be retained in the partial fraction of (5.3) for the same frequency range and verified that the four sections of the continued fraction model of Figure

5.2 would be enough to reproduce the exact impedance of (5.1) for a frequency range up to 200kHz with an error less than 5%. They also noticed that to achieve the same accuracy, 72 sections of the Foster-like circuit of Figure 5.1 would be required. Based on that, they decided to work with the standard Cauer circuit. However, it seems the authors were not aware that once the circuit parameters of Figure 5.2 are known, a Foster-like equivalent circuit which reproduces the same frequency response with exactly the same number of elements can be realized as well (later on in this chapter, network realizations will be addressed)[61]. Therefore, it seems there is no apparent gain in choosing this ladder network to represent eddy current effects in the core.

De Leon and Semlyen[20] suggested the Cauer circuit of Figure 5.3. The RL parameters were obtained by a nonlinear fitting process to match (5.1). This circuit can be interpreted as a discretization of the lamination. The inductances represents the flux paths and the resistances produce the eddy loss. At DC excitation, the current flows through the magnetizing inductances lying longitudinally (in the previous circuits, the DC current flows through one inductance only). This could be interpreted as a uniform flux distribution in the entire lamination at DC level.

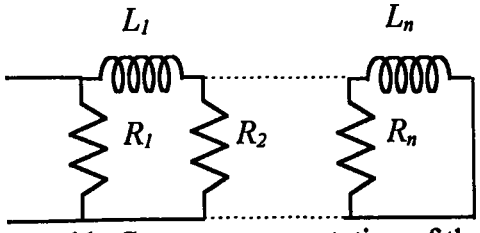

Figure 5.3 : Eddy Current representation of the core after [20]

5.3 Core Loss

In the algorithm developed in chapters 3 and 4, the excitation branches of transformers were represented by a nonlinear resistance in parallel with a nonlinear

inductance. Thus, hysteresis and eddy current loss were assumed to have the same frequency-dependence. It is clear that the circuit would not reproduce the core loss for frequencies different from the rated frequency.

A more detailed core model should take into account the nonlinear and frequency-dependent effects of saturation, hysteresis and eddy currents. It should be emphasized that information about how eddy and hysteresis losses are split, is in fact artificial. Today, the point of view of many researchers is that virtually all the observed losses are resistive losses associated with micro eddy currents due to Barkhausen jumps of domain walls [64,65], no matter how slow the magnetization loops are traversed.

Core models in which hysteresis and eddy currents are treated simultaneously are developed in the next sections. A Foster-like circuit is used to represent both, hysteresis and eddy current effects. First, consideration is given to the core operating in the linear region. Nonlinear effects are considered later.

5.4 Eddy Current and Hysteresis Modelling

There is a property of linear passive networks in which the knowledge of the real part of an impedance Z(s) for $s=j\omega$ (Re ($Z(j\omega)$), completely determines Z(s) [66]. If (Re ($Z(j\omega)$) is a given rational function of frequency ω, then one can construct the corresponding rational function Z(s) in terms of the complex frequency variable s. Once Z(s) is known, it can be realized as a passive network [61,63,66]. The same process applies to the admittance function Y(s), as described next.

5.4.1 Construction of Y(s) from Its Real Part

The process of constructing Y(s) or Z(s) from their real parts is well known in network synthesis theory and only a brief discussion is presented here. For more details, the reader is referred to [61,66].

Consider first a simple circuit composed of only two linear RL elements connected in parallel (Figure 5.4a).

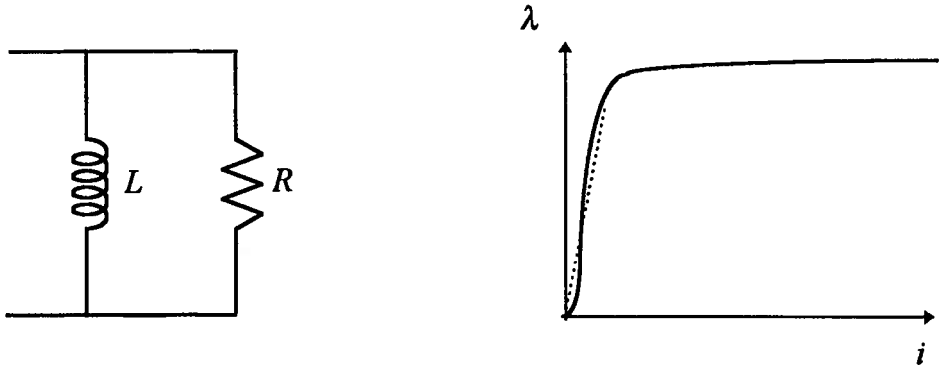

(a) (b)

Figure 5.4: Core parameters.

Its admittance Y(s) could be written in the form

$$Y(s) = \frac{1}{R} + \frac{1}{sL}.$$

It follows that

$$G = \frac{1}{R} = \frac{Y(s) + Y(-s)}{2}. \tag{5.5}$$

If the elements are frequency-dependent, $G(\omega) = 1/R(\omega) = \mathrm{Re}[Y(j\omega)]$, or with s=jω,

$$\mathrm{Re}[Y(s)] = \frac{Y(s) + Y(-s)}{2}. \tag{5.6}$$

Now, consider the exciting branch of a single-phase transformer to be linear (the extension of the method to include saturation effects will be done later). One can visualize the core operating below the knee of the saturation curve. In this region, the saturation curve could be approximated by a linear segment (dashed line of Figure 5.4b). The exciting branch can be represented by a frequency-dependent lossy element R(ω) in parallel with the magnetizing inductance L(ω). The relation which ties R(ω) to L(ω) is shown below.

First represent Y(s) as a rational function containing *n* pairs of poles and zeroes :

$$Y(s)=\frac{N(s)}{D(s)}=K_{\infty}\frac{(s+z_1)(s+z_2)\cdots(s+z_n)}{(s+p_1)(s+p_2)\cdots(s+p_n)}, \tag{5.7}$$

p_i and z_i are real and positive, i.e., the poles and zeroes of Y(s) lie on the left hand side of the s plane. From (5.6) and (5.7), the real part of Y(s) is expressed by:

$$\mathrm{Re}[Y(s)]=\frac{1}{2}\left[\frac{N(s)D(-s)+N(-s)D(s)}{D(s)D(-s)}\right]$$

or

$$\mathrm{Re}[Y(s)]=\frac{U(s^2)}{W(s^2)}=K_{\infty}\frac{(-s^2+u_1^2)(-s^2+u_2^2)\cdots(-s^2+u_n^2)}{(-s^2+p_1^2)(-s^2+p_2^2)\cdots(-s^2+p_n^2)}, \tag{5.8}$$

where u_i is also positive and real [62]. Expanding (5.8) into partial fractions

$$\mathrm{Re}[Y(s)]=K_{\infty}+\frac{K_1}{(-s^2+p_1^2)}+\frac{K_2}{(-s^2+p_2^2)}+\cdots+\frac{K_n}{(-s^2+p_n^2)}. \tag{5.9}$$

Further expanding each fraction of the equation above into two partial fractions

$$\mathrm{Re}[Y(s)]=K_{\infty}+\frac{K_1/2p_1}{(s+p_1)}+\frac{K_1/2p_1}{(-s+p_1)}+\cdots+\frac{K_n/2p_n}{(s+p_n)}+\frac{K_n/2p_n}{(-s+p_n)}$$

or

$$\mathrm{Re}[Y(s)]=\left(\frac{K_\infty}{2}+\frac{K_1/2p_1}{(s+p_1)}+\cdots+\frac{K_n/2p_n}{(s+p_n)}\right)+\cdots+\left(\frac{K_\infty}{2}+\frac{K_1/2p_1}{(-s+p_1)}+\cdots+\frac{K_n/2p_n}{(-s+p_n)}\right) \quad (5.10)$$

Comparing (5.6) and (5.10) it is clear that the admittance function is given by:

$$Y(s)=K_\infty+\frac{K_1/p_1}{(s+p_1)}+\frac{K_2/p_2}{(s+p_2)}+\cdots+\frac{K_n/p_n}{(s+p_n)} \quad (5.11)$$

From (5.11), one can also write the admittance Y(s) in the form:

$$Y(s)=\frac{a_n s^n+\cdots+a_2 s^2+a_1 s+a_0}{b_n s^n+\cdots+b_2 s^2+b_1 s+b_0} \quad (5.12)$$

It can be seen that if the function G(ω)=Re[$Y(j\omega)$] is known, Y(s) is determined.[1] It should be pointed out that G(ω) must be expressed as an even rational function in ω^2 with real coefficients in the form of (5.8) with $\omega^2=-s^2$ and $0\le G(\omega)<\infty$ for all frequencies [66]. A curve fitting procedure to obtain G(ω) or R(ω) in the required form, from one of the core loss - frequency curves supplied by steel lamination manufacturers, is explained in Appendix D. It is recommended that the data be taken for an induction level, at which the lamination is not saturated.

5.4.2 Linear Network Synthesis

From Y(s), any of the RL equivalent networks of Figure 5.5 can be realized with the same minimum number of elements. If for any of these circuit, the parameters are known, Y(s) or Z(s)=1/Y(s) could be determined and the remaining circuits could be realized as

[1] The construction of Y(s) from its real part in the partial fraction form of (5.11) was first suggested by Bode[58]. There is a method to compute the coefficients a_i and b_i in (5.12) directly from (5.8) due to C.M. Gerwetz [57]

well. It must be clear that all these circuits are equivalents only with respect to their terminals, i.e., the network elements of each circuit must have the proper values to produce the same terminal impedance or admittance as a function of the complex frequency s.

Let us describe the algebraic process for realizing the parallel Foster-like circuit. The terminal admittance of the RL network of Figure 5.5a is

$$Y(s)=\frac{1}{R_\infty}+\sum_{i=1}^{n}\frac{1/L_i}{s+R_i/L_i}. \tag{5.13}$$

This circuit could be realized directly from (5.11) with

$$R_\infty=\frac{1}{K_\infty},\quad L_i=\frac{p_i}{K_i}\quad \text{and}\quad R_i=\frac{p_i^2}{K_i}.$$

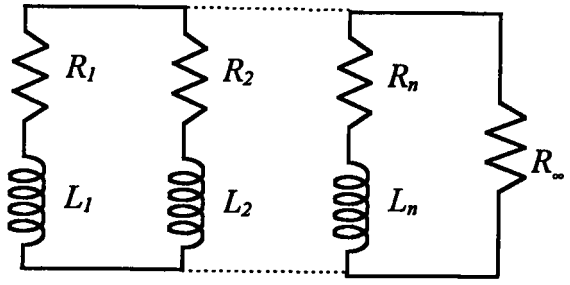

a) Parallel RL Foster-like network

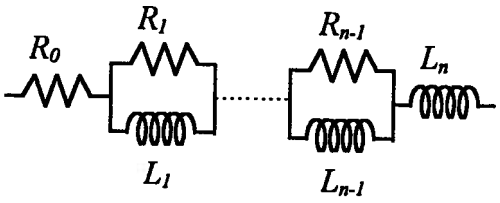

b) Series RL Foster-like network.

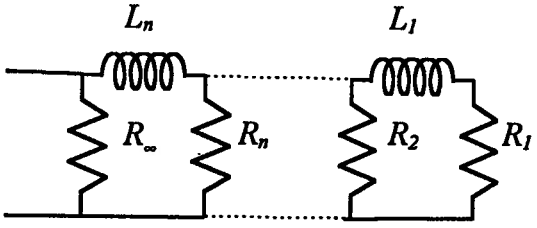

c) Physical Cauer network

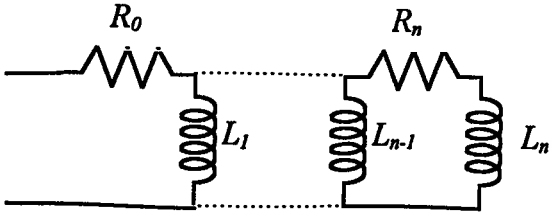

d) Standard Cauer network

Figure 5.5 : Realization of RL networks.

For the Cauer circuit of Figure 5.5c Y(s) is written in the continued fraction form:

$$Y(s)=\frac{1}{R_\infty}+\cfrac{1}{L_n s+\cfrac{1}{\cfrac{1}{R_n}+\cfrac{1}{L_{n-1}s+\cdots+\cfrac{1}{\cfrac{1}{R_2}+\cfrac{1}{L_1 s+R_1}}}}}} \tag{5.14}$$

Equation (5.14) could be derived from (5.12) according to the following steps:

a - from (5.12) Y(s) is split into two terms by removing the constant a_n/b_n;

$$Y(s)=\frac{a_n}{b_n}+\frac{a'_{n-1}s^{n-1}+\cdots+a'_2s^2+a'_1s+a'_0}{b_ns^n+\cdots+b_2s^2+b_1s+b_0} \tag{5.15}$$

or

$$Y(s)=\frac{a_n}{b_n}+\cfrac{1}{\cfrac{b_ns^n+\cdots+b_2s^2+b_1s+b_0}{a'_{n-1}s^{n-1}+\cdots+a'_2s^2+a'_1s+a'_0}}$$

b - removing $\frac{b_n}{a'_{n-1}}s$ from the denominator of the second term of the equation above, results

$$Y(s)=\frac{a_n}{b_n}+\cfrac{1}{\cfrac{b_ns}{a'_{n-1}}+\cfrac{1}{\left[\cfrac{a'_{n-1}s^{n-1}+\cdots+a'_2s^2+a'_1s+a'_0}{b'_{n-1}s^{n-1}+\cdots+b'_2s^2+b'_1s+b'_0}\right]}}. \tag{5.16}$$

Now, the process of long division is done for the term between the brackets (steps a and b are repeated). For each cycle, a constant (step a) and a pole at s=∞(step b) are removed. The process continues until the order of the polynomial in the last continued fraction is one. For the remaining circuit realizations of Figure 5.5, the reader is referred to [61].

A remark must be made about the calculation of Y(s). Consider the Foster-like circuit of Figure 5.5a with an inductance L_{dc} placed across its terminals (Figure 5.6). It is clear that L_{dc} does not affect the conductance G(ω); it affects only the susceptance. In the process described earlier, Y(s) is the minimum admittance function that produces G(ω). The full admittance is given by L_{dc} in parallel with Y(s).

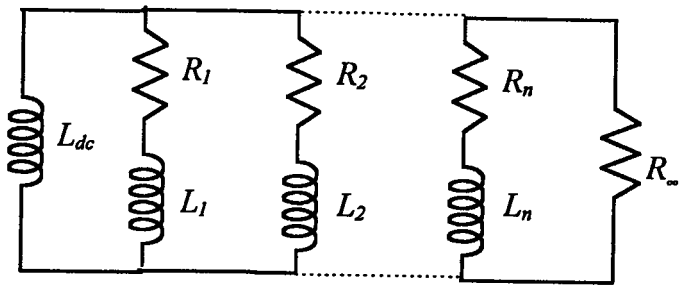

Figure 5.6: Frequency-dependent representation of the core.

5.4.3 *Iron Core Nonlinearities*

Since the resistances and inductances in the circuit of Figure 5.6 do not represent any physical part of the core, it is not clear how to incorporate nonlinear effects. Considering that low frequency elements contribute more to saturation than high frequency elements, only the inductance L_{dc} is made nonlinear. The Foster-like circuit was chosen because it has only two nodes, therefore, it is computationally more efficient than the remaining circuits of Figure 5.5.

5.4.4 *Numerical Example - Hysteresis*

It is appropriate to illustrate how the model works for an example in which a core is assumed to experience only hysteresis loss (this is an arbitrary case since hysteresis and eddy losses cannot be separated). Initially, suppose hysteresis could be reproduced by a resistance

in parallel with a nonlinear inductance. For a sinusoidal applied voltage, at rated frequency, the flux-current loop of Figure 5.7 is obtained. Let us keep the flux amplitude constant.[2] For any frequency, the area inside the flux-current loops should be the same and the loss is a function of how fast the trajectories are traversed. For a frequency equal to twice the rated frequency, the voltage doubles. So, hysteresis resistance would have to be twice the hysteresis resistance at rated frequency to produce the same loss per cycle. For any frequency, the resistance R_r should be replaced by an equivalent frequency-dependent resistance $R(\omega)$ according to:

$$R(\omega)=\frac{\omega}{\omega_r}R_r, \tag{5.17}$$

where ω_r is the rated angular frequency and R_r is the hysteresis resistance at rated frequency.

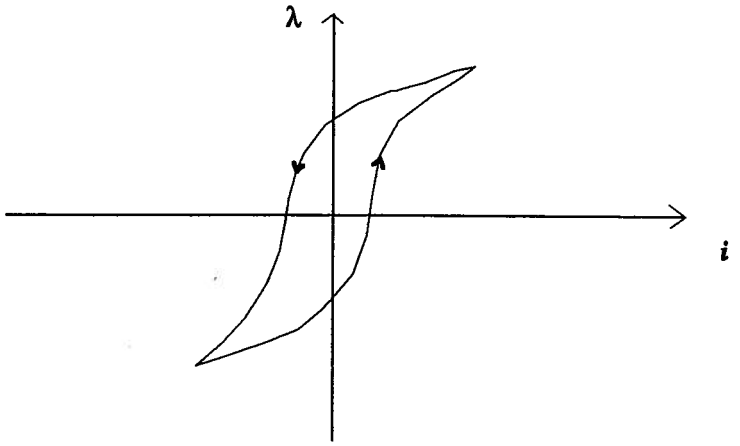

Figure 5.7 : $\lambda-i$ hysteresis curve.

Let us now represent the core by a two slope λ-i curve, defined by points in Table 5.1, and a resistance R_r=100 Ω at rated frequency (60Hz). Using the method described in the previous sections with $W_h>>W_{eddy}$ (Appendix D), the Foster-like circuit parameters of Figure

[2] This could be acomplished by keeping constant the ratio between the amplitude of the voltage signal and the frequency.

5.6 are found for a frequency range from 60 Hz to 3 kHz. The fitted frequency-dependent resistance and its value from (5.17) are shown in Figure 5.8.

Table 5.1 : Flux-current curve

Current (A)	Flux (V.s)
0.0000	0.0000
20.0000	0.4000
300.0000	0.6000

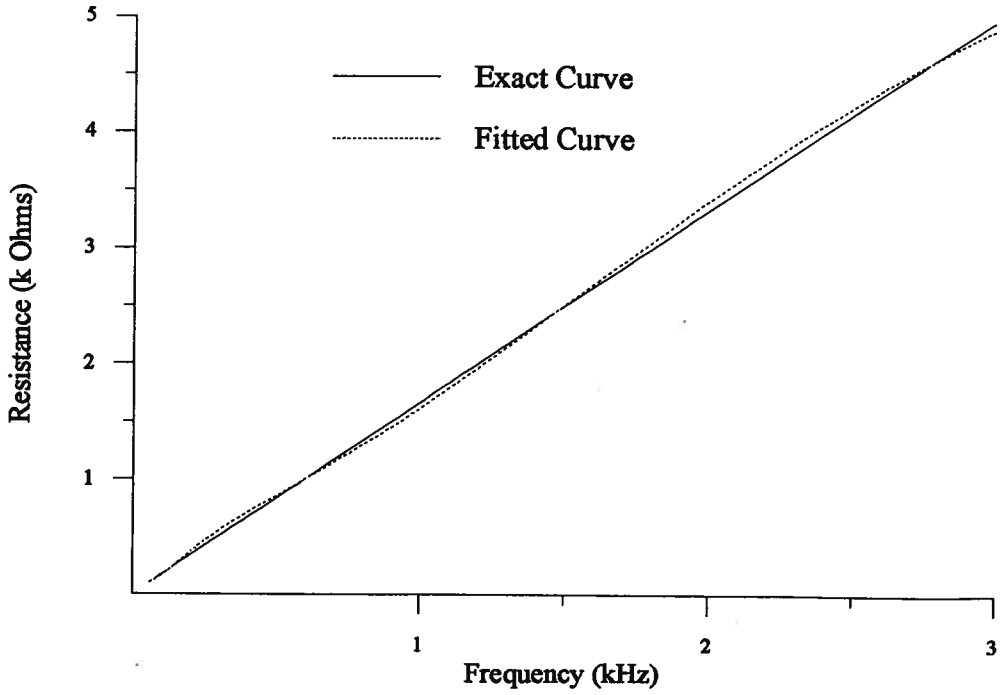

Figure 5.8: Frequency-dependent resistance.

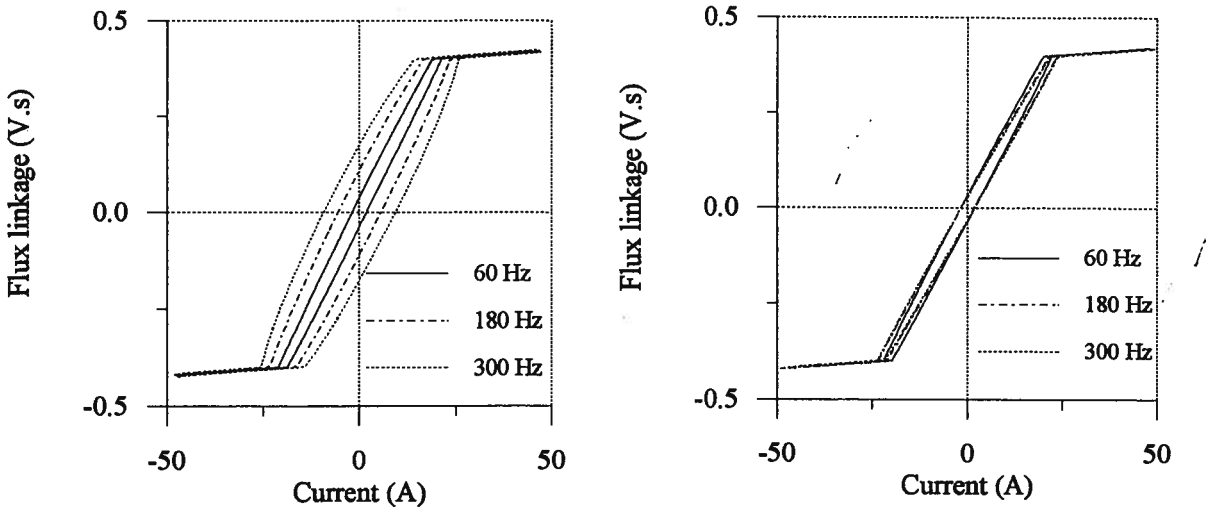

a) Constant resistance b) Frequency-dependent resistance

Figure 5.9: Flux-current loops.

The flux-current plots shown in Figure 5.9 were obtained from time-domain simulations using Microtran®[43]. Sinusoidal flux linkages of constant amplitudes and frequencies of 60 Hz, 180 Hz and 300 Hz, were used for the simulations. In Figure 5.9a, the loops were obtained considering the core loss represented by a constant resistance and, in Figure 5.9b, with the frequency-dependent model developed here. In Figure 5.9b, the area of the loops are nearly independent of the frequency, however, the flux-current loops tilt slightly clockwise as frequency increases. In a qualitative way, one could interpret that an increase of the core resistance is associated with a decrease in the core inductance caused by the flux being pushed away from the center of the lamination.

5.5 Inrush Current: Simulation and Measurements

A single-phase 60 Hz, 1 kVA , 208/104/120 V laboratory transformer, in which the core is made of non-oriented silicon steel laminations, was tested. From short-circuit tests, with the voltage source connected to the 104 V side:

1. AC resistance measured with the 120V side short-circuited - 0.60 Ω;

2. Leakage reactance with the 120 V side short circuited - 0.19 Ω;

3. DC winding resistance - 0.40 Ω.

The points (empty circles) of the flux-current characteristic of Figure 5.10 were obtained from no-load loss measurements and V_{rms}-I_{rms} values, using the method developed in Chapter 3. When the core is operating in the unsaturated region, its inductance can be roughly approximated by 2.4 H. The core loss at 60 Hz is represented by a constant resistance of 1.8 k Ω. All parameters are referred to the 104 V terminal.

The Foster-like circuit linear parameters shown in Table 5.2, was calculated for a frequency range from 60 Hz to 3 kHz assuming the ratio of hysteresis to eddy loss per cycle to be W_h/W_{eddy}=2 at 60 Hz [67] (it does not make any difference in the simulations if this ratio is taken as 1 or 3). The transformer was initially demagnetized and later, a voltage source was switched in the 104 V terminal. The voltage signal (Figure 5.11) was saved as an ASCII file and used as input in Microtran®. The inrush current waveform was measured as well. Plots of the simulated current using two core models (Foster-like circuit and a constant resistance in parallel with a nonlinear inductance) and the measured current using a time step of 50 μs, are shown in Figure 5.12. For the study, a straight line segment was connected to the last point of the curve of Figure 5.10. Its slope was chosen to match the first peak of the measured current, when the flux linkage reached its first peak (the flux waveform was obtained integrating the voltage waveform of Figure 5.11).[3]

---

[3] By extending the last segment of Figure 6.10, it was found that the first current peak in the simulations was underestimated by nearly 5%. The winding resistance, used for the simulations, was 0.45 Ω which is slightly above the measured value.

Table 5.2: Linear circuit parameters

Foster-like circuit parameters	
L_{dc}= 2.4000 H	R_1= 1722.4899 Ω
L_1 = 4.1518 H	R_2= 22264.6946 Ω
L_2= 4.6595 H	R_∞= 5271.3702 Ω

In general, the agreement between measurement and simulations, for any of the used models, is good. Figure 5.13 is a magnification of Figure 5.12 for the time interval between 0.15 and 0.20s. The two core models produce nearly the same response and are in good agreement with measurements. Another simulation was performed representing the core by a nonlinear inductance only. The current waveform was nearly the same as the constant resistance curve of Figure 5.13.

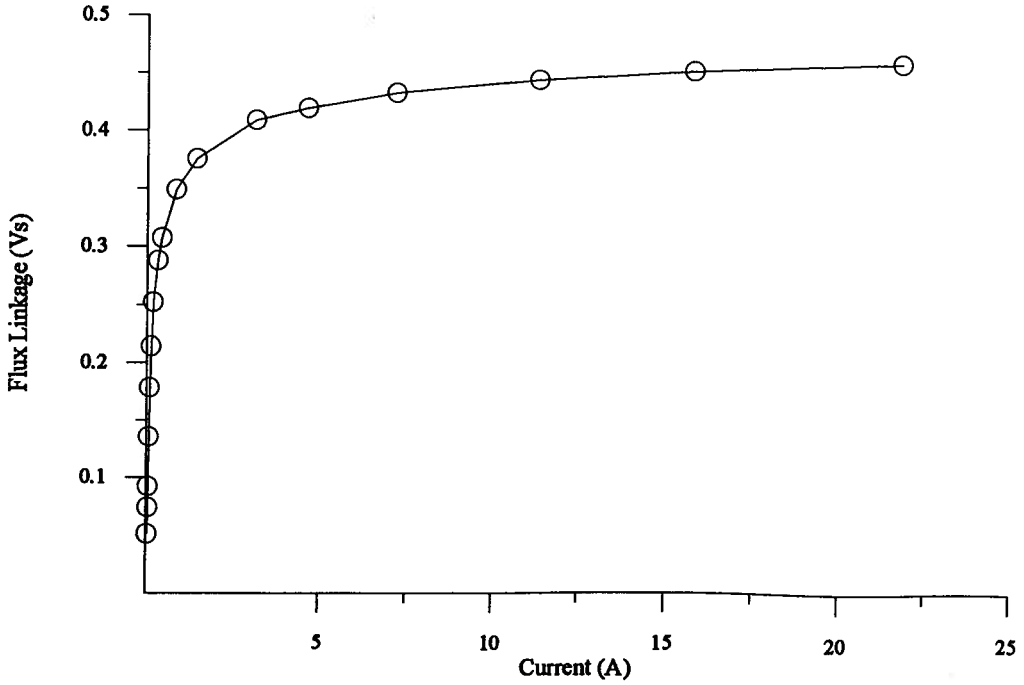

Figure 5.10: Flux-current curve of a single-phase 1 kVA transformer.

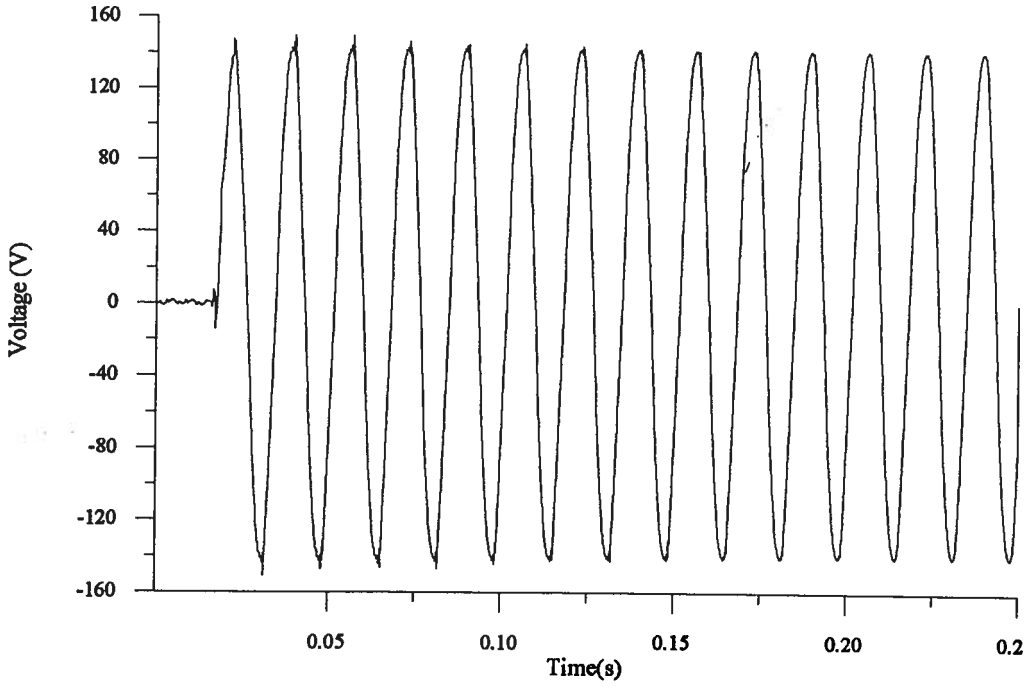

Figure 5.11: Transformer input voltage.

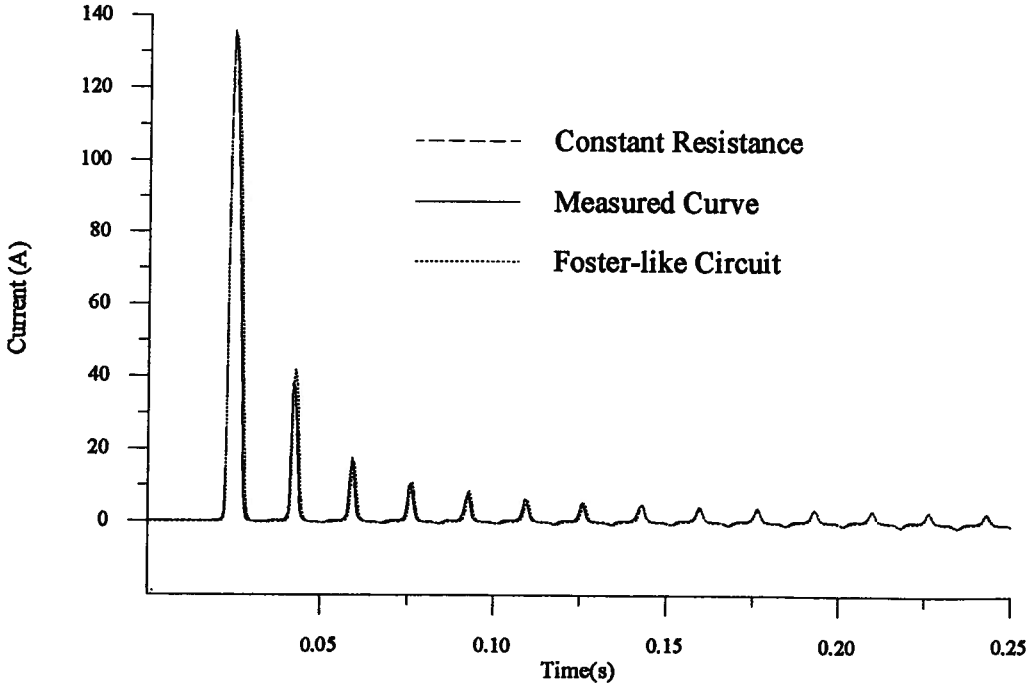

Figure 5.12: Transformer inrush current.

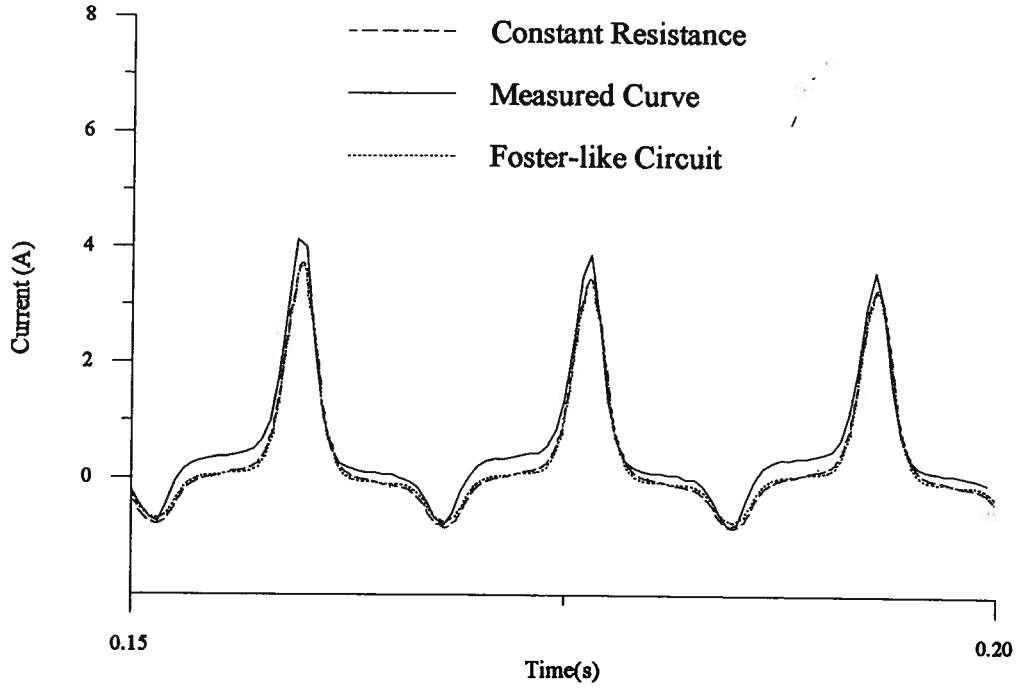

Figure 5.13: Transformer inrush current.

5.6 Ferroresonance

The BPA system of Section 3.4 is simulated once more. Now, the transformer exciting branch is represented by a Foster-like circuit with the parameters calculated for a frequency range from 60 Hz to 3 kHz, assuming the ratio of hysteresis to eddy loss per cycle to be $W_h/W_{eddy}=1$ at 60 Hz [70]. The simulation and field test results are shown in Figure 5.14. The Foster-like circuit produces nearly the same response as a linear resistance in parallel with a nonlinear inductance (see Figure 3.8 in Chapter 3).

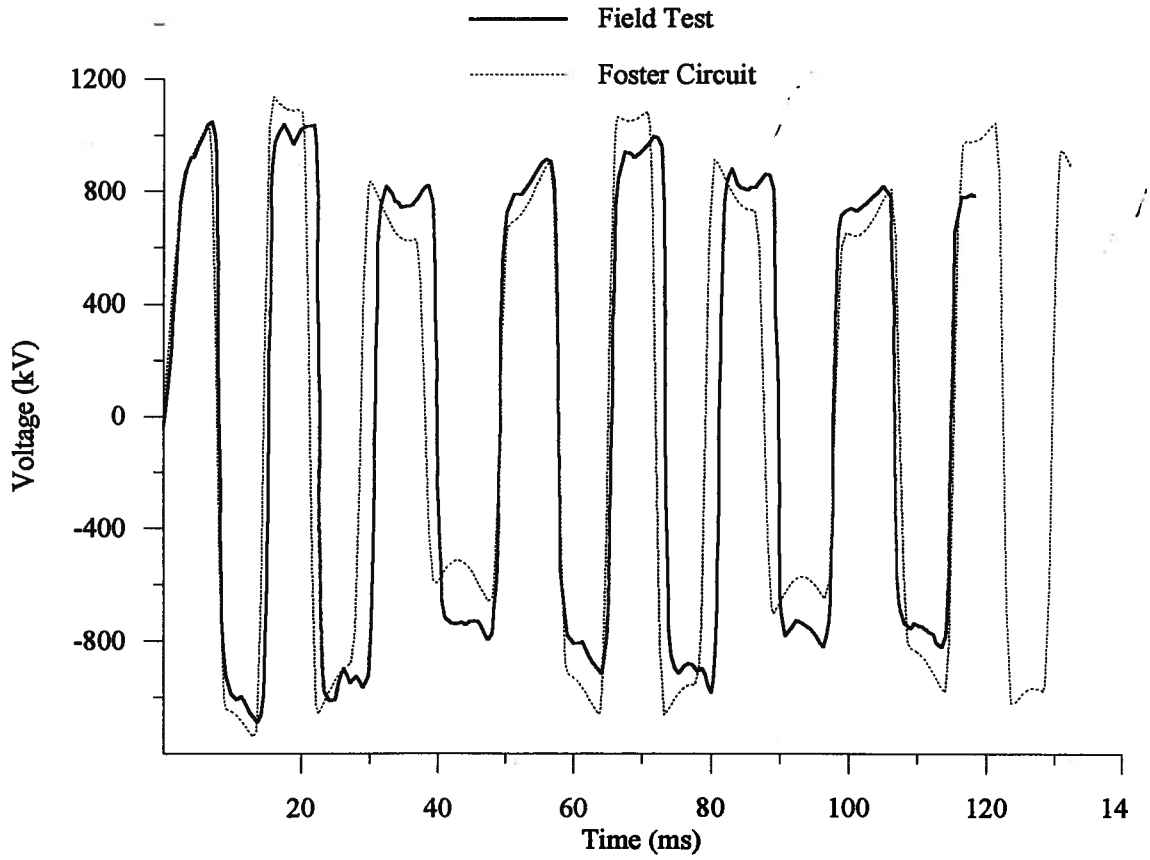

Figure 5.14: Ferroresonance in a power system.

5.7 Summary

An approach to model frequency-dependent effects in the transformer core from core loss data was presented. The parallel Foster-like circuit model, in which hysteresis and eddy current effects are treated simultaneously, was realized. Theoretically, the circuit models can be used for any frequency range (minimum frequency must not be zero).

If the circuit model is used to represent a core in which the hysteresis loss is dominant (e.g. amorphous core [22]), the core loss per cycle is nearly independent of the

frequency. The flux-current trajectories are generated by the circuit models with no need to pre-define them.

An inrush current case and a ferroresonance case were used as test examples. For both cases, there were no major improvements in representing frequency-dependent effects in the core. For the inrush current case, the simple model in the form of a nonlinear inductance reproduced the measured current reasonably well. For the ferroresonance case, a nonlinear resistance (Chapter 3) in parallel with a nonlinear inductance represented the core reasonably well.

It is still premature to say that frequency-dependent effects in the core are not important for all transient cases. More validation tests against other field measurements need to be made in the future, to fully determine their importance for practical applications.

Chapter 6

Transformer Models - Applications

6.1 Introduction

Transformer models based on parameters obtained at 60 Hz, and suitable for frequencies up to 5 kHz, are presented. Frequency-dependent effects in the windings and core nonlinearities are discussed. These models were developed for harmonic studies, as part of a research project for The Canadian Electrical Association, but may be used for transient studies as well. To validate the models, many tests were carried out on several transformer units of different power ratings. Sensitivity studies are performed to show how the total harmonic distortion of current and voltage behaves as the transformer parameters change. A field test involving a transformer, as part of a power system feeding a DC drive, is described as well, for which simulations agree reasonably well with measurements.

6.2 Basic Transformer Equivalent Circuit

Figure 6.1 is the basic transformer model. $Z(j\omega)$ represents the frequency-dependent short-circuit impedance. The excitation branch is represented by nonlinear RL elements obtained from measured *rms* values of voltages and currents(V_{rms}=f (I_{rms})) and no-load losses with the

conversion technique of Chapter 3. These elements should be placed at a point in the equivalent circuit where the integrated voltage is equal to the iron core flux. This point depends on the transformer design and is usually not accessible in the model. However, it can be approximated fairly accurately by connecting the elements to the winding closest to the core (usually the lowest voltage winding) [4].

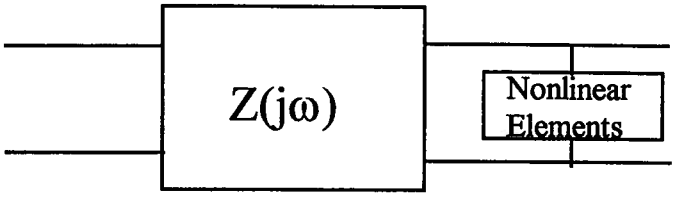

Figure 6.1: Basic transformer model.

6.2.1 Single-Phase Two-Winding Transformer

Consider initially a single pair of magnetically coupled coils as shown in Figure 6.2a. This network can theoretically be described in terms of self and mutual impedances

$$\begin{bmatrix} V_1 \\ V_2' \end{bmatrix} = \begin{bmatrix} Z_{11} & Z_{12} \\ Z_{21} & Z_{22} \end{bmatrix} \begin{bmatrix} I_1 \\ I_2' \end{bmatrix} \Rightarrow [V] = [Z][I], \tag{6.1}$$

or with its inverse relationship

$$\begin{bmatrix} I_1 \\ I_2' \end{bmatrix} = \begin{bmatrix} Y_{11} & Y_{12} \\ Y_{21} & Y_{22} \end{bmatrix} \begin{bmatrix} V_1 \\ V_2' \end{bmatrix} \Rightarrow [I] = [Y][V], \tag{6.2}$$

where $Z_{12} = Z_{21} = Z_M$ and $[Y]=[Z]^{-1}$. V_2' and I_2' are the secondary voltage and the secondary current referred to the primary side, respectively. The elements of [Z] can be found from open-circuit excitation tests. For instance,

$$Z_{21} = \left. \frac{V_2'}{I_1} \right|_{I_2' = 0} \tag{6.3}$$

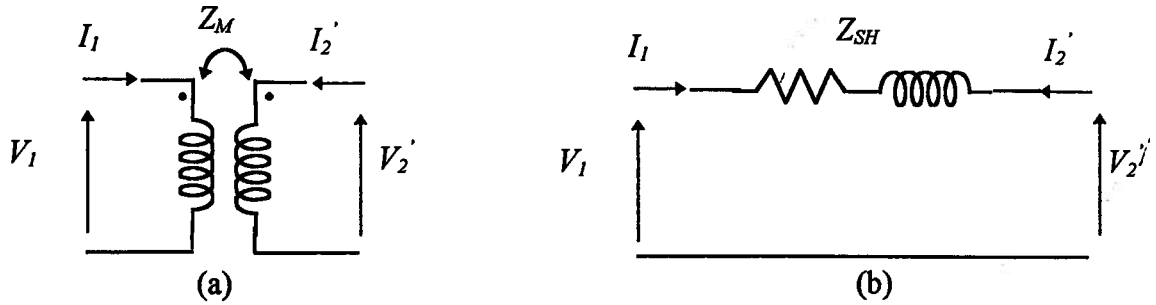

Figure 6.2: Two winding transformer:
a) Pair of magnetically coupled coils;
b) Equivalent circuit referred to primary.

Unfortunately, in practice the magnetic coupling is so high that Z_{21} is approximately equal to Z_{11}. [Z] is then almost singular and its inversion becomes ill-conditioned (one should note that $Z_{11} \cong Z_{22}$). The short-circuit impedances, which are more important than the magnetizing impedances in most studies, get lost. One suitable way to overcome these difficulties is to use the branch admittance matrix [Y] of equation (6.2). Although [Z] becomes infinite for zero exciting current, the [Y] matrix exists and can be found from standard short-circuit tests, as shown later.

For a single pair of magnetically coupled coils, only one short-circuit impedance Z_{SH} exists (Figure 2b). Then, the short-circuit admittance Y_{SH} can be obtained from

$$Y_{SH} = 1 / Z_{SH}. \tag{6.4}$$

To construct [Y], the four elements Y_{11}, Y_{12}, Y_{13}, and Y_{14}, are needed. They can be obtained directly from Figure 6.2b.[1] The 2x2 [Y] matrix is then found from one short-circuit admittance element as

[1] It is useful to note that Y_{11} is the sum of the admittance element connected between the two nodes (Y_{SH}) plus the admittance element connected between node 1 and the reference node (since we are neglecting the exciting current, its value is nil). We can also see that $Y_{11} = Y_{22}$.

$$\begin{bmatrix} I_1 \\ I_2' \end{bmatrix} = \begin{bmatrix} Y_{SH} & -Y_{SH} \\ -Y_{SH} & Y_{SH} \end{bmatrix} \begin{bmatrix} V_1 \\ V_2' \end{bmatrix}. \tag{6.5}$$

Z_{SH} is frequency-dependent and can be reproduced reasonably well by the two branch parallel Foster-like circuit of Figure 6.3a or the series Foster-like circuit of Figure 6.3b as recommended by CIGRÉ[54]. R_S and L_P are the resistance and leakage inductance of the windings at rated frequency. R_P in parallel with the 60 Hz leakage inductance produces the frequency-dependent effects.

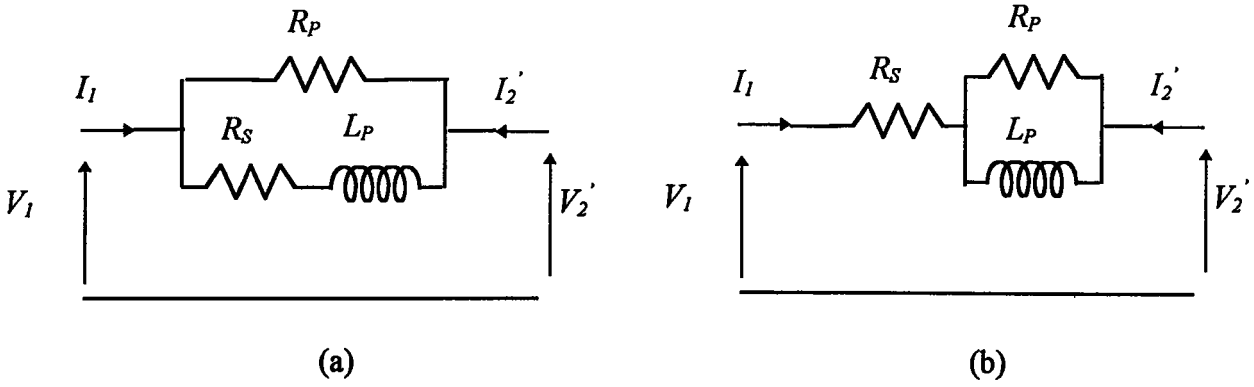

Figure 6.3: Frequency-dependent short-circuit impedance model.

6.2.2 Single-Phase Three-Winding Transformer

Single-phase distribution transformers usually have a grounded tap at the center of the secondary terminals (Figure 6.4a). These transformers are modelled as three-winding transformers (Figure 6.4b). The impedances Z_{PS}, Z_{PT} and Z_{ST} can be found from three short-circuit tests. Unfortunately, these test data are usually not available[4]. The only test usually available is the impedance measurement carried out with the secondary and tertiary terminals grounded to the center terminal. Fortunately, it appears that an accurate value of the short-circuit impedance between primary and secondary is not needed for practical applications since the current flows mainly through the impedances Z_{PS} and Z_{PT} (see Figure 6.4b). It is

therefore reasonable to assume $Z_{PS} = Z_{PT} = Z_{ST}$ referred to the same terminal. In order to produce the frequency-dependent effects in each winding, each branch Z_{PS}, Z_{PT} and Z_{ST} is replaced by the equivalent circuit of Figure 6.3. The core nonlinear elements are obtained from typical V_{rms} - I_{rms} curves, as explained in Chapter 3.

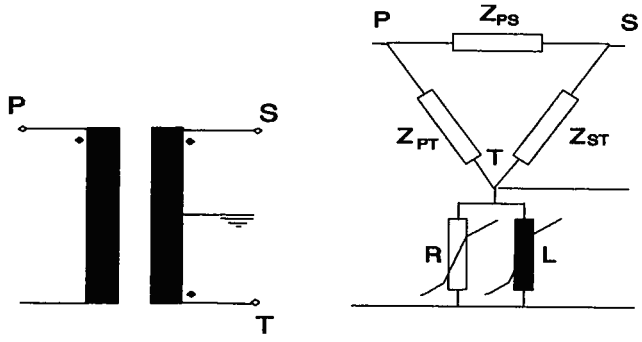

Figure 6.4: Three-winding transformer.
a) Coupled coils;
b) Equivalent circuit.

6.2.3 Three-Phase Transformer

Three-phase transformers are best represented in matrix form. It is simple to extend the single-phase transformer formulation to three-phase two-winding transformers. Equation (6.2) becomes a matrix equation

$$[Y_{SH}] = [Z_{SH}]^{-1}. \tag{6.6}$$

For a short-circuit test performed on a two-winding transformer, the voltages and currents in each phase of the feeding terminal are related according to

$$[V_{ABC}] = [Z_{SH}][I_{ABC}]$$

or

$$\begin{bmatrix} V_A \\ V_B \\ V_C \end{bmatrix} = \begin{bmatrix} Z_{AA} & Z_{AB} & Z_{AC} \\ Z_{BA} & Z_{BB} & Z_{BC} \\ Z_{CA} & Z_{CB} & Z_{CC} \end{bmatrix} \cdot \begin{bmatrix} I_A \\ I_B \\ I_C \end{bmatrix}. \tag{6.7}$$

To obtain each element of $[Z_{SH}]$ in equation (6.7), the short-circuit tests are done according to the circuit of Figure 6.5.

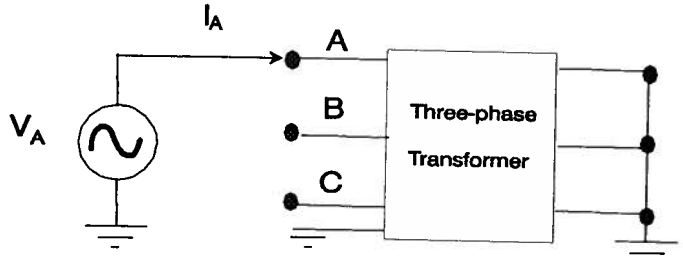

Figure 6.5: Three-phase transformer short-circuit test.

A voltage signal is applied to one phase at a time and the current in that phase and the voltages in A, B and C are then measured. The first column of $[Z_{SH}]$ can be obtained by:

$$Z_{AA} = \frac{V_A}{I_A}\Bigg|_{I_B = I_C = 0};$$

$$Z_{BA} = \frac{V_B}{I_A}\Bigg|_{I_B = I_C = 0}$$

and

$$Z_{CA} = \frac{V_C}{I_A}\Bigg|_{I_B = I_C = 0}.$$

The same procedure applies to the other two columns. Due to symmetry, only six measurements are required to construct $[Z_{SH}]$. In practice, $[Z_{SH}]$ is generally assumed to be balanced ($Z_{AB} = Z_{AC} = Z_{BC}$ and $Z_{AA} = Z_{BB} = Z_{CC}$) and the number of measurements is reduced to two. Positive and zero sequence short-circuit tests are the standard data required to build $[Z_{SH}]$.[2]

[2] For transformers rated 500 kVA and below, only positive sequence tests are available[55].

As explained earlier, since the impedance matrix may become singular, it is convenient to use admittance matrix [Y] formulation. In fact, here we use matrices $[R_s]$ and $[L_P]^{-1}$ or $[\omega L_P]^{-1}$ (imaginary part of [Y]). These matrices are obtained from positive and zero sequence tests and computed by the support routine BCTRAN [4]. $[R_S]$ is a diagonal matrix obtained from positive sequence tests - the zero sequence resistance R_{S0} is assumed to be the same as the positive sequence resistance R_{S+}. The manufacturer provides either the R_{S+} in ohms or the load losses from which R_{S+} can be obtained. Once the matrices are determined, arbritary transformer connections can be realized by node renaming.

Frequency-dependent effects in the short-circuit impedance are treated the same way as for single-phase transformers. Here the elements of Figure 6.3a are all matrices. $[R_p]$ is calculated according to the equation

$$[R_p] = k\,[\omega L], \tag{6.8}$$

Where k is a constant and $[\omega L]$ is the reactance matrix obtained from positive and zero sequence short-circuit reactances. For the representation of the circuits in admittance form, the conductance matrix $[G_p]$ can be used instead of $[R_p]$, where,

$$[G_P] = \frac{1}{k}\,[\omega L]^{-1}$$

The proper way to represent saturation effects is to look at the transformer magnetic circuit. Saturation is related to fluxes in the core and tank. There are several types of core construction. To model the core, one should know what kind of geometry the transformer has. One should know if the transformer is constructed with three different cores, if its core is three-legged, five legged or shell-type. A zero sequence magnetizing impedance can be estimated for each type of core construction.[3] It can be approximated as linear, because of

[3] This probably is not applicable to five-legged transformers constructed from four different cores [69].

fluxes usually passing through air between core elements and the tank. The saturation curve must be obtained for each leg of the transformer and placed across each winding at the secondary terminal to represent the nonlinear effects[4]. If details of core design are not known, the positive sequence saturation curve is placed across each winding.

6.3 Estimation of Transformer Parameters

Measurements were taken to determine the values of the parameters in the transformer equivalent circuit, and to correlate them with the nameplate data. Single and three-phase transformers were tested at Powertech Labs and BC Hydro and Power Authority (Table 6.1). Short-circuit impedance measurements and open-circuit saturation tests ($V_{rms}=f(I_{rms})$ and no-load losses), were performed for the units listed below. The bases of the per unit (p.u.) system used for the short-circuit impedances are rated voltage and power.

6.3.1 Short-Circuit Tests

High frequency currents produced by the signal analyzer HP3562A[4] were injected into the transformers under test. Short-circuit frequency response impedance measurements (real and imaginary values) were recorded as ASCII files on floppy disks.

6.3.1.1 Single-Phase Transformers

In Figure 6.6, some of the measurements of impedances made on the primary side, with the secondary side short-circuited and the tertiary left open, are shown. *R(f)* and *X(f)* represent

[4] The analyzer has a built-in signal source which can produce and measure a scanning signal well above the frequency range of interest. Its measurement range is 64μ Hz to 100 kHz.

the real and imaginary parts of the short-circuit impedance, respectively. Although the transformers have the same rated power and nearly the same short-circuit impedances at 60 Hz, there is a considerable difference in the frequency response behaviour of transformer 1 compared to the others. Differences in coil and core constructions may be the causes of these discrepancies.

Impedances measured on the secondary side, with the tertiary short-circuited and an open primary, are shown in Figure 6.7. It is difficult to correlate Figure 6.6 and 6.7. *X(f)* in Figure 6.7 is, for the whole frequency range, slightly bigger than *X(f)* in Figure 6.6 (transformer 1 behaves in the opposite way). Comparing the measurements of Figure 6.6 and 6.7, it can be seen that Z_{PS} is almost the same as Z_{ST} for transformers 2 and 3. For practical purpose, it is reasonable to assume $Z_{PS}=Z_{ST}$.

Table 6.1: Distribution transformers

Code	Manufacturer (date)	Power (kVA)	Voltage (kV)	Z_{SH}* (%)	Measured 60 Hz Impedance Z_{sh} (%)	R (%)	X (%)
xformer1	***1975***	*50*	*14.4*	*2.18*	-	-	-
xformer2	***May 1992***	*50*	*14.4*	*2.10*	-	-	-
xformer3	***1978***	*50*	*14.4*	*2.10*	-	-	-
xformer4	***1973***	*50*	*7.2*	*2.30*	-	-	-
xformer5	***not available***	*75*	*14.4*	*2.83*	*2.78*	*1.18*	*2.52*
xformer6	***not available***	*100*	*14.4*	*2.10*	*2.03*	*0.77*	*1.88*
xformer7	***not available***	*167*	*14.4*	*2.10*	*2.26*	*0.68*	*2.16*
xformer8	***not available***	*10*	*14.4*	*2.20*	*1.91*	*1.10*	*1.56*
xformer9	***not available***	*25*	*14.4*	*2.10*	*2.01*	*0.89*	*1.80*
xformer10	***not available***	*50*	*14.4*	*2.10*	*1.90*	*0.81*	*1.72*
xformer11	***May 1992***	*10*	*14.4*	*2.20*	-	-	-
xformer12 **	***not available***	*150*	*7.2*	*4.21*	-	-	-
*xformer13***	***not available***	*500*	*7.2*	*5.60*	-	-	-
*xformer14***	***not available***	*75*	*14.4*	-	-	-	-

*nameplate short-circuit impedance **three-phase transformers

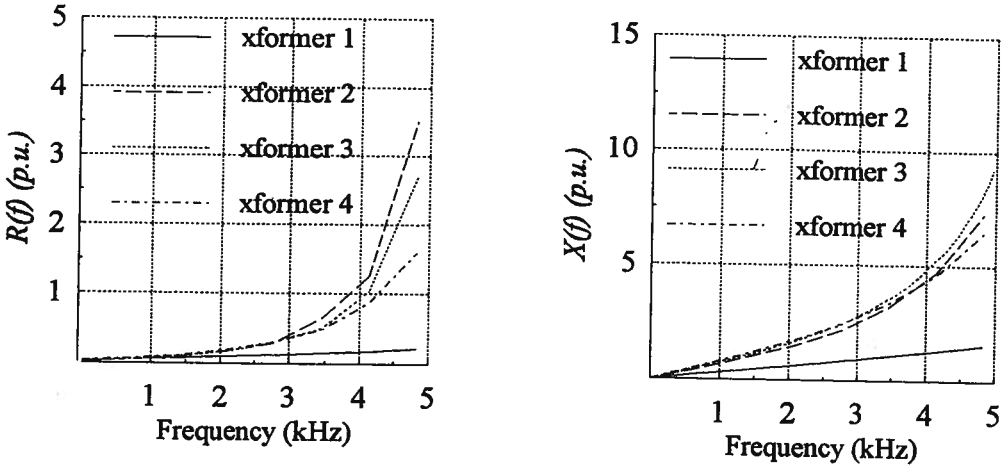

Figure 6.6 : Impedance measured on the primary side

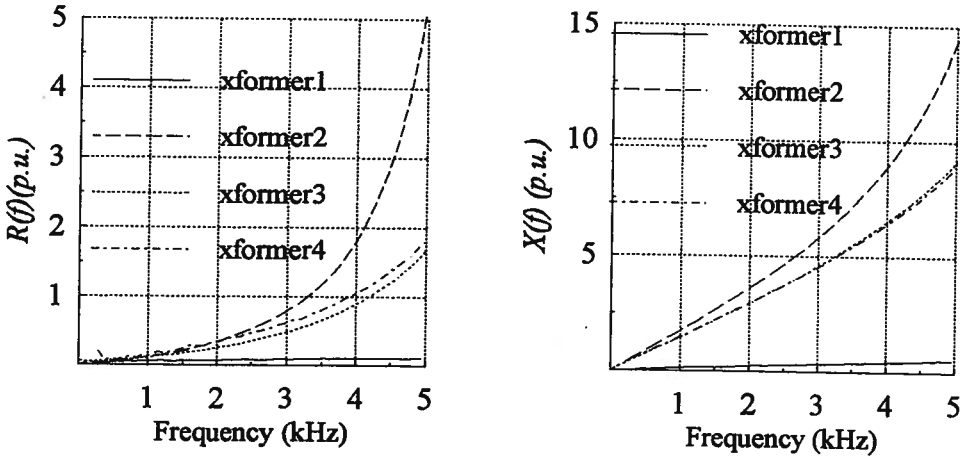

Figure 6.7: Impedance measured on the secondary side.

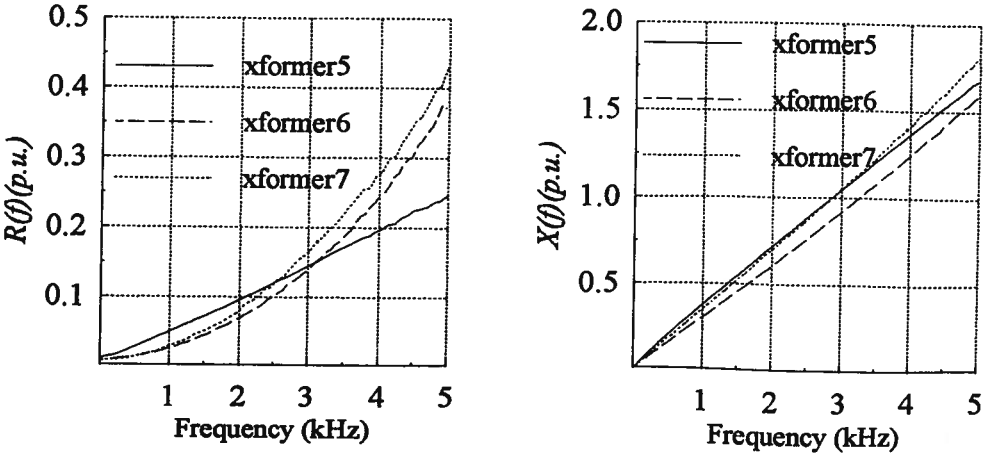

Figure 6.8: Short-circuit impedances of single-phase transformers.

In Figure 6.8 one can see the real and imaginary parts of the short-circuit impedances (transformers 5, 6 and 7) measured the way in which manufacturers probably supply the data to users (measurements are taken on the primary side with the secondary and tertiary grounded to the center terminal). The equivalent impedance seen by the source is Z_{PS} in parallel with Z_{PT} in this case. Measured and simulated L/R curves are shown in Figure 6.9. The solid curves are obtained from measurements. The simulated curves are produced by two parallel circuits of the type of Figure 6.3a.

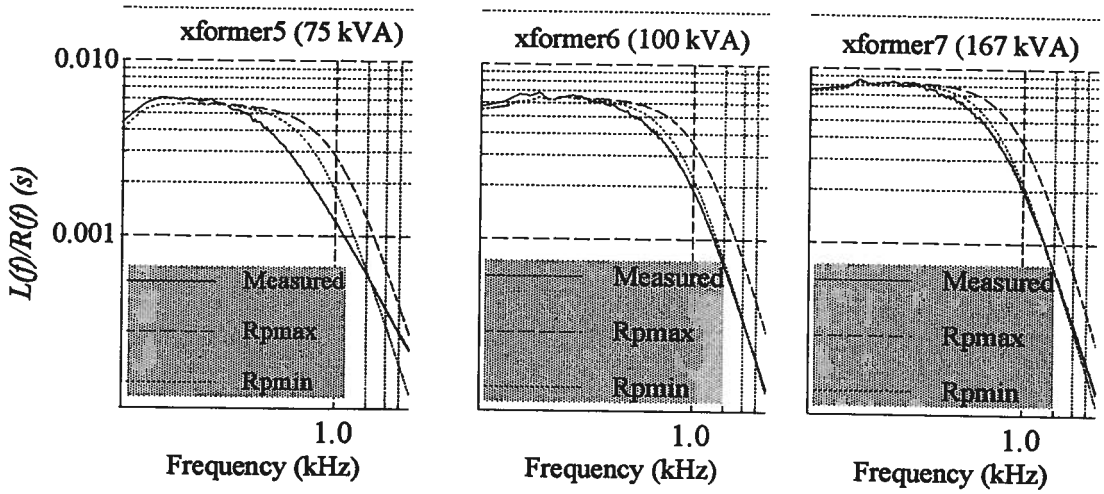

Figure 6.9: Measured and simulated L/R curves.

Two values of resistances R_P are used [54]:

$$R_P = R_{P\max} = 30\,p.u. \quad \text{and} \quad R_P = R_{P\min} = 13\ p.u.\,. \tag{6.9}$$

The real and imaginary parts of the computed short-circuit impedance are calculated as follows:

$$R(f) = \frac{R_S}{2} + \frac{(R_S/2)(\omega L_P)^2}{R_P^2 + (\omega L_P)^2} \tag{6.10}$$

and

$$X(f)=\frac{(R_P^2/2)(\omega L_P)}{R_P^2+(\omega L_P)^2}. \tag{6.11}$$

The 60 Hz resistance R_S is obtained from load losses. It can be seen that the simulated L/R ratios come close to the measured L/R curves (especially for $R_P = R_{pmin}$). For transformers 8,9 and 10 (Figure 6.10) one can see that the $X(f)$ curves are bent upwards, indicating a resonance frequency near the last measured frequency. Stray capacitances need to be included in the model to produce the correct frequency response when one gets close to resonance points. The first resonance frequency for all tested single-phase transformers is between 6 and 60 kHz. A similar resonance frequency range was found previously by Ontario Hydro[56].

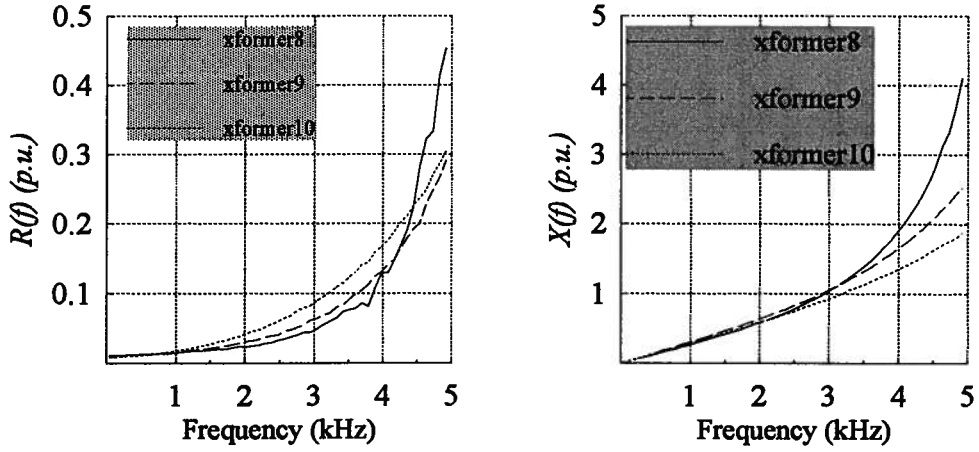

Figure 6.10: Short-circuit impedance frequency response.

6.3.1.2 Three-Phase Transformers

The short-circuit impedance measurements were performed according to the circuit of Figure 5.5. The impedance measured at each phase (self impedance) of transformers 12, 13 and 14 are shown in Figure 6.11, 6.12 and 6.13. The mutual impedances were measured as well and found to be negligible for the 500 kVA and 150 kVA transformer (they were less than an order of magnitude of the self impedances).

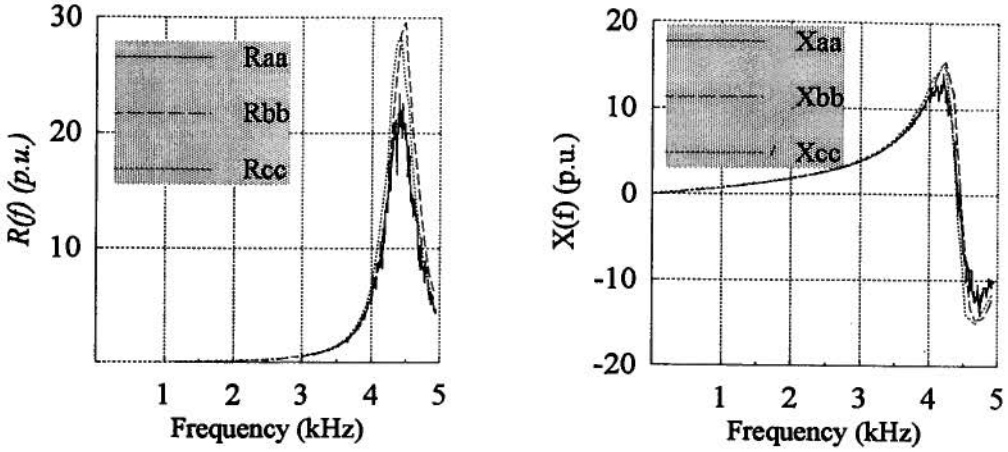

Figure 6.11: 150 kVA three-phase transformer (self impedances).

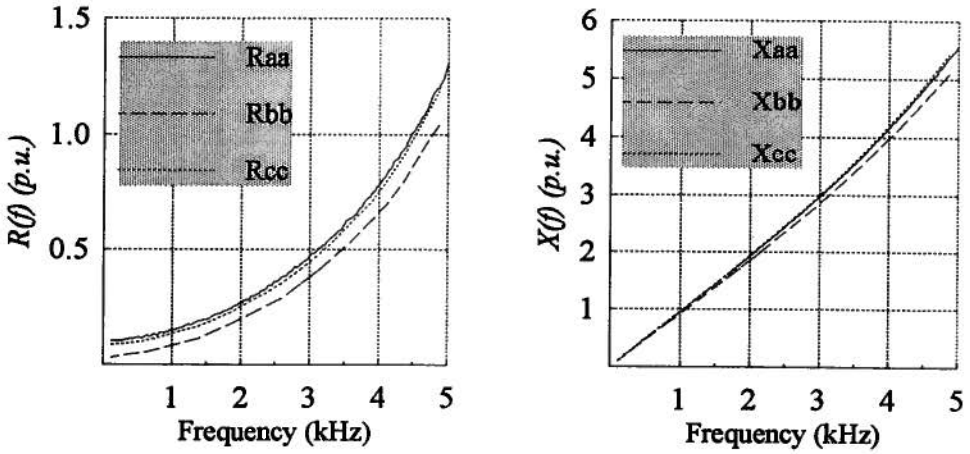

Figure 6.12: 500 kVA three-phase transformer (self impedances).

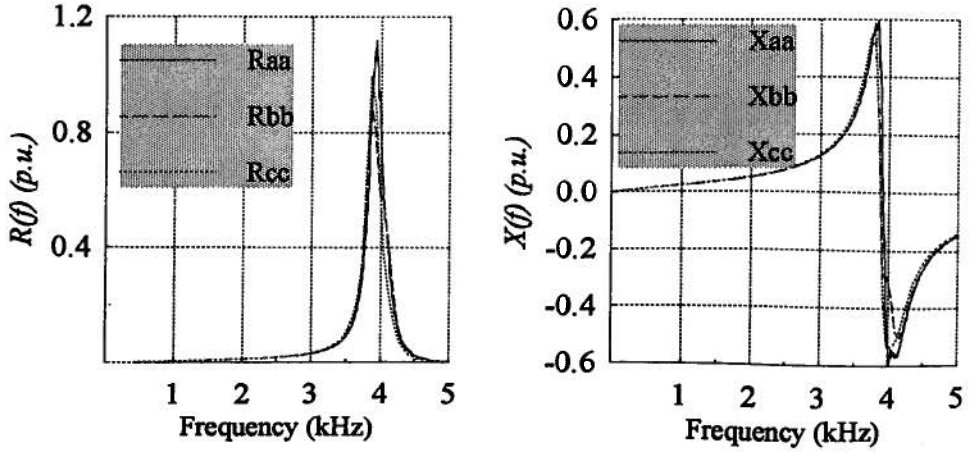

Figure 6.13: 75 kVA transformer short-circuit impedances(self impedances).

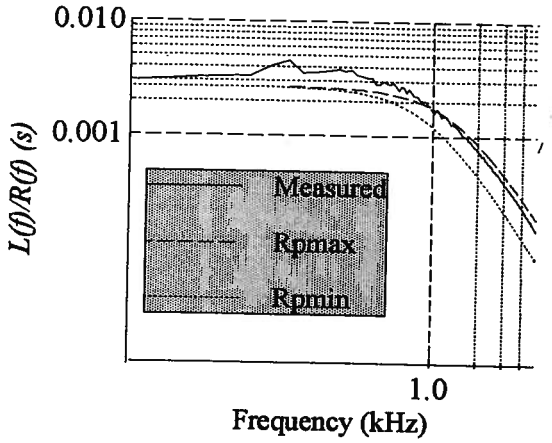

Figure 6.14: 500 kVA transformer L/R curve.

Each phase of the 500 kVA or 150 kVA transformer could therefore be simulated as a single-phase two-winding transformer. In Figure 6.14, simulated and measured (solid lines) L/R curves for the 500 kVA transformer are shown. R_P is obtained from equation (6.9). Simulated curves come close to the one obtained from measurements (especially for $R_P = R_{pmax}$). For this example the parameter k in equation (6.8) is:

$$k = \frac{30}{\omega L_+},$$

where ωL_+ is the positive-sequence short circuit reactance at rated frequency.

For the 75 kVA transformer, the mutual impedances were of the same order of magnitude of the self impedances.The matrix form would therefore be more appropriate to represent this transformer. Unfortunately, for three-phase distribution transformers, only positive sequence data are usually available from manufacturers.

6.3.2 Open Circuit Tests

In the open circuit tests, the low voltage winding is excited with a nearly sinusoidal voltage source at 60 Hz to obtain the transformer saturation characteristics. No-load losses

and *rms* current were measured for different *rms* voltage levels. The *x*-axis of Figure 6.15a is the ratio of the *rms* exciting current I_{exc} to the *rms* exciting current $I_{exc\text{-}rated}$ at rated voltage for single-phase transformers 1,2,3,4 and 8. The y-axis is the ratio of the *rms* exciting voltage V_{exc} to the rated voltage $V_{exc\text{-}rated}$. The solid line is the average curve. Below rated voltage, saturation curves differ very much from each other. However, for harmonic and transient studies, the representation above rated voltage is more important and in this region the curves come close to each other.

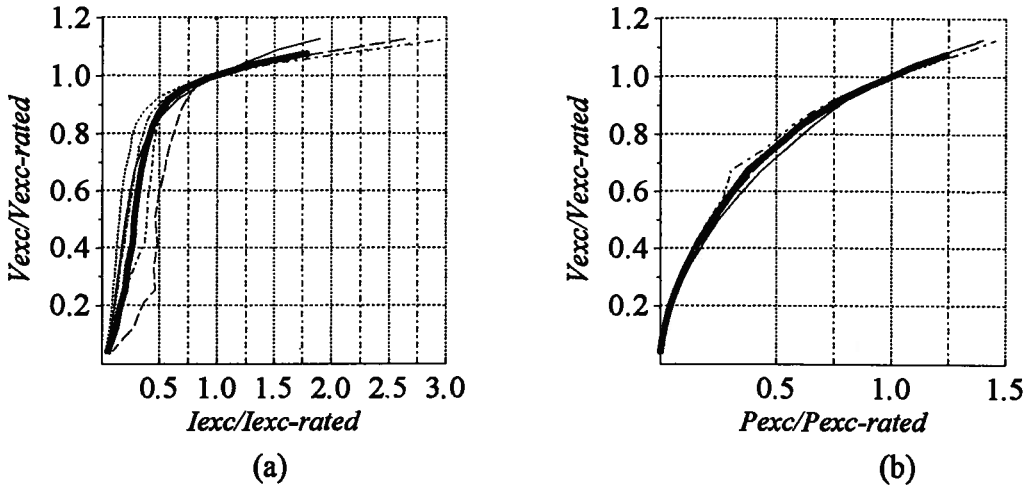

Figure 6.15: Single-phase transformers.
a)V_{rms} - I_{rms} characteristics;
b) V_{rms} - average power curves.

The *x*-axis of Figure 6.15b is the ratio of the no-load exciting losses P_{exc} to the no-load losses at rated voltage $V_{exc\text{-}rated}$ for the same transformers. The solid line represents the average curve.

For three-phase transformers open-circuit tests are usually performed for positive sequence. Figure 6.16 is the measured positive sequence excitation characteristic of the three-phase 75 kVA transformer. one can see how the exciting current through each phase (solid line is the average curve) behaves as the exciting voltage changes.

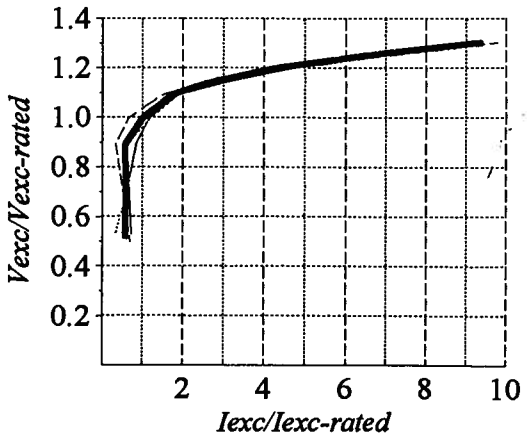

Figure 6.16: V_{rms} -I_{rms} characteristic for a 75 kVA three-phase transformer.

Typical distribution transformer correction factors that should be applied to no-load losses at rated voltage to give the correct losses when the transformers are driven into saturation, are shown in Table 6.2[44]. Agreement between this table and the solid line curves of Figures 6.15 and 6.16 is reasonably good.

Table 6.2 -Correction factors

	Correction Factors		
Operating Voltage (%)	No-load Loss	Exciting Current	kVA rating
105	1.15	1.50	For 167 kVA and below (1ϕ)
110	1.30	2.20	For 150 kVA and below (3ϕ)
105	1.50	2.30	For 250 kVA and above(1ϕ)
110	2.40	4.60	For 225 kVA and above (3ϕ)

6.3.2.1 Stray Capacitances

The V_{rms}-I_{rms} curve shown in Figure 6.17 was obtained from a recently manufactured transformer (xformer11 - Table 6.1). The *rms* current at 90% of the rated voltage is smaller than

the *rms* current at 50% of the applied voltage. Here, the exciting current is very much affected by stray capacitances.

A crude estimation of the saturation curves and the open-circuit capacitance can be found iteratively. First, the algorithm generates the peak flux-current characteristic "corrupted" by stray capacitance effects as shown in Figure 6.17b. The peak current is decreasing in the region between points A and B. Since The inductance is very high in this region. It can be assumed that it is infinite between turning points A and B. The peak current I_c through the open circuit capacitance C_{open} is then the horizontal distance between turning point A and any point in between A and B. For instance at point B, the open-circuited capacitance can be obtained from:

$$C_{open} = \frac{I_C}{\omega^2 \lambda_B}.$$

In Table 6.3, the "corrupted" flux-current points were obtained using Figure 6.17a as input data.

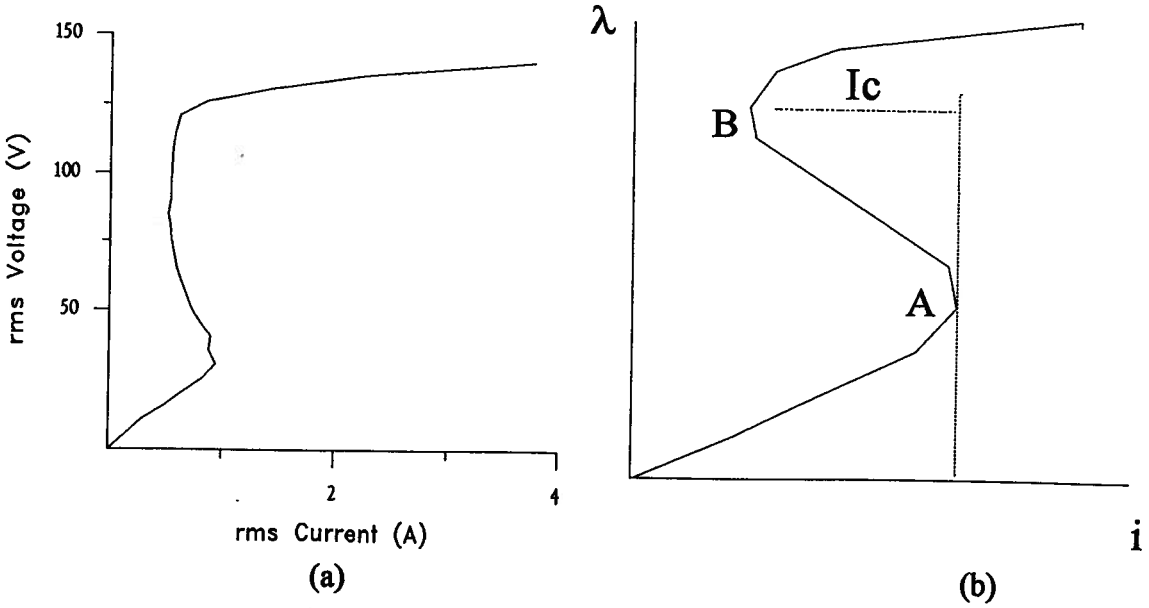

Figure 6.17: Newly manufactured transformer.
a) V_{rms} - I_{rms} curve;
b) Corrupted flux-current curve (not to scale).

Table 6.3: Corrupted flux-current curve.

Flux Linkage(Vs)	Current(A)
0.000000	0.0000000
0.040327	0.426281
0.059046	0.747657
0.075777	0.905318
0.095659	1.193316
0.114790	1.240726
0.151553	0.815392
0.169560	0.396883
0.189066	0.123851
0.207823	0.162665

The following information is needed:

peak current at turning point A = 1.240726 A;

peak current at turning point B = 0.123851 A;

peak flux at turning point B = 0.189066 Vs.

Then, the open circuit capacitance referred to the 120 V side is

$$C_{open} = \frac{1.240726 - 0.123851}{(2\pi \times 60)^2 \times 0.189066} \cong 41.56\,\mu F.$$

If C_{open} is needed to be referred to the high voltage terminal,

$$C_{open} = 41.56 \times (120/14400)^2 \cong 2.89\,\eta F.$$

The C_{open} could then be split into three parts and placed between each transformer terminal and ground of Figure 6.4b. Although the open circuit capacitances affect the exciting current, the first resonance frequency for this transformer was above 6 kHz.

6.4 Sensitivity Study

The frequency-dependent short circuit impedances of transformer 5 are obtained from nameplate data in the way explained in Section 6.3.1. The V_{rms}-I_{rms} curve and no-load losses are measured in the laboratory and the nonlinear core parameters are calculated. Numerical simulations using the MHLF program[57] are carried out to see how the total harmonic distortion(THD) of the primary current and secondary voltage are affected by changes in the short-circuit parameter R_p (see equation 6.11), and in a balanced linear load connected half to the secondary and half to the tertiary terminal.[5] Stray capacitances are neglected. The transformer primary terminal is excited with a sinusoidal voltage and driven into saturation. The simulation results are shown in Table 6.4. Rp has little effect in the primary current and in the secondary voltage. From the last two rows one should note that at full load the nonlinear shunt elements are of minor importance (the harmonics produced by them are of small amplitude). The load model is more important than the nonlinear excitation branch model.

Table 6.4 - Sensitivity study.

Voltage (p.u.)	Load (p.u.)	Load Power Factor	Rp(p.u.)	THD Primary Current (%)	THD Secondary Voltage (%)
1.05	0.00	-	13.0	19.317	0.312
1.05	0.00	-	30.0	18.900	0.317
1.10	0.00	-	13.0	26.041	0.542
1.10	0.00	-	30.0	25.488	0.550
1.05	1.00	0.60	13.0	0.041	0.171
1.10	1.00	0.60	30.0	0.065	0.280

[5] THD is the ratio between the total *rms* value of the harmonics and the *rms* value of the fundamental [71].

6.5 Field Test

In Figure 6.18, three three-phase 500kVA transformers, connected to a 12 kV three-phase power system, feed a 1500 HP DC Drive. Currents and voltage waveforms were measured at both transformer terminals. The current and voltage waveforms at the 12 kV side are shown in Figure 6.19 and in Figure 6.20. In Figure 6.21 one can see plots of measurements and simulations of the line voltage at delta side when the DC drive is on low load. Frequency-dependent effects in the windings and the nonlinear effects in the core are neglected (the transformer is represented as a constant RL short-circuit branch).[6] Solid lines are computed curves and dotted curves were obtained from measurements. One can see that there is a good agreement between measurements and simulations. The difference between curves may be attributed to measurement noise.

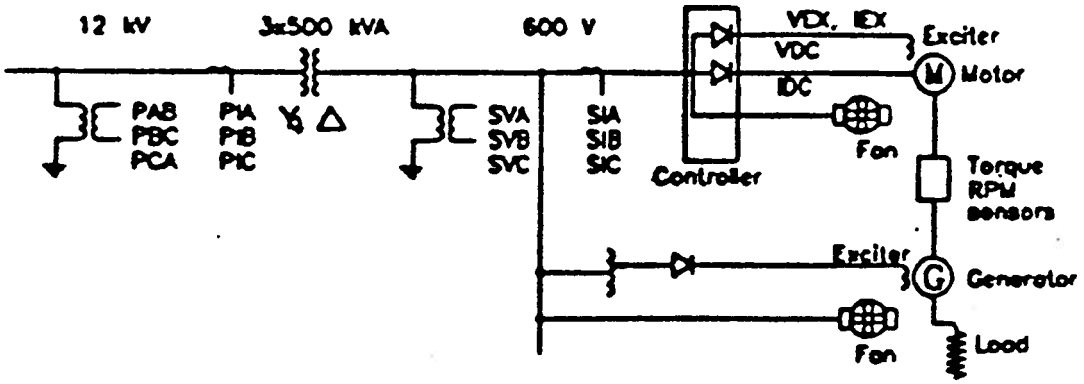

Figure 6.18: DC drive set up.

[6] Here, the measured primary voltage, current and the short circuit impedance were the required data. In fact, voltage and current waveforms were saved as ASCII files and converted from time-domain to phase-domain to be used as input sources in the MHLF program .

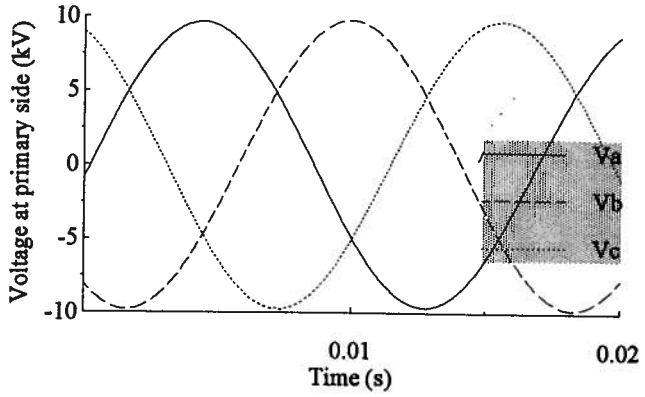

Figure 6.19: Measured voltage waveform.

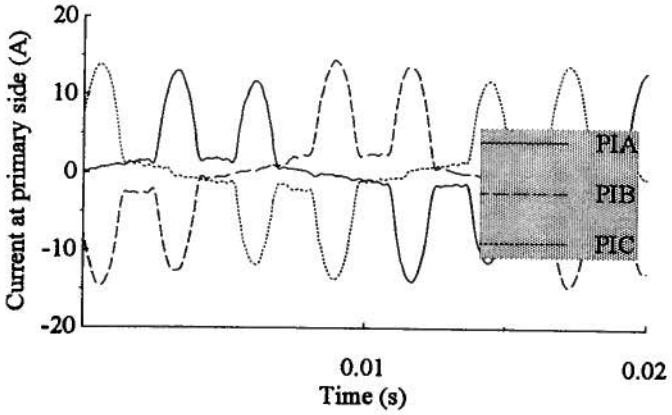

Figure 6.20: Measured current waveform.

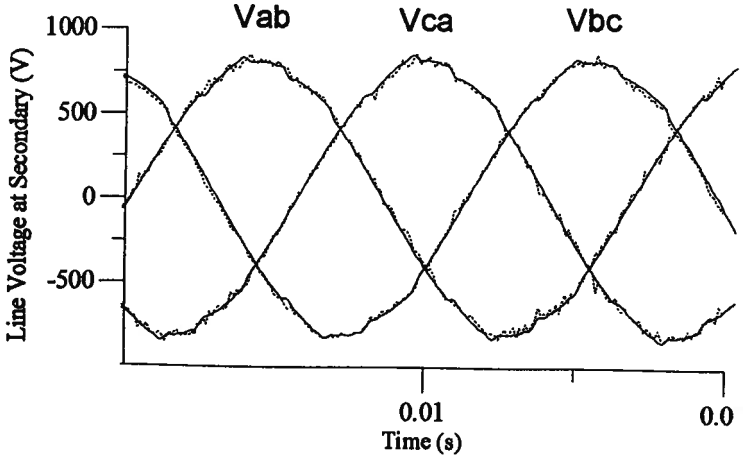

Figure 6.21: Transformer secondary line voltage.

6.6 *Summary*

Transformer models for harmonic studies were presented. They are derived from 60 Hz manufacturer's data. Short-circuit impedance and open circuit saturation tests were performed, the parameters of the transformer equivalent circuits were determined and correlated to nameplate data. The transformer equivalent circuits reproduce the measured short-circuit impedances reasonably well if stray capacitances are negligible for the frequency range of interest in harmonic studies (60 Hz to 5 kHz). If stray capacitances are important (resonance for short-circuit test close to 5 kHz), it is better to add shunt capacitances to the transformer model. These capacitances are determined by low-frequency or resonance measurements, or taken as typical values from publications or textbooks [58-60].

Typical saturation curves for single-phase and three-phase transformers are presented. For situations in which the exciting current includes strong capacitive effects, a crude estimation of the open circuit capacitance can be made if saturation V_{rms} - I_{rms} curves and no-load losses are provided.

Sensitivity studies indicate that the load plays an important role in the harmonic contents of terminal voltages and currents. In general, the representation of the core is less important than the representation of the short-circuit impedance and the load.

In general, at steady state, transformers usually do not experience deep saturation(flux in the core may be only a few percent higher than the rated flux). To predict the exciting current for a practical case is extremely difficult since, even for the same transformer rating (see Figure 6.15), the saturation curves may differ very much from each other. However, the exciting current, although distorted, is very small and will not affect the simulation results. The simplest model of the transformer was able to reproduce the field test reasonably well.

It is advisable to include the nonlinear effects of the core for situations in which resonance may occur (for instance, the transformer is unloaded or supplying a light load). The transformer could be driven into a deeper saturated level. The exciting current should not be neglected here, and similarly to the inrush current case of the last chapter, in the saturated region, the exciting current is likely to be predicted with reasonable accuracy provided the saturation curves are known up to deep saturation.

Chapter 7

Conclusions

Iron core nonlinearities may play a very important role in transient studies. In the following paragraphs, the major contributions of this research work are outlined.

A direct method for producing saturation curves from readily available transformer test data as supplied by manufacturers, was presented. The algorithm is easy to implement and may be useful for electromagnetic transient programs.

A method for more correctly representing the saturation curve of a delta-connected transformer, suitable for situations in which the tests are performed with a closed delta, was developed. It uses positive sequence excitation test data as input and takes into consideration the removal of triplen harmonics from the line current. The algorithm is iterative and easy to implement.

An approach to model frequency-dependent effects in the transformer core from transformer no-load loss data, was presented. The parallel Foster-like circuit model, in which hysteresis and eddy current effects are treated simultaneously, were realized. The flux-current trajectories are generated by the circuit models with no need to pre-define them.

Practical applications of transformer models for harmonic studies were presented. The transformer models were derived from manufacturer's data and may be used for transient studies as well. In general, when the transformer is not in deep saturation, the exciting current, although distorted, is very small and will not affect the simulation results. It is advisable to include the nonlinear effects of the core only for situations in which resonance may occur (for instance, when the transformer is unloaded or supplying a light load).

A method for crudely estimating the transformer open circuit capacitance from saturation V_{rms} - I_{rms} curves and no-load losses, was presented. It is useful for situations in which the exciting current includes strong capacitive effects.

Two case studies involving transients were investigated: an inrush current test in a 1 kVA transformer and a ferroresonace field test. For the inrush current test, the simple core model (a nonlinear inductance) reproduced the measured current reasonably well. For the ferroresonance test, a simple core model (nonlinear resistance in parallel with a nonlinear inductance) also represented the core reasonably well. Theoreticaly, this core model is limited to a single frequency. At frequencies both lower and higher than fundamental the model would not produce the frequency-dependent core behaviour. However, for these case studies, there was no need to include frequency-dependent effects.

For future work, there is a need to further test the core models against other field measurements, to fully determine the importance of frequency-dependent core models for practical applications. There is also a possibility of computing saturation curves of delta-connected transformers directly without iterations. This would save computer time, and make the solution algorithm more reliable.

References

1. P.A.Abetti, *Bibliography on the Surge Performance of Power Transformers and Rotating Machines,* Trans.AIEE, vol. 77, 1958, pp. 1150-1168.

2. C. Degeneff, *A Method for Constructing Terminal Models for Single-Phase N-Winding Transformers,* Paper A78 539-9, presented at IEEE PES Summer Meeting, Los Angeles, Calif., July 16-21, 1978.

3. L. Nakra, *Behaviour of Circuits with Ferromagnetic Nonlinearity,* Chapter 1, Ph. D. Thesis, McGill University, Montreal, August 1973.

4. H. W. Dommel, *Electromagnetic Transients Program Reference Manual,* Section 6, Department of Electrical Engineering-The University of British Columbia, Vancouver, 1986.

5. F. L. Alvarado, *Eletromagnetic Transients Program (EMTP),* EPRI, EL-4561, Vol. 3, The University of Wisconsin at Madison, Madison, Wisconsin, June 1989.

6. W. F. Tinney, *Compensation Methods for Network Solutions by Optimally Ordered Triangular Factorization,* IEEE Trans. Power App. Syst., vol. PAS-91, Jan./Feb. 1972, pp. 123-127.

7. J.G. Frame, N. Mohan and T. Liu, *Hysteresis Modeling in an Electromagnetic Transients Program,* IEEE, Trans. Power App. Syst.,vol. PAS-101, Sept. 1982, pp. 3403-3412.

8. B. Mork and K. S. Rao, *Modeling Ferroresonance with EMTP* , EMTP-Newsletter, vol. 3, No. 4, May 1983, pp. 2-7.

9. E. P. Dick and W. Watson, *Transformer Models for Transient Studies Based on Field Measurements* , IEEE Trans. Power App. Syst, vol. PAS-100, No. 1, Jan. 1981, pp. 409-419.

10. N. Germay, S. Mastero and J. Vroman, *Review of Ferroresonance Phenomena in High Voltage Power System and Presentation of a Voltage Transformer Model for Predetermining Them,* CIGRE', Paris, paper 33-18, 1974

11.G. Biorci and D. Pescetti, *Analytic Theory of the Behaviour of Ferromagnetic Materials*, Nuovo Cimento, vol. 7, No. 6, 1958, pp. 829-842.

12. I. D. Mayergoyz, *Mathematical Models of Hysteresis*, Springer-Verlag, 1991

13.J.L. Binard, *Hysteresis Model For Power Transformer Transient Simulation Program*, EMTP Newsletter, Vol. 7, No. 3, Sept. 1987.

14.J.G. Santesmases, J. Ayala, S. H. Cachero, *Analytical Approximation of Dynamic Hysteresis Loops and its Application to a Series Ferroresonant Circuit* , Proc. IEE 117, No. 1, January 1970, pp. 234-240.

15.L. O. Chua and K. A. Stromsmoe, *Lumped Circuit Models for Nonlinear Inductors Exhibiting Hysteresis Loops*, IEEE Trans. on Circuit Theory, vol. CT-17, No. 4, Nov. 1970, pp. 564-574.

16.E.J. Tarasievicz, A. S. Morched, *Detailed Transformer Model for EMTP; Part 1: Eddy Current Representation*, EMTP Review, Vol. 3, No. 4, October 1989.

17.E.J. Tarasievicz, A. S. Morched, A. Narang and E. P. Dick, *Frequency Dependent Eddy Current Models for Nonlinear Iron Cores*, IEEE Transactions on Power Systems, Vol. 8, No. 2, May 1993, pp.588-597.

18. J. Avila-Rosales and F. L. Alvarado, *Nonlinear Frequency Dependent Model for Electromagnetic Transient Studies in Power Systems* , IEEE Trans. Power App. Syst, vol. PAS-101, Nov. 1982, pp. 4281-4288.

19.J. Avila-Rosales and A. Semlyen, *Iron Core Modeling for Electrical Transients*, IEEE Trans. Power App. Syst., vol. PAS-104, No. 11, Nov. 1985, pp. 3189-3194.

20.F. De Leon and A. Semlyen, *Time Domain Modeling of Eddy current Effects for Transformer Transients*, IEEE Transactions on Power Delivery, Vol. 8, No. 1, January 1993, pp.271-280.

21.F. Keffer, *The Magnetic Properties of Materials*, Scientific American, vol.217, No. 3, pp. 222-234.

22.G. E. Fish, *Soft Magnetic Materials*, Proceedings of the IEEE, Vol. 78, No. 6, June 1990, pp. 947-972.

23.P.J. Nahin, *Oliver Heaviside: Sage in Solitude*, IEEE Press, New York, 1987, pp. 109.

24. M. Latour, *Note on Losses In Sheet Iron at Radio Frequencies,* Proceedings of the Institute of Radio Engineers, V.7, 1918, pp. 61-71

25.T. H. O'Dell, *Ferromagnetodynamics*, Chapters 1 and 5, Mcmillan Press Ltd, London, 1981.

26.H. J. Williams, W. Shockley and C. Kittel, *Studies of Propagation Velocity of a Ferromagnetic Domain Boundary* , Phys. Rev. 80, 1950, pp. 1090-1094

27.P. D. Agarwal and L. Rabins, *Rigorous Solution of Eddy Current Losses in Rectangular Bar for Single Plane Domain Wall Model,* Journal of Applied Physics, Suplement to vol. 31 No. 5, May 1960, pp. 246S-248S.

28.C. W. Chen, *Magnetism and Metalurgy of Soft Magnetic Materials*, North Holand Publishing Company, New York, 1977.

29.F. Brailsford, *Investigation of the Eddy Current Anomaly in Electrical Sheet Steels*, J. IEE, 1948, No. 95, Pt. 2, pp. 121-125.

30.K. J. Overshott, I. Preece and J. E. Thompson, *Magnetic Properties of Grain-Oriented Silicon Iron, Part 2 - Basic Experiments on the Nature of the Anomalous Loss Using an Individual Grain,* Proc. IEE, Vol. 115, No. 12, December 1968, pp.1840-1845.

31.T. Spooner, *Properties and Testing of Magnetic Materials*, McGraw-Hill, 1927.

32.C. Heck, *Magnetic Materials and Their Applications*, (English translation from the German),Chapter 10, Butterworth & Co. Ltd, 1974, pp. 337.

33.S.L. Burgwin, *Measurement of Core Loss and A.C. Permeability with the 25 cm Epstein Frame*. Proceedings, Am, Soc. Testing Mats., ASTEA Vol. 41, 1941 pp. 779-796.

34.G. Herzer and H. Hilzinger, *Recent Developments in Soft Magnetic Materials*, Physica Scripta, Vol. T24, 1988, pp. 22-28.

35.A. J. Moses, *Recent Advances In Experimental Methods For The Investigation of Silicon Iron,* Physica Scripta, Vol. T24, 1988, pp. 49-53.

36.F. J. Wilkins and A. E. Drake, *Measurement and Interpretation of Power Losses in Electrical Sheet Steel*, Proc. IEE Vol 112, No. 4, April, 1965, pp. 771-785

37.A. Basak and A.A.A. Qader, *Fundamental and Harmonic Flux Behaviour In a 100kVA Distribution Transformer Core*, IEEE Trans. on Mag., Vol. Mag -19, No.5, September 1983, pp. 2100-2102.

38. Stanley H. Charap, *Magnetic Hysteresis Model*, IEEE Trans. on Mag., vol. Mag -10, No. 4, December 1974, pp. 1091-1096.

39.T. Nakata, *Numerical Analysis of Flux and Loss Distribution in Electrical Machinery*, (Invited Paper), IEEE Trans. on Magnetics, Vol. Mag - 20, No. 5, September, 1984.

40.R. J. Larry and L. R. Turner, *Survey of Eddy Current Programs*, IEEE Trans. on Magnetics, Vol. Mag -19, No. 6, November 1983, pp.2474-2477.

41.G.W. Swift, *Power Transformer Core Behavior Under Transient Conditions*, IEEE Trans. Power App. Syst,vol. PAS-90, No.5, September/October, 1971, pp. 2206-2210.

42.H. W. Dommel, A. Yan, R. J. Marcano and A. B. Milliani, *Case Studies For Electromagnetic Transients*, UBC Department of Electrical Engineering Internal Report, Vancouver, 1983.

43.Microtran Power System Analysis Corporation, *Transient Analysis Program Reference Manual*, Vancouver, Canada, 1991.

44.Westinghouse Electric Coorporation, *Electric Utility Engineering Reference Book*, Vol. 3, Distribution Systems, Chapter 6, Pittsburgh, Pensylvania, 1959.

45.S. Prusty and M. V.S. Rao, *A Direct Piecewise Linearized Approach to Convert rms Saturation Characteristic to Instantaneous Saturation Curve*, IEEE Transactions on Magnetics, Vol. Mag-16, No.1, January 1980, pp. 156-160.

46.W. L. A. Neves and H. W. Dommel, *On Modelling Iron Core Nonlinearities*, IEEE Transactions on Power Systems, Vol. 8, No. 2, May 1993, pp. 417-425.

47.W. L. A. Neves, H. W. Dommel, *Saturation Curves of Delta-Connected Transformers From Measurements*, to appear in IEEE Transactions on Power Delivery. Paper 94 SM 459-8 PWRD presented at IEEE PES Summer Meeting, July 24-28, 1994, San Francisco, CA.

48.W. L. A. Neves, H. W. Dommel and Wilsun Xu, *Practical Distribution Transformer Models for Harmonic Studies*, to appear in IEEE Transactions on Power Delivery. Paper 94 SM 406-9 PWRD presented at IEEE PES Summer Meeting, July 24-28, 1994, San Francisco, CA.

49.A. Otter and W. Neves, *Loss Measurement Programs at TRIUMF*, Proceedings of The Kaon PDS Magnet Design Workshop, TRIUMF, Vancouver, October 3-5, 1988, pp. 132-135.

50.M. B. Stout, *Basic Electrical Measurements*, Section 16-8, New York, Prentice Hall Inc., 1950.

51.S.N. Talukdar, J.K. Dickson, R.C. Dugan, M.J. Sprinzen, C.J. Lenda, *On Modeling Transformer and Reactor Saturation Characteristics for Digital and Analog Studies*, IEEE Trans. on PAS, vol. PAS-94, 1975, pp. 612-621.

52.C. G. A. Koreman, *Determination of the Magnetizing Characteristic of Three-Phase Transformers in Field Tests*, IEEE Transactions on Power Delivery, Vol. 4, No. 3, July 1989, pp. 1779-1785.

53. Leuven EMTP Center (LEC), *ATP Rule Book*, Section XIX-G, Revision July, 1987.

*54.*CIGRÉ Working Group 36.05, *Harmonic, Characteristic Parameters, Methods of Study, Estimates of Existing Values in the Network*, Electra No. 77, pp. 35-54.

55.C57 Collection, *Distribution, Power and Regulating Transformers*, IEEE Press, 1991

56.Canadian Electrical Association Project RP-070-D-165, *Power Line Carrier on Distribution Systems*, Ontario Hydro's Research.

*57.*Wilsun Xu, *Multiphase Harmonic Load Flow Program (MHLF) Reference Manual.* Powertech Labs, Inc., February, 1991

58.Allan Greenwood, *Electrical Transients in Power Systems*, John Wiley & Sons Inc., New York, 1991.

59.ANSI/IEEE C37.011-1979, *IEEE Application Guide for Transient Recovery Voltage for AC-High Voltage Circuit Breakers Rated on a Symmetrical Current Basis.*

60.CIGRÉ Working Group 02 of Study Committee 13, *Interruption of Small Inductive Currents: Chapter 5 - Part I*, Electra No. 133, pp. 79-96.

61.Ernst A. Guillemin, *Synthesis of Passive Networks*, Chapter 8, John Wiley & Sons Inc., New York, 1957.

62.Athanasios Papoulis, *The Fourier Integral and Its Applications*, McGraw Hill Book Company Inc.,1962, pp.195-196.

63.Jirí Vlach, *Computerized Approximation and Synthesis of Linear Networks*, Chapter IV, John Wiley & Sons Inc., New York, 1969.

64.B. D. Cullity, *Introduction to Magnetic Materials*, Addison Wesley Publishing Company, 1972.

65.J. J. Becker, *Magnetization Changes and Losses in Conducting Ferromagnetic Materials,* Journal of Applied Physics, Vol. 34, No. 04 (Part 2), April, 1963, pp. 1327-1332.

66.David F. Tuttle, *Electric Networks Analysis ant Synthesis,* Chapter XI, McGraw Hill Inc. 1965.

67.United States Steel, *Electrical Steel Sheets Engineering Manual,* 4th Edition, 525 William Penn Place, Pittsburgh 30, PA.

68.William H. Press, Saul A. Telkolsky, William T. Vetterling, Brian P. Flannery, *Numerical Recipes, The Art of Scientific Computing,* 2nd Edition, Section 5.13, Cambridge University Press, New York,1992.

69.L. Stuehm, B. A. Mork and D. Mairs, *Five Legged Core Transformer Equivalent Circuit,* IEEE Transactions on Power Delivery, Vol. PWRD-4, July 1989, pp. 1786-1793.

*70.*A. C. Franklin and D. P. Franklin, *The J & P Transformer Book: A Practical Technology of the Power Transformer,* 11th Edition, Butterworths, 1983.

*71.*A. E. Emanuel, *Nonsinusoidal Waveforms in Power Systems .Basic Definitions,* IEEE Tutorial Course 90EH0327-7-PWR.

Appendix A

Orthogonality Between I_r and I_l

Consider the circuit of Figure 3.1a. The voltage across the transformer terminals and its correspondent flux linkage can be written in the form

$$v(\theta)=V_k \sin\theta, \tag{A.1}$$

and

$$\lambda(\theta)=-\lambda_k \cos\theta, \tag{A.2}$$

respectively.

Let us use Fourier analysis to represent the current $i_r(\theta)$ through the nonlinear resistance and the current $i_l(\theta)$ through the nonlinear inductance. Due to the odd symmetry of the $v-i_r$ and $\lambda-i_l$ curves, $i_r(\theta)$ and $i_l(\theta)$ will have only odd harmonic components in the form

$$i_r(\theta)=a_1 \sin\theta + a_3 \sin 3\theta + \cdots + a_p \sin p\theta + \cdots \tag{A.3}$$

and

$$i_l(\theta)=b_1 \cos\theta + b_3 \cos 3\theta + \cdots + b_p \cos p\theta + \cdots, \tag{A.4}$$

where p is odd.

The total current $i_t(\theta)$ is then:

$$i_t(\theta) = i_r(\theta) + i_l(\theta), \tag{A.5}$$

i.e.,

$$i_r(\theta) = \sqrt{a_1^2 + b_1^2}\sin(\theta + \gamma_1) + \sqrt{a_3^2 + b_3^2}\sin(3\theta + \gamma_3) + \cdots + \sqrt{a_p^2 + b_p^2}\sin(p\theta + \gamma_p) + \cdots, \tag{A.6}$$

where $\gamma_p = \arctan(b_p / a_p)$.

Evaluating the *rms* values of $i_r(\theta)$, $i_l(\theta)$ and $i_t(\theta)$, we have

$$I_{r-rms} = \sqrt{a_1^2 + a_3^2 + \cdots + a_p^2 + \cdots}, \tag{A.7}$$

$$I_{l-rms} = \sqrt{b_1^2 + b_3^2 + \cdots + b_p^2 + \cdots} \tag{A.8}$$

and

$$I_{t-rms} = \sqrt{a_1^2 + b_1^2 + a_3^2 + b_3^2 + \cdots + a_p^2 + b_p^2 + \cdots}, \tag{A.9}$$

respectively.

From equations (A.7), (A.8) and (A.9), it can be seen that

$$I_{t-rms}^2 = I_{r-rms}^2 + I_{l-rms}^2. \tag{A.10}$$

Appendix B

Measurement of the Initial Magnetization Curve

The initial magnetization curve is a plot of the locus of the DC symmetrical hysteresis loop tips for different peak values of magnetization. Figure B.1 is the circuit used to measure it.

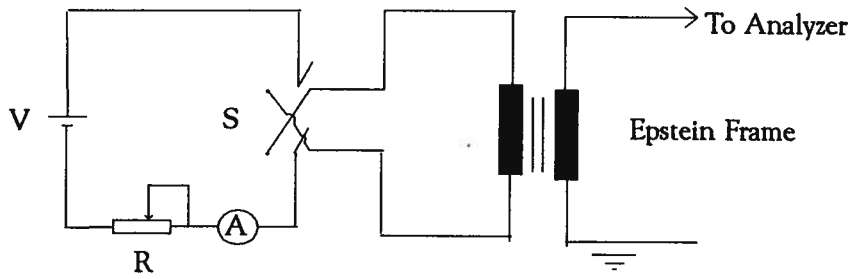

Figure B.1: Measurement of the initial magnetization curve.

The magnetizing winding of the Epstein frame (primary winding) is connected to a DC power supply through a reversing switch S, ammeter and a decade resistance box R. The secondary winding is connected to a digital waveform analyzer where the voltage

waveform is obtained and numerically integrated to give the flux linkage across the secondary winding.

The Epstein frame is demagnetized before any measurement is taken. This is accomplished by driving the core into saturation using alternating current at power frequency and gradually reducing the core excitation to zero.

After demagnetization, R is set to provide a low current, and S is reversed several times to assure the sample is in a definite hysteresis cycle (AA' and A'A trajectories of Figure B.2). Then, the first reading takes place. The voltage across the secondary winding of the Epstein frame is integrated and the flux difference between AA' is obtained. This value is divided by two and segment OA is plotted.

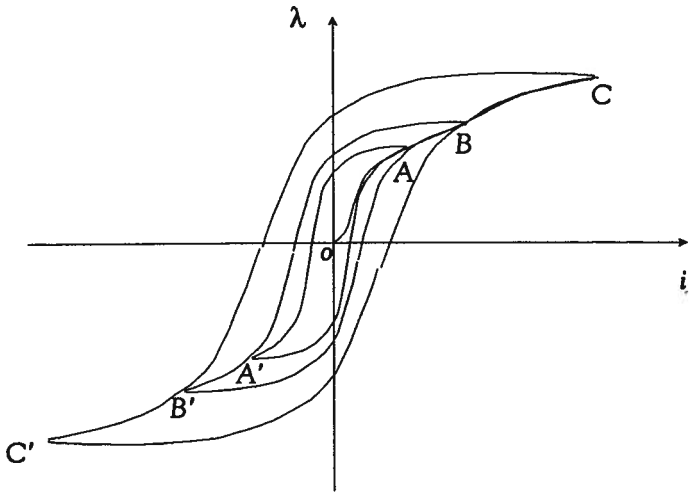

Figure B.2: Hysteresis loop locus.

After the first reading, R is changed to give a slightly greater value of the current in the primary winding and the process is repeated up to the desired limit.

Appendix C

Computation of Triplen Harmonic Components

Although only the computation of triplen harmonics is needed, it is appropriate to show the derivation of all odd harmonic components of the current that may be produced by saturation curves during standard tests. The equations below are developed for nonlinear inductances. For nonlinear resistances, one just needs to replace λ by and L by R in all equations.

Consider the piecewise nonlinear inductance of Figure 4.2c. For a sinusoidal flux $\lambda(\theta)=\lambda_k \sin(\theta)$, the current can be written in a Fourier series form containing odd harmonics only. So,

$$i_{l\Delta}(\theta)=b_1 \sin\theta + b_3 \sin 3\theta + \cdots + b_p \sin p\theta + \cdots , \tag{C.1}$$

where p is odd, and

$$b_p = \frac{4}{\pi}\int_0^{\frac{\pi}{2}} i_{l\Delta}(\theta)\sin p\theta d\theta . \tag{C.2}$$

For segment $k=2$,

$$b_p = \frac{4}{\pi}\left[\int_0^{\theta_1}\left(\frac{\lambda_2 \sin\theta}{L_1}\sin p\theta\right)d\theta + \int_{\theta_1}^{\frac{\pi}{2}}\left(i_{l\Delta_1}+\frac{\lambda_2 \sin\theta-\lambda_1}{L_2}\right)\sin p\theta d\theta\right].$$

Substituting $\Gamma_1=\frac{1}{L_1}=\frac{i_{l\Delta_1}}{\lambda_1}$ and $\Gamma_2=\frac{1}{L_2}$ into the equation above, the fundamental current ($p=$) and its harmonics ($p>$) are:

$$b_1=\Gamma_2\lambda_2+\frac{4}{\pi}[(\Gamma_1-\Gamma_2)(s(\theta_1)\lambda_2+\lambda_1 cos\theta_1)]$$

and

$$b_p=\frac{4}{\pi}[(\Gamma_1-\Gamma_2)(g(p,\theta_1)\lambda_2+\frac{\lambda_1}{n}cos\, p\theta_1)].$$

With

$$s(\theta_1)=\frac{1}{2}\left(\theta_1-\frac{1}{2}\sin 2\theta_1\right)$$

and

$$g(p,\theta_1)=\frac{\sin[(p-1)\theta_1]}{2(p-1)}-\frac{\sin[(p+1)\theta_1]}{2(p+1)}.$$

Finally, for any segment k, one can write

$$b_1=\Gamma_k\lambda_k+\sum_{i=2}^{k}\frac{4}{\pi}(\Gamma_{i-1}-\Gamma_i)(s(\theta_{i-1})\lambda_k+\lambda_{i-1}\cos\theta_{i-1})$$

and

$$b_p=\sum_{i=2}^{k}\frac{4}{\pi}(\Gamma_{i-1}-\Gamma_i)\left(g(p,\theta_{i-1})\lambda_k+\frac{\lambda_{i-1}}{p}\cos p\theta_{i-1}\right),$$

where

$$\Gamma_k=\frac{1}{L_k},$$

$$s(\theta_i)=\frac{1}{2}\left(\theta_i-\frac{1}{2}\sin 2\theta_i\right)$$

and

$$g(p,\theta_i)=\frac{\sin[(p-1)\theta_i]}{2(p-1)}-\frac{\sin[(p+1)\theta_i]}{2(p+1)}.$$

Appendix D

Rational Approximation of the Real Part of Y(s)

D.1 Fitting Procedure

Similar to equation (5.8), the frequency-dependent resistance could be expressed as a rational function in $-s^2$

$$R(s) = R_\infty \frac{(-s^2 + a_1^2)(-s^2 + a_2^2)\cdots(-s^2 + a_n^2)}{(-s^2 + b_1^2)(-s^2 + b_2^2)\cdots(-s^2 + b_n^2)}, \tag{D.1}$$

and with $s=j\omega$, $R(\omega)$ is written in the form:

$$R(\omega) = K_c \frac{(c_1\omega^2 + 1)(c_2\omega^2 + 1)\cdots(c_n\omega^2 + 1)}{(d_1\omega^2 + 1)(d_2\omega^2 + 1)\cdots(d_n\omega^2 + 1)} \tag{D.2}$$

Where K_c, $c_i = 1/a_i^2$ and $d_i = 1/b_i^2$ are positive real numbers, with $i = 1,2,\cdots,n$. The right hand side of (D.1) is fitted to the known function $R(\omega)$. The goal here is to compute K_c, c_i and d_i. The number of terms n will depend on the frequency range of interest. $R(\omega)$ is fitted interval by interval as shown in Figure D.1 starting with the interval between ω_{min} and ω_1 and ending with the interval between ω_n and ω_{max}.

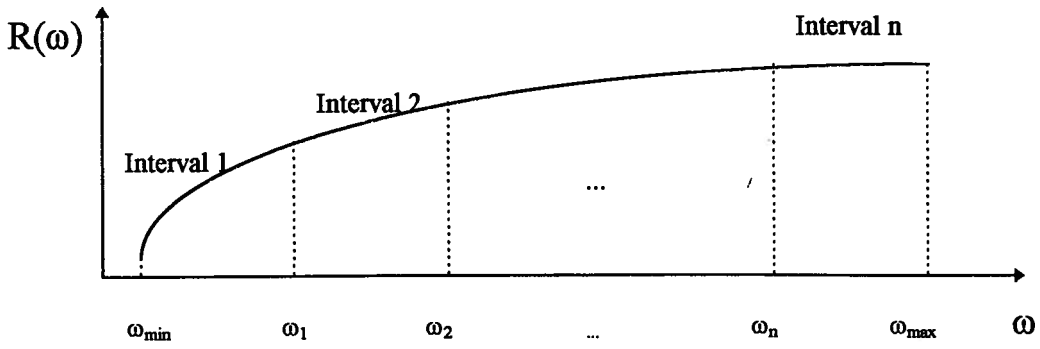

Figure D.1: Frequency dependent resistance.

The algorithm proceeds as follows:

1 - For interval 1, write R(ω) as

$$R(\omega) = K_c \frac{(c_1\omega^2 + 1)}{(d_1\omega^2 + 1)} = \frac{K_d\omega^2 + K_c}{(d_1\omega^2 + 1)}$$

or

$$K_d\omega^2 - d_1 R(\omega)\omega^2 + K_c = R(\omega) \qquad \text{(D.3)}$$

2 - Estimate ω_1. Take m frequency sample points between ω_1 and ω_{min} . Build the overdetermined system of equations (D.3) with only the parameters K_c, K_d and d_i unknown. A weighted linear least square fitting routine[68] is used to find these parameters ($c_1 = K_d/K_c$ is also computed). If the maximum error in the fitting is less than a predifined value, proceed to next step, If not, ω_1 is reduced by small steps $\Delta\omega_1$ and the system of equations (D.3) is reevaluated.

3- For interval 2 in Figure D.1, write R(ω) as

$$R(\omega) = K_c \frac{(c_1\omega^2 + 1)(c_2\omega^2 + 1)}{(d_1\omega^2 + 1)(d_2\omega^2 + 1)},$$

with K_c, c_1 and d_i already known from the previous step. Estimate ω_2 and find c_2 and d_2 following the procedure of step 2, with the m frequency samples now taken between ω_{min} and ω_2.

For the remaining intervals in Figure D.1, c_i and d_i are found in the same fashion and the constants R_∞, a_i and b_i of (D.1) are determined.

Experience has shown that a first estimate of $\omega_1 = 5\omega_{min}$ (with $\Delta\omega_1=0.1\omega_{min}$) and subsequent estimates of $\omega_{i+1} = 10\ \omega_i$ (with $\Delta\omega_i = 0.1\omega_{i-1}$ for $i \geq 2$) are usually very close to the final values for an error of 3% and 100 frequency samples used as input parameters to the fitting routine.

D.2 G(ω) Obtained from Lamination Data

Steel manufactures may supply core loss vs. frequency curves for the most commom lamination grades subjected to constant flux amplitudes[1]. These data are generally obtained on Epstein samples using a sine wave voltage source following the test procedure of ASTM Standard Method A-34. With this information one can obtain either the frequency-dependent resistance R(ω) or conductance G(ω) as described next.

In the sinusoidal steady state the average power P_{loss} is:

$$P_{loss} = P(\omega). \tag{D.4}$$

---

[1] To avoid confusion of trade names, the American Iron and Steel Institute has assigned AISI type numbers to electrical steel. These consist of the letter "M" (for magnetic material) followed by a number which, when the designations were originally made, was about to ten times the core loss in watt/lb at 15 kilogauss (1.5 T) and 60 Hz for 29 gage sheet (0.0140 in). Core losses have since been reduced but the type numbers remain [59].

$R(\omega)$ is obtained by:

$$R(\omega)=\frac{V_m^2}{2P_{loss}}=\frac{\lambda_m^2\omega^2}{2P(\omega)}, \tag{D.5}$$

where V_m and λ_m are the amplitude of the applied voltage and flux, respectively. Since the flux is kept constant, $R(\omega)$ can be written in the form:

$$R(\omega)=K\frac{\omega^2}{P(\omega)}. \tag{D.6}$$

It is convenient to normalize $R(\omega)$ assuming that the resistance measured at the transformer rated frequency ω_r is $R(\omega_r)=1$. So, the constant K in the equation above is

$$K=\frac{P(\omega_r)}{\omega_r^2}, \tag{D.7}$$

and the normalized resistance $R_N(\omega)$ is

$$R_N(\omega)=\frac{P(\omega_r)}{\omega_r^2}\cdot\frac{\omega^2}{P(\omega)}. \tag{D.8}$$

So, if the transformer lamination loss vs. frequency curve is known, an estimate of the frequency-dependent core loss resistance can be made by scaling the normalized resistance $R_N(\omega)$ to the resistance at rated frequency $R(\omega_r)$. Then,

$$R(\omega)=R_N(\omega)\cdot R(\omega_r), \tag{D.9}$$

or for the conductance $G(\omega)$

$$G(\omega)=\frac{1}{R(\omega)}. \tag{D.10}$$

D.3 G(ω) Obtained from Standard Tests

The frequency-dependent core resistance could also be estimated from transformer standard tests. The plot of loss/cycle can be crudelly approximated by a straight line, as shown in Figure D.2.

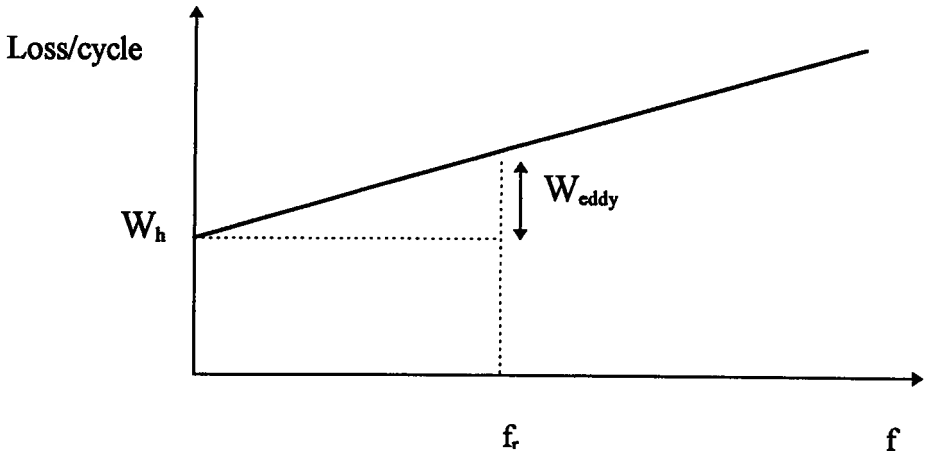

Figure D.2 : Transformer core loss curve at rated flux.

Power transformer manufacturers usually supply two or three values of no-load loss at different frequencies, with the flux kept at the rated level. From Figure D.2, the loss per cycle coud be written as

$$\frac{P_{loss}}{f} = W_h + W_{eddy} \cdot \frac{f}{f_r}, \qquad \text{(D.11)}$$

where f is the frequency in which the loss is measured, f_r is the rated frequency, W_h is the hysteresis loss per cycle and W_{eddy} is eddy loss per cycle at the rated frequency.

Taking (D.11) and writing the loss for the angular frequency $\omega=2\pi f$,

$$P_{loss} = \frac{1}{2\pi}\left(W_h \cdot \omega + W_{eddy} \cdot \frac{\omega^2}{\omega_r}\right). \tag{D.12}$$

From (D.6) and (D.12), the resistance R(ω) is

$$R(\omega) = \frac{\lambda_m^2 \omega^2}{2P_{loss}} = \frac{\lambda_m^2 \omega^2}{\frac{1}{\pi}\left(W_h \cdot \omega + W_{eddy} \cdot \frac{\omega^2}{\omega_r}\right)} \tag{D.13}$$

Normalizing R(ω), as done for (D.7) and (D.8),

$$R_N(\omega) = \frac{K\omega}{ratio + \frac{\omega}{\omega_r}}, \tag{D.14}$$

where ratio=W_h/W_{eddy} and

$$K = \frac{ratio+1}{\omega_r}.$$

The resistance and conductance are then:

$$R(\omega) = R_N(\omega) \cdot R(\omega_r), \tag{D.15}$$

and

$$G(\omega) = \frac{1}{R(\omega)}.$$

If the transformer manufacturer does not supply the core loss vs. frequency curve, a typical ratio W_h/W_{eddy} is commonly taken as unity [70]. In practice, the straight line of Figure D.2 could be drawn using loss measurement data gathered from routine tests. For instance, it could be obtained from the loss measurement taken at rated voltage and rated frequency and, as recommended by ANSI C57.12.90 (Induced Overvoltage Withstand Test), from the loss measurement taken at twice the rated frequency and double voltage amplitude.